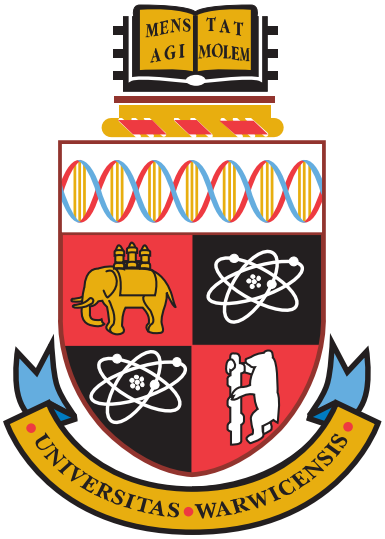

Image-Based Modelling of Cell Reorientation

Robert Lockley

A thesis presented for the degree of
Doctor of Philosophy

Department of Systems Biology

Date: September 2015

THE UNIVERSITY OF
WARWICK

CONTENTS

LIST OF FIGURES

LIST OF TABLES

ACKNOWLEDGEMENTS

I would like to thank the following people without whom I would not have completed this thesis.
First I would like to thank my supervisors Till Bretschneider and Graham Ladds for their support and direction with this project, and all the members of their respective groups. Many thanks to Wayne Croft and Ingrid Tigges for their help with working with *Dictyostelium* and the microscopy and to Jérémie Dalous for shear flow experimental data.
I would like to thank my advisory panel of Mike Chappell, Björn Stinner and Anatoly Shmygol, for their advise on the project and all the staff and fellow students at Systems Biology.
Finally, I would like to thank my parents Brenda and Steve, and my partner Alice for their support whilst I have been working on this project.

DECLARATION

This thesis is presented in accordance with all the regulations for the degree of Doctor of Philosophy. The work presented in this thesis was undertaken by myself unless otherwise stated. It was composed by myself and no work in it has been submitted for a degree or qualification at this University or any other institution.

ABSTRACT

Directed cell motility plays a key role in many areas of biology, with cells able to reorient quickly in response to changes of an extracellular stimuli. A complex signalling network directs this response, which motivates the use of conceptual mathematical models that replicate aspects of this behaviour and can be more readily analysed. Comparisons between such models have more focused on the qualitative differences between them. We wished to construct a framework for the rigorous comparison between models, using cell repolarisation in response to shear flow change.

We fitted three reaction-diffusion models of cell polarity to experimental data of *dictyostelium* amoeba repolarising in response to mechanical shear flow. Experiments performed under different conditions were fitted simultaneously, to provide models with a range of cellular dynamics, with the models being fit to spatio-temporal data of cortex fluorescence of an F-actin reporter. All models were able to give a satisfactory fit, with parameter identifiability determined using the profile likelihood. The Meinhardt and Levchenko models were able to obtain better fits than the Otsuji model. Analysis of the model behaviour and parameter identifiability prompted alterations of the models, which resulted in a fully identifiable two-variable Meinhardt model.

Simulations of the Meinhardt and Levchenko models were used to test their behaviour over time frames past which the models had been fitted. This motivated changes to the model parameters to obtain the desired long-term behaviour. Further simulations were run to elicit the model response to a changing external signal beyond that seen in the fitting, with the models being able to adapt to a moving signal, and respond to multiple simultaneous signals.

Further fitting of the Meinhardt and Levchenko models was conducted using single cell data. The models were able to fit well to data taken from both repolarising and unstimulated cells, showing that these models are able to replicate both mean and single cell spatio-temporal imaging data.

ABBREVIATIONS

BCa	Bias-corrected and accelerated
cAMP	Cyclic denosine monophosphate
cGMP	Cyclic guanosine monophosphate.
CI	Confidence interval
fMLP	Formylmethionyl-leucyl-phenylalanine
G-protein	Guanine nucleotide-binding proteins
GFP	Green fluorescent protein
GPCR	G protein–coupled receptor
GTP	Guanosine-5'-triphosphate
LEGI	Local excitation global inhibition
PI3K	Phosphatidylinositol-4,5-bisphosphate 3-kinase
PIP3	Phosphstidylinositol (3,4,5)-triphosphate
PLA2	Phospholipase A2
PLE	Parameter likelihood estimation
RE	Relative error
RFP	Red fluorescent protein
SE	Standard error
sGC	Soluble guanylyl cyclase
TORC2	Target of rapamycin complex 2

1. INTRODUCTION

1.1 Cell Motility and Polarity

Cell motility is an important facet of cell behaviour. It allows cell migration, a vital part of many biological processes including development, immune response and cancer metastasis. This movement can either be random or directed in response to an external signal. In amoeboid cell motility, this movement is primarily driven by the formation and protrusion of pseudopods. This protrusion is driven by the polymerisation of actin filaments, which push the cell membrane forward. Retraction of the rear of the cell is achieved through the use of contractile forces generated through Myosin-II. Together, these combine to allow a cell to move through extending a front and retracting its rear.

In order to direct its movement, a cell needs to be able to translate an external signal into an internal cell polarity. In this instance polarity refers to the asymmetric distribution of proteins inside the cell. By acquiring a polarity the cell is given a clear front and back, allowing it to move in the desired direction. This polarity defines the axis that the cell is directed upon when it moves. Internal pathways activated by the signal are used to induce this polarity in the cell, allowing it to direct the regulation of cellular processes that produce the actin/myosin behaviour needed for it to move.

1.2 Chemotaxis

The most well studied experimental system of induced polarity is the response of cells to chemoattractant gradients. In *Dictyostelium discoideum*, these can be a diverse range of attractants (folic acid, platelet activating factor, lysophosphadtidic acid), with the most well studied being cAMP, (Chen et al. 1996). Neutrophils recognise bacterial proteins through G-protein coupled fMLP receptors (Nardin et al. 1991), whilst fibroblasts respond to gradients of platelet-derived growth factor. Chemotaxis is the ability to sense spatial heterogeneities of a chemical attractant and to respond such that the cell can migrate along the gradient. It is crucial for single celled organisms, allowing them to navigate towards food and to congregate if required. In larger organisms, chemotaxis plays a vital role during development and allows direction of immune cells towards sources of infection.

Bacterial cells sense chemoattractant gradients in a temporal manner, sensing gradients as they travel and hence determining whether or not the direction is suitable. This information is used to bias a series of runs and tumbles to direct the cell in the right direction (Wadhams & Armitage 2004).

Eukaryotic cells sense chemoattractant gradients by translating extracellular signal gradients into an intracellular gradient of signalling components that result in the specification of a cell front and rear (Bagorda & Parent 2008). Chemoattractant receptors, commonly G-protein coupled, are uniformly distributed along the cell membrane, even in the presence of gradients (Parent & Devreotes 1999). The sensing is achieved by the redistribution or activation of signalling lipids and proteins localised to receptor proteins on the membrane. By comparing occupancy a direction can be determined which biases the cell motility. As this sensing remains unaffected when immobilising cells it indicates a spatial gradient sensing mechanism (Parent &

Devreotes 1999).

1.3 Mechanotaxis

Besides polarisation during chemotaxis, *Dictyostelium*, neutrophils and endothelial cells can polarise in response to mechanical stimuli (Dalous et al. 2008, Dixit et al. 2011, Valignat et al. 2013, Zhu et al. 2014, Wojciak-Stothard & Ridley 2003). Examples of such stimuli are flow shear stress and substrate stiffness. In the case of flow shear stress media flows over the cell at a rate insufficient to cause detachment from the substrate. This flow of media stimulates a response, with the cell polarising as with a chemotatic signal. In *Dictyostelium* this is the production of a protruding actin front into the flow and a retracting tail (Dalous et al. 2008). The response of Neutrophils to shear flow stress is cytoplasmic pseudopod retraction, with GPCRs acting as mechanosensors (Makino et al. 2006). Endothelial cells reorient in response to flow shear stress in a two-stage process. First there is Rho-induced depolarisation, followed by Rho/Rac-mediated polarisation and migration following the direction of flow (Wojciak-Stothard & Ridley 2003).

Such mechanotaxis has advantages over chemotaxis for data analysis in that it provides a single shear stress experienced by all cells in the experiment, allowing parallel analysis of multiple cells. This can be done using a flow chamber with an area of homogeneous laminar flow and imaging cells that are in it. Signal strength is easily changed and precisely controlled. This contrasts to chemotaxis where the concentration of chemoattractant will change as the cells move in response to the chemoattractant gradient. This results in a changing input signal, complicating the process of fitting any models to such data.

1.4 Dictyostelium

Dictyostelium discoideum is a single celled amoeba. It feeds on bacteria amongst the leaves and soil on forest floors. Once the local food supply is exhausted, it undergoes a behavioural change, switching from migrating to locate food to forming aggregates with surrounding cells. These aggregates develop into multicellular fruiting bodies, consisting of a ball of spore cells held up by a stalk to allow dispersion to new feeding grounds. This behaviour has earned it the term 'social amoeba'. *Dictyostelium* is an attractive organism for use in studying cell motility and polarity. Its lifestyle is totally dependent on efficient motility. In order to hunt down bacteria in the soil, it must be able to move towards factors secreted by the bacterium. It also uses chemotaxis to congregate into an aggregate (Konjin et al. 1968). By secreting cyclic adenosine monophosphate (cAMP) from the rear, they attract one another into the aggregate. However, an external stimulus is not needed for *Dictyostelium* to be motile. In the absence of a chemoattractant signal it performs random motility (Li et al. 2008).

1.4.1 Dictyostelium *Chemotaxis*

Dictyostelium cells detect gradients of cAMP using heterotrimeric G-protein coupled receptors that activate a number of downstream pathways. Four receptors are expressed progressively during developement, cAR1, cAR3, cAR2 and cAR4 (Saran et al. 2002). These pathways combine together to produce the polarisation behaviour observed in *Dictyostelium*. An early hypothesis is the idea that the cell orientates through a chemical compass that locally induces actin polymerisation and the production of new pseudopods at the part of the cell closest to the signal.

The first molecule to be identified that satisfied this behaviour was phosph-

stidylinositol (3,4,5)-triphosphate (PIP3). It is produced in response to extracellular stimuli and is strongly enriched at the leading edge of *Dictyostelium* in strong gradients of chemoattractant (Parent et al. 1998). Though it was initially thought that it was a singular compass to steer the cell, it has been shown that whilst disruption of PIP3 kinase reduces the chemotactic efficiency of *Dictyostelium*, *Dictyostelium* cells completely unable to generate any PIP3 are still capable of chemotaxis in steep gradients (Hoeller & Kay 2007).

The realisation that chemotaxis was possible without PIP3 prompted a search for other signalling pathways that can orientate the cell. Several other signalling molecules have been identified that are important in chemotaxis and migration. One important intracellular pathway induced upon receptor activation involves the conversion of members of the Ras family of small GTPases into their active GTP-bound state, which occurs upstream of the PI3K response. RasG and rasC were found to be the most important in the response to cAMP, with the loss of both these genes effectively blocking directional movement, indicating that Ras signalling plays an essential role in chemotactic signalling (Bolourani et al. 2006). Ras plays an important role in macropinocytosis with PI3K1/2 and PI3K4. The absence of RasG or RasS causes severe macropinocytosis defects, and the absence of PI3K1/2 and PI3K4 completely removing macropinocytosis (Hoeller et al. 2013).

Another candidate that was found is the target of rapamycin complex 2 (TORC2) (Lee et al. 2005). This complex is activated via Ras upon cAMP stimulation, and acts through two different pathways, one PI3K dependent and one PI3K independent. (Kamimura et al. 2008) There is some functional overlap between the two pathways allowing partial compensation, indicating that the PI3K and TORC2 work in parallel to mediate response to cAMP.

Two other signalling pathways have been found that are PI3K independent. These involve a member of the phospholipase A2 family (PLA2) (Chen et al. 2007) and soluble guanylyl cyclase (sGC) (Veltman et al. 2008). PLA2 does not change localisation in response to chemoattractant, but facilitates the underlying motility of the cell. sGC has two independent signalling roles. It localises to the front of the cell, interacting with F-actin. Its product, cGMP, localises to the rear of the cell where it produces myosin filaments to drive retraction (Bosgraaf et al. 2002). These signalling pathways work together to regulate the response of *Dictyostelium* to cAMP. Loss or disruption of one of these pathway can be compensated for by others, giving the cell a robust and flexible system for regulating chemotaxis.

The primary method of *Dictyostelium* chemotaxis is through the extrusion of pseudopods, driven by F-actin, though it will move with blebs in the face of sufficiently high resistance. The actin polymerisation for pseudopod protrusion is controlled through the SCAR/WAVE complex and Rac Ibarra et al. (2005).

1.4.2 Dictyostelium *Mechanotaxis*

In addition to chemotactic behaviour *Dictyostelium* also exhibits a response under stimulation by shear stress (Décavé et al. 2003). Cells consistently orientated pseudopods against shear flow, behaving in a way similar to that seen in chemotactic studies. This orientation was disrupted through the inhibition of PI3K without disrupting the pseudopod extension. The formation of pseudopods is sensitive to calcium, but not the directionality of movement (Fache et al. 2005). These combine to suggest that the shear flow response involves two pathways, one activating G proteins to control cell speed, modulated by calcium, the other resulting in a PIP3 gradient that

controls cell orientation.

When considering the responses induced by a change in the direction of flow, the response was shown to be similar to that exhibited in response to the change of a strong chemotactic gradient (Dalous et al. 2008). The front of actin polymerisation and myosin tail break down before reforming on the opposite ends of the cell. The timing of this response was modulated by the strength of the shear stress that the cells were exposed to. The rate at which this process happened differed in the two different shear flow conditions. The higher shear stress acted as an inhibitor towards the formation of a new front, increasing the time before the cell fully repolarised, Fig. 1.1 B,C. The rate at which the old front degraded was unaffected by the different shear stresses.

In addition to observing repolarisation, data were also collected for the cell returning to random motility after flow removal, and acclimatising to flow after a period of no flow, Fig. 1.1 D,E. These were both using the flow shear stress of 2.1Pa. Together, these give 4 different conditions to which polarisation models can be fitted.

1.5 Mathematical Modelling

There are two extremes in the approach of the establishment of cell polarity from a modelling perspective. One is to try to determine the entire biochemical pathway involved, and then dissect the network into independent modules whose behaviour can be analysed and then reintegrated back into the network. The other is to consider simpler models that have analogous capabilities. Once such models are understood and can replicate in this case cell polarisation, specific factors can be identified that follow similar kinetics as the components in the model. Most models will fall inbetween these two

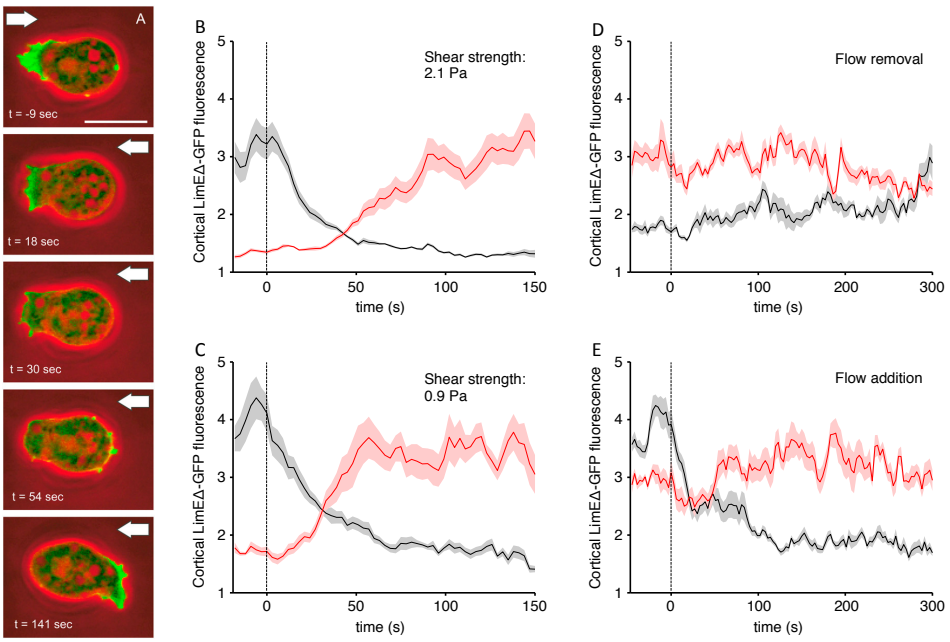

Fig. 1.1: **Actin repolarisation induced by a change in flow.** The response of cells to a rapid change in flow. Cells are exposed to a rapid flow reversal (A, B, C), the cessation (D) or the onset (E) of flow. (A) Sequence of images showing the change in localisation of the f-actin reporter (LimEΔ-GFP) during flow reversal. Arrows indicate direction of flow, with reversal at time $t = 0$. Scale bar $10\mu m$. (B, C, E) Quantification of the responses to flow change outlined above. The red lines indicate mean intensities of the cortical fluorescence in the halves of the cell that are upstream after flow change, whereas the black line indicates the mean of the downstream half of the cell. (D) Quantification of the response to the removal of flow, with the red line corresponding the half of the cell upstream before flow was removed, and the black line corresponding to the half of the cell downstream of flow. Zero time is the time of flow change, the shaded region indicates the error region of ± SE. For panel B, 18 responses of 14 cells were averaged; for panel C, 10 responses of 5 cells; for panel D 13 responses of 9 cells; for panel E 11 responses of 8 cells. Figure adapted from Dalous et al. (2008).

extremes. The level of complexity used in a model will depend on what the unknown mehcanistic information is, and quality and level of data available for model validation.

The first to consider if a simple reaction-diffusion system could replicate the pattern formation seen in nature was Turing (Turing 1952). His goal was to prove spontaneous pattern formation using only diffusion. A uniform chemical distribution is disturbed by the addition of diffusion of the components, allowing the formation of patterns based on the new distribution of the chemical components. The first authors to suggest this using this framework for investigating cell orientation were Gierer and Meinhardt, who demonstrated the use of lateral inhibition to develop pattern formation (Gierer & Meinhardt 1972, Meinhardt & Gierer 1974).

One of the first attempts towards creating a model for chemotaxis using this method was by Meinhardt (Meinhardt 1999). It used a single activator along with two inhibitors to replicate several facets of the behaviour seen in *Dictyostelium*. The two inhibitors had different roles; a global inhibitor provided the localisation of a single front of activation, and the second local inhibitor destabilised the front so that the cell could respond to a change in the external signal. Another early model designed to replicate the behaviour seen in *Dictyostelium* was proposed by Levchenko and Iglesias (Levchenko & Iglesias 2002). An activator and inhibitor are both activated in response to an external signal, and in turn influence a third response element. This was a local excitation, global inhibition (LEGI) model, where a fast acting local activator was coupled with a slower global inhibitor. When later coupled with a second excitable system, it was able to replicate most of the behaviour of chemotaxing cell, along the behaviour of several mutants (Xiong et al. 2010). These models are related to larger PI3K and PTEN

based model that also utilise amplification to replicate the behaviour seen in PIP3 in *Dictyostelium* (Levchenko & Iglesias 2002, Ma et al. 2004).
Other models have been proposed, based either on different mathematical foundations such as stochastic responses, coupling different polarity modules together, or by considering the detailed biochemistry present in the cell being studied (Jilkine & Edelstein-Keshet 2011). Work has also been conducted considering cell motility, coupling polarisation in the cell with the evolution of the membrane (Elliott et al. 2012).
Cell polarity models help the understanding of how cells respond to external signals. Relatively simple models can match some of the complicated dynamics seen in cell repolarisation, providing insights into the possible underlying dynamics present. More complex biological models can motivate conceptual models that aim to capture the shared dynamics. However, it can be difficult to measure all the rate constants needed for highly detailed models. For more conceptual models, the rate constants and model species may have no direct biological meaning. This can make it difficult to draw any direct biological conclusions from any model analysis.

1.6 Identifiability Analysis

For a comprehensive analysis of modelling results it is necessary to know reliable parameter estimates. Given model predictions rely on the calibrated parameters, the reliability of the parameters will affect model predictions accordingly. In model fitting not all components may be observable, or data may be insufficient to assure that parameter estimates are reliable. What follows is a formal definition of structural identifiability.
Let $\mathbf{p}$ be a parameter vector belonging to the parameter space $\mathbf{P}$ such that $\mathbf{p} \in \mathbf{P}$. Let $\mathbf{y}(t, \mathbf{p})$ be the model output function. Consider $\overline{\mathbf{p}}$, such that

$\overline{\mathbf{p}} \in \mathbf{P}$ and $\mathbf{y}(t, \mathbf{p}) = \mathbf{y}(t, \overline{\mathbf{p}})$ for all t. If this equality, in a neighbourhood $\mathbf{N} \in \mathbf{P}$ of $\mathbf{p}$, implies that $\mathbf{p} = \overline{\mathbf{p}}$ then the model is locally structurally identifiable in a neighbourhood $\mathbf{N}$. If $\mathbf{N} = \mathbf{P}$, then the model is globally structurally identifiable. If no neighbourhood $\mathbf{N}$ exists, then the parameter is structurally unidentifiable.

Parameters are non-identifiable if they cannot be estimated, i.e. they do not influence the quality of the model fit. Identifiable parameters are determined from confidence intervals, with a desired probability (Lehmann & Leo 1983). There are two types of identifiabilities, structural and practical. Structural identifiability concerns the structure of the model and the observations that go with it, where as practical identifiability concerns the amount and quality of the data. A model that is structurally unidentifiable cannot be practically identifiable as there does not exist enough observations, or the model is formulated in such a way as to make obtaining unique results for certain parameters impossible. However, a model can be structurally identifiable, but practically unidentifiable if the quality of the data is insufficient to allow identifiable parameter estimates. This is affected by noise in the data, the sample rate of the data and any errors in the model.

To resolve practical unidentifiabilities it is necessary to improve the quality or quantity of the data. To resolve a structural unidentifiability it is necessary to reparameterise the model in order to minimise the parameters used. Several tools exist to determine model identifiability. These include the Exact Arithmetic Rank (EAR) software(Karlsson et al. 2012), the DAISY software, which uses an approach based on differential algebra algorithms (Bellu et al. 2007) and the numerical based Profile Likelihood Estimation (Raue et al. 2011).

1.7 Aims and Objectives

The central aim of this project is to develop a framework for the rigorous comparison of different cell polarity models. Many models have been proposed to try to answer how cells are able interpret an external signal, and what mechanisms they need to turn this into an internal asymmetry that forms a directional response. These models differ in their assumptions as to the dynamics of the signal sensing, along with the level of biological detail that they contain. The focus will be on conceptual models that are designed to replicate cell polarity behaviour, as opposed to detailed biochemical models. Firstly, good quality fits will be obtained of the models to mean repolarisation data of *Dictyostelium*. Identifiability analysis will be used to analyse the model fits and indicate confidence levels on the parameters values obtained in the fitting. Model comparisons will be conducted through the quality of the model fits and the level of model identifiability. This identifiability analysis, along with model simulations, will be used to guide any changes to the models. This will be done to improve the model fits, model identifiability and the models longer term behaviour. Using these fitted models simulations will be used to further test model behaviour, and to provide predictions for further repolarisation experiments.

Using the same methods for fitting models to mean cell data, models will be fitted to individual cell data. This will be of both repolarising and unstimulated cells. From the fitted models, parameter estimates and species dynamics can be compared to back to those observed in cells to find suitable cadidates for model components.

In addition, I will also use fluorescence microscopy to gather further image data of *Dictyostelium*. This will be both of unstimulated cells and those exposed to external cues. Using the Ibidi flow chamber system I will attempt

to obtain more cell repolarisation data, for model validation and further fitting.

The following chapter contains the materials and methods, along details of the cell polarity models that will be used in later chapters. In Chapter 3, I will detail the results of the fluorescence imaging experiments with *Dictyostelium*. Chapter 4 shows the results of the model fitting and identifiability analysis. Chapter 5 details further model investigation, including model modifications and long term simulations. Chapter 6 contains the fitting to single cell data, and Chapter 7 contains the discussion and conclusions.

A paper was published Cytometry, entitled Image Based Validation of Dynamical Models for Cell Reorientation. It covered the model fitting, identifiability analysis and some of the modifications. It is included in Appendix C.

2. MATERIAL, METHODS AND MODELS

2.1 Dictyostelium *Cell Lines*

When working with *Dictyostelium* I followed protocols on the website Dictybase (www.dictybase.org)(Fey et al. 2007). I worked with two differently tagged cell lines, one double tagged with actin and myosin reporters and one with a single actin reporter.

2.1.1 Growth Protocol

Dictyostelium cells were grown in 10ml of growth medium in 10cm plastic cell culture dishes. Medium was HL5 supplemented with glucose (supplier ForMedium, peptone 14g/l, yeast extract 7g/l, glucose 13.5 g/l, KH_2HPO_4 0.5 g/l, Na_2HPO_4 0.5 g/l). Medium was supplemented with antibiotics depending on strain and dishes were kept between 21-23°C.
Dishes were subcultured every 2-3 days, depending on cell density, to avoid cell confluency. The majority of cells were removed along with the old medium, before 10ml of fresh medium was added. Dishes were subcultured 5-8 times before being discarded and new cultures started from frozen stocks.

2.1.2 LimE/GFP-Myosin Tagged Cell Line

The first *Dictyostelium* cell line consisted of wild type *Dictyostelium discoideum* (AX2) cells expressing LimEΔ-RFP F-actin reporter along with GFP-myosin-II myosin reporter, pBig-GFPMyo. The medium was supple-

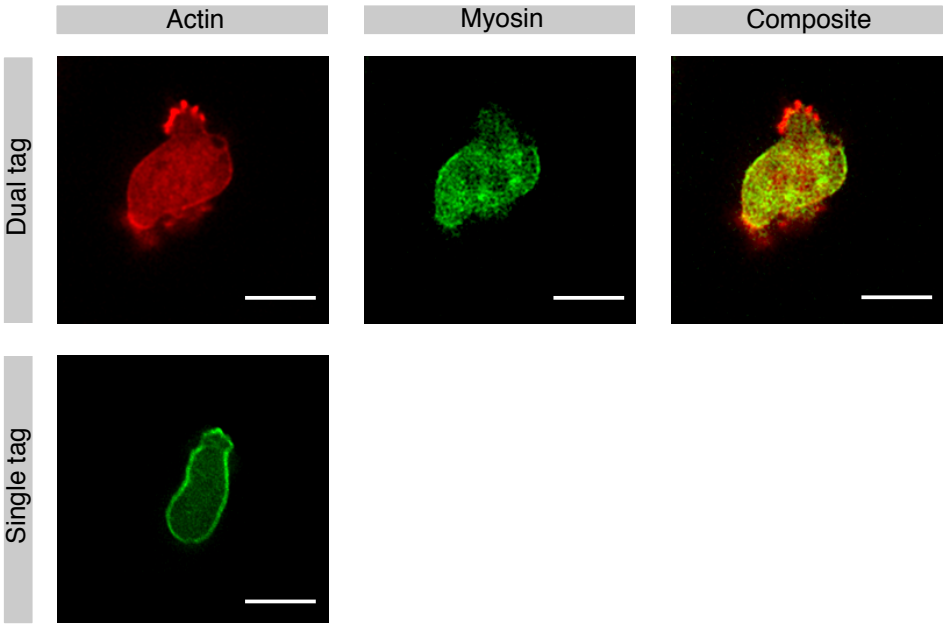

Fig. 2.1: ***Dictyostelium* cell lines** First row shows the dual tagged cell line, expressing red actin reporter and green myosin reporter. Second row shows the single tagged cell line, expressing green actin reporter. Scale bar 10µm.

mented with the antibiotics Streptomycin to 200 μg/ml, and G418 and Blasticidin to 10 μg/ml. An illustrative example is provided in the first row of Fig 2.1. The cells were a gift from Dr. Annette Müller-Taubenberger (LMU München).

2.1.3 ABP120 Tagged Cell Line

The second *Dictyostelium* cell line consisted of wild type *Dictyostelium discoideum* (AX2) cells expressing ABP120 actin reporter. The medium was supplemented with the antibiotics Streptomycin to 200 μg/ml, and Blasticidin to 20 μg/ml. An illustrative example is provided in the second row of Fig 2.1. The cells were a gift from Dr. Rob Kay (MRC Laboratory of Molecular Biology).

2.2 Imaging Details

To prepare them for imaging, cells were removed from culture dishes and washed twice with KK_2 buffer (16.5 mM KH_2PO_4, 3.9 mM K_2HPO_4 and 2 mM $MgSO_4$) to remove all growth media. Cells were starved in buffer for 0-2 hours before imaging or exposing to cAMP.

When exposing to cAMP for development, cells were starved in buffer for 1 hour, and subjected to pulses of 50µM of cAMP every 6 minutes for 5 hours.

To image cells exhibiting random motility, the cells were imaged on glass bottomed plates. When using the flow chamber, cells were imaged on Ibidi Luer slides (LxWxH 50x5x0.2 mm^3). These were connected to the flow chamber sytem as detailed in Section 2.3.

Images were taken on a Personal DeltaVision microscope equipped with a 40x/1.35 UAPO/340 Olympus oil objective. LimEΔ-RFP was excited using a 543nm laser with emission recorded at 594nm. GFP-myosin-II and ABP120-GFP were excited using a 488nm laser, with emission recorded at 520nm. Captured images were processed in SoftWorx to reduce optical distortion, being deconvolved using an interative-constrained algorithm, (Agard 1984). The algorithm generates an estimate of the deconvolved image. This is convolved with the point spread function of the objective lense and compared to the original image. The differences between them are used to modify the estimate, with the modified estimate constrained to be non-negative. This process removes out of focus blur, improving the quality of the image for analysis.

In order to maximise the amount of cellular behaviour seen in the time series taken I minimised the time between frames, which is limited by the exposure times for each channel that is imaged. The minimum time between frames was 1.6 seconds for dual channel images and 0.5 seconds for single channel

images.

2.2.1 QuimP

Single cells were tracked and fluorescence intensities in the cortex were calculated using the QuimP package (Tyson et al. 2010) for the ImageJ software. An iterative active contour algorithm determines the outline of the cell perimeter, as shown in Fig. 2.2. The accuracy of this outline is controlled through various parameters in the QuimP software, modification of which allows an accuracy of within 1μm of the cell boundary. This outline forms an 'outer chain', which is shrunk in towards the cell interior to form an 'inner chain', which separates the cell cortex from the interior. The distance it was shrunk by was 1.5μm to capture the entire cell cortex. Cortical fluorescence intensities were sampled by connecting corresponding nodes on the outer and inner chain. The maximal intensity along each connecting line is taken to be the local cortical intensity. To account for different protein expression levels and photobleaching, cortical fluorescence intensities are normalised with respect to the average intensity in the cell interior.

2.3 Flow Chamber

To expose cells to a changing flow of medium I used a flow chamber system from Ibidi. Cells were placed in Ibidi Leur flow chamber slides, which were connected to a pump system through a series of tubes. The pump system consists of air pressure pump which is connected to a fluidic unit. A reservoir of medium is mounted on the fluidic unit, with tubing connecting the reservoir to the chamber passing through a switching valve on the fluidic unit. The fluidic unit controls the direction of flow in the chamber through use of the switching valve. The media reservoir consists of two separate

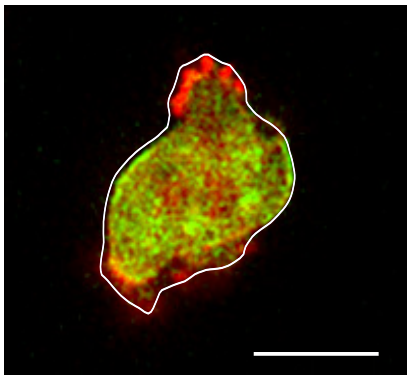

Fig. 2.2: **Cell cortex boundary as determined using Quimp software.** The same dual tagged *Dictyostelium* cell as shown in Fig. 2.1 is shown with the cell boundary as determined by QuimP (white line). Scale bar $10\mu m$.

tubes, with the switching value used to allow flow to change from one tube to the other without affecting the direction of flow in the chamber. The speed of flow in the chamber is controlled through the air pressure. This allows unidirectional flow for extended periods despite only having a reservior of media of roughly 10ml. This functionality of the system has been used on epithelial cells and bone tissue (Kotsis et al. 2008, Morris et al. 2010).

All these processes are controlled via the PumpControl software. This software can accept pre-programmed instructions, allowing multiple experiments to easily use the same flow conditions regardless of their complexity. Before each experiment, the system was calibrated so that an accurate flow rate was used during the experiments. This took the form of a calibration factor between the programmed flow rate and that measured from the change in the reservior levels, allowing the two to match during experiments. During experiments there was no leakage from the tubes or reservoirs, and they fitted securely to the fluidic unit. From tracking fluid levels in the reserviors, flow rates were observed to remain consistent with the programmed

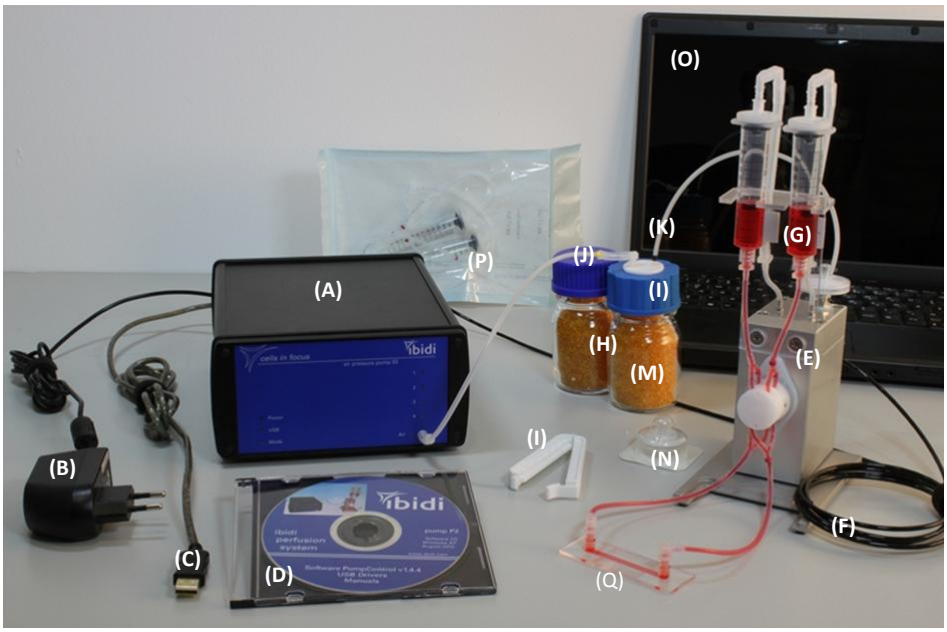

Fig. 2.3: **Equipment used in the flow chamber system.** (A) Ibidi air pressure pump. (B) Pump power plug. (C) Pump USB connector. (D) CD containing pump software. (E) Fluidic unit. (F) Electric cable to connect pump to fluidic unit. (G) Reservoirs with attached cables (filled with red fluid to distinguish the tubing). (H) Spare drying bottle. (I) Drying bottle connection cap. (J) Air pressure tubing connecting pump to drying bottle. (K) Air pressure tubing connecting drying bottle to fluidic unit. (L) Clamp. (M) Drying bottle. (N) Replacement filter for fluidic unit. (O) Laptop installed with PumpControl software. (P) Sterile reservoir and tubing set. (Q) Flow chamber slide. Image taken from Ibidi pump manual

values.

2.3.1 Dalous Flowchamber Data

For model fitting, data were taken from *Dictyostelium* repolarising in response to shear flow reversal. These experiments were previously reported by Dalous et al. (2008), using JH10 cells with an F-actin reporter (LimEΔ-GFP).

In the Dalous et al. experiments, cells were exposed to two different shear stresses, 0.9 Pa and 2.1 Pa. Above 2.1 Pa cells were detached from the

substrate due to the strength of the flow, and below 0.9 Pa cells turn to rotate the actin front, rather than repolarise through breaking down the old front and building a new one. To induce a repolarisation, cells were first subjected to flow in order to become polarised into the direction of flow. Upon the change of flow direction the cell repolarised through the old actin front breaking down and a new front being formed into the new direction of flow.

2.4 Bootstrap Comparison

The bootstrap is a statistical test that relies on random sampling with replacement to assign measures of accuracy to sample estimates (Efron 1977). This approach can be used when standad statistical tests may not be applicable or practical.

Resampled data sets are created by randomly resampling from the original data set, with replacement. These are created to be the same size as the original data set. For each of these resampled data sets, the statistic of interest can be calculated. This results in a distribution of the statistic over the resampled data sets. Using this distribution, a confidence interval for the value of the statistic can be created using the percentile bounds:

$$[\Theta^*_{(\alpha/2)}, \Theta^*_{(1-\alpha/2)}] \tag{2.1}$$

where $\Theta^*_{(1-\alpha/2)}$ denotes the $1-\alpha/2$ percentile of the ordered bootstrapped statistic values Θ^* for a confidence level α.

This confidence interval can be used to compare statistics between two data sets. With the null hypothesis being that the statistic is the same for both

data sets, it can determined whether or not the confidence interval of the difference covers this. Resampled data sets are created from each of the data sets. Using a resampled data set from each of the intial data sets, the difference between the statistic of each is caculated. Repeating this process over the pairs of resampled data sets calculates the bootstrap distribution. If the confidence interval for the difference between the two values of the statistic does not contain 0, the null hypothesis can be rejected. This supports the conclusion that the statistic is different with the confidence level used in the tests.

2.4.1 Bias Corrected and Accelerated Confidence Interval

Instead of using percentiles based on the confidence level, a better method is to use bias-corrected and accelerated (BCa) intervals (Efron 1987, DiCiccio & Efron 1996). This method contains adjustments for the bias and skewness in the bootstrap distribution. The percentile values in the confidence interval are replaced with the following:

$$\alpha_1 = \Phi\left(\hat{z}_0 + \frac{\hat{z}_0 + \Phi^{-1}(\alpha)}{1 - \hat{a}(\hat{z}_0 + \Phi^{-1}(\alpha)}\right) \tag{2.2}$$

$$\alpha_2 = \Phi\left(\hat{z}_0 + \frac{\hat{z}_0 + \Phi^{-1}(1-\alpha)}{1 - \hat{a}(\hat{z}_0 + \Phi^{-1}(1-\alpha)}\right) \tag{2.3}$$

where $\hat{z}_0$ is the bias correction, $\hat{a}$ is the acceleration characteristic and Φ is the standard normal distribution. When $hatz_0 = \hat{a} = 0$ it gives the standard percentile bounds detailed in the previous section.

The bias correction, $\hat{z}_0$, gives a correction for any bias in the data set. It is based on the proportion of resampled data sets that have a lower value for

the statistic than in the initial data set. It is calculated as follows:

$$\hat{z}_0 = \Phi^{-1}\left(\frac{\#\{\hat{\Theta}^*(b)\} < \hat{\Theta}}{B}\right) \tag{2.4}$$

where $\hat{\Theta}$ = actual value of the statistic from the original sample, $\hat{\Theta}^*(b)$ = value of the statistic from bth bootstrap resample, and B = number of bootstrap samples.

The acceleration characteristic, $\hat{a}$, is a measure of the skewness of the data. It is calculated using kacknife values of the estimate of the statistic. To create a jackknife sample the statistic is recalculated using all but one data point, removing each in turn. The acceleration is calculated using the difference between the mean of the jackknife samples and each individual sample:

$$\hat{a} = \frac{\sum_{i=1}^{n}(\hat{\Theta}_{(.)} - \hat{\Theta}_{(i)})^3}{6\{\sum_{i=1}^{n}(\hat{\Theta}_{(.)} - \hat{\Theta}_{(i)})^2\}^{\frac{3}{2}}} \tag{2.5}$$

where n = the number of jackknifed samples, $\hat{\Theta}_{(i)}$ = the value of the statistic calculated on the jackknifed sample with the i^{th} value removed, $\hat{\Theta}_{(.)}$ = the mean of the n jackknifed samples.

2.5 Model Fitting

Cell polarity models were fitted to the *Dictyostelium* repolarisation data using the MATLAB toolbox PottersWheel (Maiwald & Timmer 2008). The models are spatial reaction-diffusion models consisting of coupled PDEs with two or three variables. These are considered to be on the cell cortex or in the cytosol depending on how the model is formulated. In each model one

variable indicates the polarisation. This is fitted to the cortex fluorescence values measured from the F-actin reporter in the flow experiments outlined in 2.3.1.

2.5.1 Model Discretisation

In order to fit these PDE models in PottersWheel it is necessary to transform them into a series of coupled ODEs. This is achieved through the discretisation of the cell cortex into a series of equidistant nodes, as illustrated in Fig 2.4. The discretisation used 20 nodes. The number of nodes that could be used was limited by PottersWheel, with larger numbers of nodes requiring more model reactions than PottersWheel was able to implement. As cells are aligned with the shear flow and do not exhibit much variation in shape the system further simplified by not considering the movement of the cell cortex, considering it instead to be fixed in space.

To allow diffusion between adjacent nodes a second order finite difference approximation of the diffusion operator was used, $\partial^2 C/\partial x^2 \approx (C_{i-1} - 2C_i + C_{i+1})/(\Delta x)^2$, where C_i, C_{i-1} and C_{i+1} denote the intensity at point i and to the immediate left and right. To link the two end nodes, periodic boundary conditions were used, with $C_0 = C_{20}$ and $C_{21} = C_1$ for diffusion. A cell circumference of 30µm was used during fitting, which corresponds to a cell diameter of 9.55µm. This resulted in chord length of $\Delta x = 1.5$µm between adjacent nodes.

2.5.2 Data for Fitting

The cortical fluorescence measurements of each cell were obtained using QuimP. This resulted in a series of 200 fluorescence measurements around the cortex for every time point in the image series. In order to reduce this to

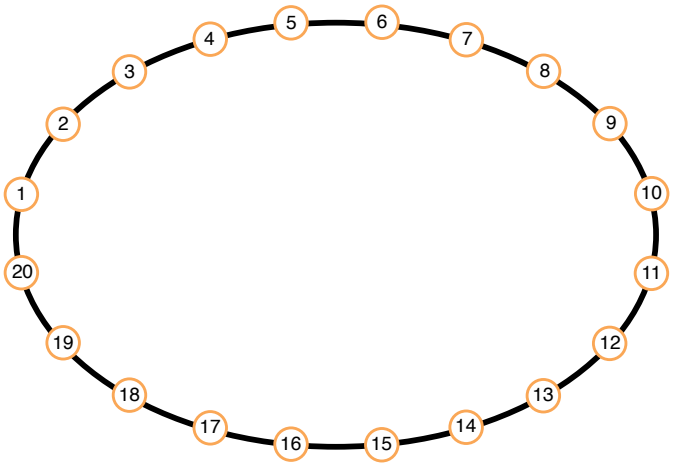

Fig. 2.4: **Schematic of discretisation.** The cell cortex is approximated using a series of 20 linked nodes. The nodes are evenly spaced around around the cortex, with adjacent nodes linked via diffusion.

a series of 20 nodes, the mean of every 10 nodes was used as the fluorescence values for fitting.

Models were fitted either to single cell or to mean population data. When fitting to single cell data, models were fitted to the averaged 20 node data for the cell in question. When fitting to population data, cells were fitted to the mean fluoresence values over the 20 nodes. To generate the mean values, fluorescence data were aligned using the flow change as a common point of reference. Using this point to indicate $T = 0$, for each time point where data existed the mean was calculated from the measurements taken at that point, both before and after the flow change. As cells were imaged over different lengths of time, the number of cells used to construct this mean varies over the course of the data. All mean data points were generated using at least 50% of the cells exposed to that condition. For each mean data point a corresponding standard deviation was calculated from the fluorescence values used the calculate the data point.

When fitting to the *Dictyostelium* repolarisation data from Dalous et al. (2008), the data are separated into 4 conditions; reversal of flow direction for 2.1Pa and 0.9Pa, removal of flow after a period with flow, and beginning flow after a period without flow.

2.5.3 Model Fitting in PottersWheel

Models were fitted in the MATLAB toolbox PottersWheel, a toolbox for model fitting and analysis (Maiwald & Timmer 2008). Once a model is imported into PottersWheel it can be combined with data for fitting using numerically fast integration algorithms based on FORTRAN and C MEX ODE files. Inbuilt model analysis tools can be used for further analysis of the fitted models.

Models were loaded through PottersWheel model definition files. These specify the model in terms of reactions and their components: Dynamical Variables, Reactions, Compartments, Dynamical Parameters, Driving Inputs, Observables and Scaling Factors. These files can either be created using the PottersWheel model creation wizard or through writing the files directly. A MATLAB script was created to generate suitable model definition files for all models used in the fitting. These model definition files can be found in appendix B.1. The reactions used were those corresponding to the ODE representation of the model over 20 nodes.

PottersWheel contains a range of solvers for model integration. During model fitting, the solver RADAU5 was used (Hairer & Wanner 1996). It uses an implicit Runge-Kutta method of order 5, and is suitable for use on stiff systems. It is also compatible with the fast FORTRAN integration capability included in PottersWheel. During use of the PLE package (2.6), the sundials stiff solver cvodes (Hindmarsh et al. 2005) was used for integration.

For model simulations post fitting, models were implemented in MATLAB using the stiff solver ode15s.

The metric which the fitting attempted to minimise was the chi-squared sum of squared errors difference between the model and the data, namely:

$$\chi^2 = \sum_{i=1}^{N} \frac{(y_{model}(i) - y_{meas}(i))^2}{\sigma^2_{meas}(i)}, \tag{2.6}$$

where N is the number of data points, $y_{model}(i)$ is the value given by the model at point i, with $y_{meas}(i)$ being the value of the data at point i, and σ^2_{meas} is the standard deviation in the measurement of data point i. If no standard deviation is available for the data, then a substitute error is calculated, using

$$\sigma_{meas}(i) = 0.1 \times y_{meas}(i) + 0.05 \times max(y). \tag{2.7}$$

This corresponds to a 10% relative error with 5% error relative to the maximum. This was minimised using the recommended Trust Region optimisation method (Coleman & Li 1996, Coleman & Verma 2001). Models were fitted in log parameter space.

When fitting the models in PottersWheel there were two types of parameter, rate constants and the initial conditions for the model species. To remove any dependency on the initial values of parameters during fitting, models were fitted over multiple iterations. Before each iteration each model parameter was disturbed so each fitting began from a distinct parameter set. This process was followed for 15-25 times and the fit with the lowest chi-squared score selected. During each fit, PottersWheel fitted the value of the rate constants and the initial conditions for the model species. As the models were implemented on a series of 20 linked nodes, each node was allowed to

have a different starting value for each model species that varied over the cell cortex.

An important feature of PottersWheel is the ability to fit a model to several data sets simultaneously. This enables more accurate parameter estimates to be obtained. A parameter can be specified as local (has a different fitted value corresponding to each data set) or as global (has the same value for each data set). Local parameters correspond to components that vary for different experimental conditions, whereas global parameters correspond to components that remain unchanged over the different conditions. All rate constants were set to global, except for terms dealing with the strength of the external signal, which was set as a local variable. The initial conditions for model species were also set as local variables.

2.6 Parameter Profile Likelihood Estimation

The Profile Likelihood Estimation (PLE) toolbox (Raue et al. 2009) was used to determine parameter identifiability. This is included in PottersWheel, using the same model implementation and data as used for model fitting. The PLE method exploits the maximum likelihood interpretation of the sum of squared errors by determining how it changes as parameters are varied. Starting with the best model fit, parameters are varied in turn and the model refitted with the new parameter value. The resulting change in the χ^2 value for the model determines what identifiability type can be assigned to the parameter.

To generate a profile likelihood for a parameter p_i, the parameter is iteratively varied about its optimum value and the remaining model parameters refitted after each variation. By tracking the resulting χ^2 values for each fit the profile likelihood is generated. To obtain a confidence interval,

thresholds are determined for the change in the profile. The thresholds are determined based on the $\chi^2(\alpha, df)$ distribution, the α quantile of the χ^2 distribution with df degrees of freedom. α was set to to default confidence level of 68%, corresponding to one standard deviation. df was set to either 1, for pointwise confidence intervals, or the number of parameters for simultaneous confidence intervals. These thresholds give a region bounded by the threshold based confidence intervals.

The existance, or lack thereof, of limits to this confidence interval indicates the identifiability of the parameters. If a parameter has a finite confidence interval then it is identifiable. If one or both of the limits are infinite then the parameter is unidentifiable. Examples of this are illustrated in Fig. 2.5, where the change in the χ^2 values as the parameter is varied are plotted along with markers for the two threshold values. For an identifiable parameter, Fig. 2.5 A, the χ^2 values cross the threshold above and below the fitted value, giving a finite confidence interval. For a structurally unidentifiable parameter, Fig. 2.5 B, the χ^2 values do not cross the thresholds. For a practically unidentifiable parameter, Fig. 2.5 C, the χ^2 values cross the threshold in one direction, but not in the other. Finite limits on the confidence interval occur only when the χ^2 values are able to cross the threshold. This mehod was implemented on fitted models coupled with the data used in fitting. To ensure that the χ^2 profile was successfully calculated and no behaviour missed, when the χ^2 profile did not cross the thresholds, the limit on the maximum number of steps was increased from the default value and the analysis redone for that parameter to ensure that an increase in the likelihood had not been missed due to an inadequate number of steps. During this, other possible variables were kept at the default values. If any better fits were located during the analysis then the new parameter values replaced

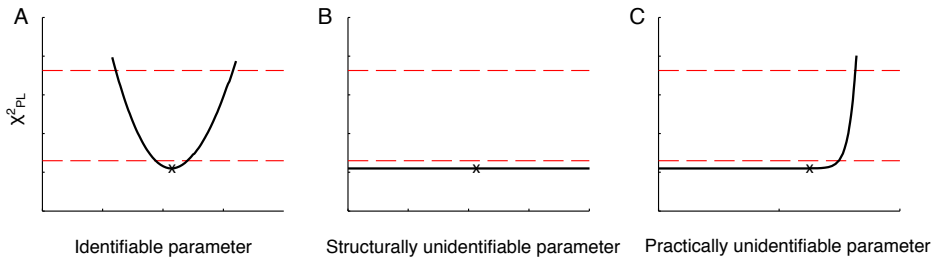

Fig. 2.5: **Possible parameter identifiability results.** The PLE method has 3 different possible outputs for each parameter. In each example the black line shows the change in the χ^2 as the parameter is varied. Cross indicates the parameter value found during fitting. The two red dashed lines indicate the threshold levels, lower for pointwise confidence interval, higher for the simultaneous confidence interval. (A) For an identifiable parameter, the plot crosses the threshhold in both directions. (B) For a structurally unidentifiable parameter the plot is flat and does not cross the threshold in either direction. (C) For a practically unidentifiable model, the plot crosses the threshold in only one direction.

the previous values and the PLE analysis restarted.

2.7 Mathematical Models

For model fitting I used 3 different mathematical models: one of the first cell polarity models proposed by Meinhardt (1999), a local excitation, global inhibition (LEGI) model proposed by Levchenko & Iglesias (2002), and a substrate depletion model proposed by Otsuji et al. (2007). These models provide a range of different behaviours and mechanisms that can be tested against the repolarisation behaviour that has been observed experimentally. For each model, the component that represents the polarisation of the cell was fitted to the actin fluorescence data taken from *Dictyostelium*, Section 2.5.2 . As these are normalised fluorescence values they do not have units, all model species will be considered unitless to match the species that are fitted. The time scale and cell dimensions are defined, so the units of parameters will be affected by these.

2.7.1 External Signal

In each model there needs to be a term that represents the external signal. The strength of this varies around the cell cortex, being strongest where the cortex is closest to the signal source, and weakest on the opposite side of the cell. To represent this I followed Meinhardt's example of using a cosine curve to allow a gradient of input signal over the cell cortex x (Meinhardt 1999);

$$s(x) = r_a(1 + dy \times cos(2\pi(x - y))(1 + drRND) \tag{2.8}$$

Here y is the point closest to the point where the signal is strongest, dy is the assymetry of the external signal, and r_a is the production of the activator. dr is the strength of random fluctuations. The parameter dy governs the strength of the external signal, the greater it is the stronger the signal felt by the cell. When there is no signal, it is set to zero. During model fitting, it was fitted as a local parameter, having a different value for each condition to which a model was fitted. As it is zero in the absence of flow, values obtained during fitting are only for periods when flow is present. As fitting in PottersWheel does not allow the use of random terms, $drRND$ was omitted from the signal function during fitting.
This external signal was used in all three models used during fitting.

2.7.2 Meinhardt Model

One of the first approaches towards creating a simple model that showed some of the characteristics of cellular polarisation was by Meinhardt, using a system based on Turing patterns (Meinhardt 1999). The role of the model was to account for the directional sensitivity of chemotactically sensitive

cells. An external signal, such as a chemoattractant gradient, imposes a directional preference onto the cells pattern formation system.

The model consists of an autocatalytic activator, coupled to two inhibitors. The concentration of the activator indicates the direction of the polarisation. One inhibitor diffuses rapidly over the cell, where as the other acts more locally. The rapidly difussing inhibitor is set to be the same over every node in the cell cortex. This uniformity over the cell cortex motivates naming it as the global inhibitor. The role of the global inhibitor is to prevent the formation of fronts of activation at locations other than where the external signal is strongest. The function of the other, local, inhibitor is to destablises established fronts so that the orientation can change with any changes in the external signal.

This allows the model to replicate several features exhibited by chemotactic cells, including random polarisation in the absence of external signals, the generation of a stable cell polarity in the presence of a maintained signal and responding to a change in the external signal. Simulations in the absence of signal showed out of phase oscillations and travelling waves of activation, similar to those seen in unstimulated *Dictyostelium* cells (Killich et al. 1993, 1994).

A possible candidate considered for the activator was calcium induced calcium release, with a corresponding global inhibitor being the rapid efflux of H^+ ions to maintain the electrical neutrality of the cell. For the local inhibitor, the closing of the inositol 1,4,5-triphosphate receptor Ca^{2+} channel at high Ca^{2+} concentrations was proposed. Together these form a system of an autocatalytic activator, with two inhibitors working on different scales.

The model equations are given by:

$$\begin{aligned}
\frac{\partial a}{\partial t}(x,t) &= \frac{s(x)(\frac{a^2}{b}+b_a)}{(s_c+c)(1+s_a a^2)} - r_a a + D_a \frac{\partial^2 a}{\partial x^2}(x,t) \\
\frac{db}{dt}(t) &= r_b \sum_n \frac{a}{n} - r_b b \\
\frac{\partial c}{\partial t}(x,t) &= b_c a - r_c c + D_c \frac{\partial^2 c}{\partial x^2}(x,t)
\end{aligned} \tag{2.9}$$

where a = activator, b = global inhibitor, c = local inhibitor and n = the number of nodes. D_a and D_c are the diffusion constants for a and c respectively. r_a is the degradation rate of the activator, with b_a the basic production, s_a the saturation and s_c the Michaelis-Menten constant. r_b is the production and degradation rate of the global inhibitor and b_c and r_c are the production and degradation rate of the local inhibitor. $s(x)$ is the external signal from Section 2.7.1. D_a and D_c have the units $\mu m^2 s^{-1}$, and the parameters b_c, r_a, r_b and r_c have the unit s^{-1}.

During model fitting, the activator, a, is fitted the cortex fluorescence values.

2.7.3 Levchenko Model

Levchneko and Iglesias proposed a local excitation, global inhibition (LEGI) model to account for the behaviour of *Dictyostelium* in response to differing gradients of chemoattractants (Levchenko & Iglesias 2002). It consisted of a fast activating local activator and a slow global inhibitor, both activated in response to an external signal. These in turn influence a response element. This was later connected to a stochastic excitable network module (Xiong et al. 2010). The excitable network controls pseudopod fomation, with the LEGI module providing an input that directs where the pseudopods will be forming. The LEGI module was considered to represent the chemoattractant receptor and its associated G-proteins, with the excitable network

representing the downstream Ras and PI3K activations.

Model fitting was conducted using the LEGI module as it is the component that deals with the cell polarisation. A signal drives the production of an activator and an inhibitor, both of which are located on the cell cortex. The response element exists in active and inactive forms, with a fixed total amount and the active form indicating the polarisation. The activator promotes the activation of the response element, whereas the inhibitor promotes its inactivation. On the cell cortex, only the inhibitor diffusses, suppressing further front formation.

The model equations are given by:

$$\begin{aligned} \frac{\partial A}{\partial t}(x,t) &= k_A s(x) - k_{-A} A \\ \frac{\partial I}{\partial t}(x,t) &= k_I s(x) - k_{-I} I + D_I \frac{\partial^2 I}{\partial x^2}(x,t) \\ \frac{\partial R}{\partial t}(x,t) &= k_R A(R_T - R) - k_{-R} I R \end{aligned} \tag{2.10}$$

where A = activator, I = inhibitor and R = response element. D_I is the diffusion constant for the inhibitor I. k_A and k_{-A} are the rate constants for the production and degradation of A, k_I and k_{-I} are the rate constants for the production and degradation of I and k_R and k_{-R} are the rate constants for the production and degradation of R. R_T is the total amount of the response element and $s(x)$ is the external signal from Section 2.7.1. D_I has the units $\mu m^2 s^{-1}$, and all rate constants $k_{()}$ have the unit s^{-1}.

During model fitting, the response element, R, is fitted the cortex fluorescence values.

2.7.4 Otsuji Model

Otsuji et al. (2007) proposed a mass-conserved activator-substrate model based on the similarities of the behaviour of models of Rho-GTPases and phosphoinositides (Narang et al. 2001, Subramanian & Narang 2004). In both models, the total amount of reactants were conserved between the cell membrane and the cytosol and endoplasmic reticulum, for Rho-GTPases and phosphoinositides respectively. Both models were reaction-diffusion systsems that exhibited a switch-like response, responding to the presence of an external signal and having no response during its absence.

A conceptual model was developed to replicate these properties. It consists of one species which has two states, active (u) and inactive (v). These are both localised to the membrane and diffuse around it. The substrate becomes active at a constant rate, but the rate at which it becomes inactive is mediated by the strength of the external signal, with a stronger signal resulting in a slower rate of degradation. This allows a localisation of the area of activation to the area closest to the signal.

This model was able to replicate the behaviour seen in the Rho-GTPase model; a switch like response to the external signal, selecting a unique front in the presence of multiple signals and responding to a change in the signal by movement of the polarisation front.

The model equations are given by:

$$\begin{aligned} \frac{\partial u}{\partial t}(x,t) = & \quad a_1 \left[v - \frac{u+v}{(a_2 s(x)(u+v)+1)^2} \right] + D_u \frac{\partial^2 u}{\partial x^2} \\ \frac{\partial v}{\partial t}(x,t) = & \quad a_1 \left[\frac{u+v}{(a_2 s(x)(u+v)+1)^2} - v \right] + D_v \frac{\partial^2 v}{\partial x^2} \end{aligned} \tag{2.11}$$

where u and v are the active and inactive form respectively. D_u and D_v are the diffusion constants for the two states, a_1 and a_2 are model parameters

and $s(x)$ is the external signal from Section 2.7.1. D_u and D_v both have the units $\mu m^2 s^{-1}$, and a_1 has the unit s^{-1}.

During model fitting, the active form, u, is fitted the cortex fluorescence values.

3. ACTIN/MYOSIN DYNAMICS IN DICTYOSTELIUM

This chapter presents experimental work with *Dictyostelium* and image analysis of *Dictyostelium* fluorescence images. Developed *Dictyostelium* were exposed to pulses of the chemoattractant cAMP, to confirm cells had developed. The response was imaged and analysed.

Bosgraaf et al. (2009) demonstrated several analyses of cell cortex fluorescence data taken from *Dictyostelium*, including of cAMP response and of the correlation between cortex fluorescence and protrusion. These were demonstrated on data from a single cell. Using fluorescence data obtained from QuimP analysis on vegetative and developed cells the analysis was extended to populations of cells.

In the following chapters mathematical model of cell polarity will be fitted to cortex fluorscence data taken from *Dictyostelium* repolarising in response to shear flow reversal. This repolarisation data were collected by Jérémie Dalous and presented in (Dalous et al. 2008) . The flow chamber apparatus detailed in Section 2.3 was used to try and replicate these experiments in order to provide more data and experimental conditions for model fitting and validation.

3.1 cAMP response of developed Dictyostelium

Development in *Dictyostelium* cells was induced with regular pulse of cAMP, with a frequency of once every 6 minutes. When cells are developed they

respond to a pulse of cAMP through localisation of actin and myosin-II to the cytoskeleton (Etzrodt et al. 2006, McRobbie & Newell 1983). This was done with the double-tagged LimE/GFP-myosin-II strain of *Dictyostelium* cells. Attempts to replicate this with the single tagged ABP120 cell strain were unsuccessful.

When exposed to the pulse of cAMP, there is a localisation of the actin and myosin reporters to the cell cortex, Figure. 3.1 A,B. The actin response has 2 peaks 35s apart, with the myosin peak occurring between them. The first actin response is of greater intensity than the second and the myosin response, and is present for a shorter length of time before decreasing. During the first actin response, there is a decrease in the myosin cortical fluorescence.

The mean response of multiple (10) cells was calculated, Figure 3.1 C. The first actin peak is visible, peaking 5-8s after the cAMP pulse. The second actin peak is not visible in the mean data. The myosin peak is also visible in the mean response.

The single cell response shows a cleaner spike than that seen in the mean cell response, instantly reducing intensity after the reaching the fluorscence peak. In the mean cell data, the peak remains constant for 2 image frames, before it decreases. This widening of the first response is likely due to slight variations in the time that cells were exposed to cAMP. As the peak is relatively narrow, differences in the time that cells are exposed to cAMP of 1 image frame (1.65s) would cause noticeable widening.

3.2 Node Speed and Fluorescence

The analysed QuimP data was used to determine what relationship exists between the node speed and the fluorescence value. Actin and myosin are

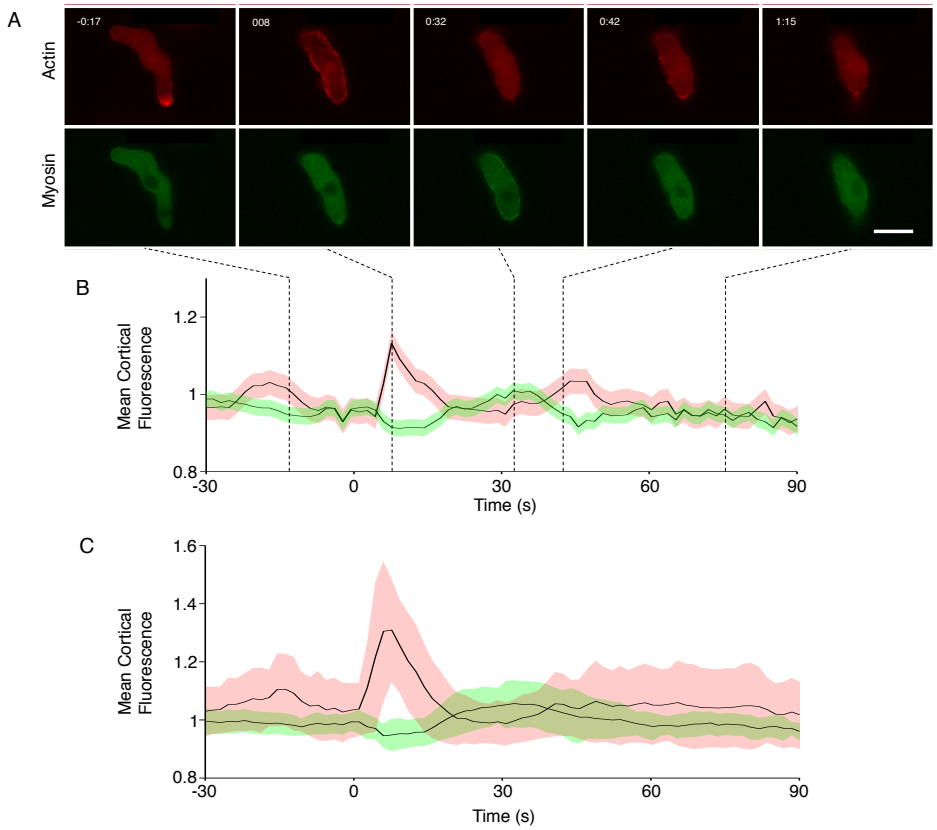

Fig. 3.1: **Response of developed *Dictyostelium* to cAMP.** Development in dual-tagged *Dictyostelium* was induced using cAMP pulses. (A) During imaging cells were exposed to another pulse of cAMP at time $t = 0$. This induced a response from the actin and myosin reporters, with greater localisation to the cell cortex. Scale bar $10\mu m$. (B) Mean cortical fluorescence taken from A, red and green show the actin and myosin reporter respectively. Shaded area indicates the standard deviation. (C) Mean cortical fluorescence taken from the response of 10 cells to a pulse of cAMP, red and green show the actin and myosin reporter respectively. Shaded area indicates the standard deviation of this mean.

involved in cell protrusion and retraction, so the log of the ratio of actin/myosin fluorescence was compared with the node speed. By using the log of the ratio, positive values correspond to areas where there is a higher concentration of the actin reporter, with negative values corresponding to nodes where there is a higher concentration of the myosin reporter.

The data was split into bins based on the value of the fluorescence ratio. There were 16 bins of width 0.125 covering the range -1 to 1. Bins will be referred to using the numbers 1-16, as opposed to the range the bin covers. The mean node speed for each bin was calculated using the values taken from the nodes whose log fluorescence ratio was within the bin limits. Positive node speeds correspond to protrusions, with negative speeds corresponding to retractions.

To compare bins to each other I used the bootstrap comparison method outlined in Section 2.4. The means of the bins were compared at the confidence levels of 95%, 90% and 75% using the BCa intervals, with the null hypothesis being that the means of both bins were the same. The confidence intervals were calcualted for every pair-wise combination of bins.

Populations of vegetative and developed double-tagged *Dictyostelium* were analysed in this way, as opposed to analysis of a single cell (Bosgraaf et al. 2009).

3.2.1 *Vegetative* Dictyostelium

Several nodes were found to have a speed greater than $4\mu ms^{-1}$. From observations on the spread of node speeds, these were designated as outliers and removed. Four such nodes were removed out of 3.9×10^5 nodes used, less that 0.001%. The results of separating nodes by their fluorescence value are shown in first row of Figure 3.2. The resulting plot is diamond shaped

with concave edges, with the points following the axes of the node speed and log fluorescence ratio. This indicates that the nodes with the smallest node velocity have the greatest range in values of the log fluorescence ratio, and those with a log ratio close to zero have the greatest range in node speed. There is a greater spread in the top half of the diamond, for nodes with a speed greater than zero.

There is a correlation between node speed and log fluorescence value. Nodes that have a positive log ratio have positive node speed, and nodes that have a negative log ratio have a negative node speed. This implies higher actin for protrusion and higher myosin for retraction. The means of the first 5 bins with a positive fluorescence ratio increase with a linear rate of 8.46×10^{-2}. A bin to bin comparison using the bootstrap method was used to see if the mean value for each bin is statistically different to the others, testing at 95%, 90% and 75% confidence intervals. With the vegetative data, 3 bins (the leftmost) are empty of data and not considered for the purposes of bin comparison. The results are shown in the bottom row of Figure 3.2.

The majority (91.0%) of bins passed the 95% level test. Of the adjacent bins, only bins 15-16 did not pass at 95%. When testing bins at 90% and 75%, 92.3% and 94.9% were able to pass respectively. When considering just adjacent bins, bin number 3 through to bin number 15 were all able to pass at 95%. This includes all bins from which the linear increase was calculated.

3.2.2 *Developed* Dictyostelium

As with the vegetative cells, several nodes were removed as outliers. Nodes with a speed with a magnitude $> 4\mu m$ were removed. This totalled 16 nodes

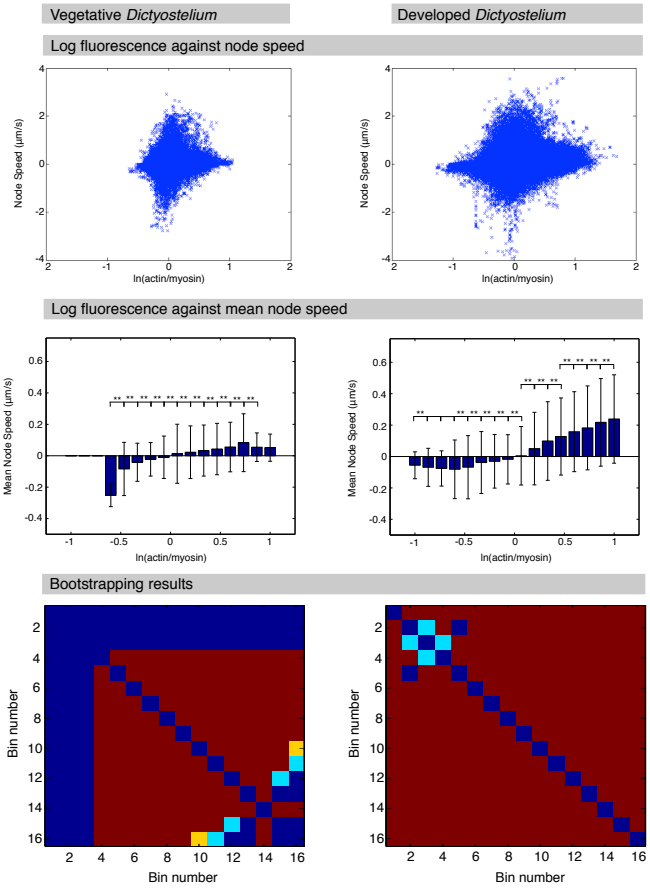

Fig. 3.2: **Actin/Myosin fluorescence values compared with node speed for double tagged *Dictyostelium* cells.** Cortex fluorescence data from vegetative and developed *Dictyostelium* cells, double tagged with actin and myosin reporters, with no external stimuli, were obtained with the QuimP software. The first row shows a plot of node speed against the log of the fluorescence value ratio. The second row shows the log fluorescence ratio against the mean node speed. The data are grouped into 16 bins, of equal width 0.125, between log fluorescence ratios of -1 and 1. The mean node speed is calculated using all data points whose fluorescence value is between the limits for each bin. Error bars show the standard deviation of the speeds within each bin, *s indicates the result of bootstrap comparison between adjacent bins. The metric tested was the difference between the means. No stars indicates 75% success, * indicates 90% and ** indicates 95%. Lack of a bar between two columns indicates that there was no success from the bootstrap analysis. The third row shows the results of the bootstrapping between bins. Red, yellow and light blue signify passing the bootstrap comparison at 95%, 90% and 75% respectively. Dark blue signifies that it did not pass the test, or was not tested (for the leading diagonal and vegetative bins 1-3). The first column uses data obtained from vegetative cells and the second uses data obtained from developed cells. Data were collected from 11 vegetative cells, with a combined total of 2918 image frames and 391442 nodes, and from 10 developed cell with a combined total of 4443 image frames and 803724 nodes.

out of 8.04×10^5, 2×10^{-3}% of the nodes. Results of the analysis are shown in Figure 3.2. The node spread follows a similar pattern to that observed for vegetative *Dictyostelium*, but with a greater range and spread. The nodes with the greatest range of values again follow the axes for node speed and log fluorescence ratio close to zero.

Using this data from developed *Dictyostelium* there was also a correlation between the log fluorescence value and node speed as seen with the vegetative cells. For the positive log fluorescence values there was a mean increasing linearly with a slope of 0.263, 3 times the rate of increase seen for the vegetative data. The retraction from having myosin is less clear, with a decrease in the mean node retraction as the log fluorescence ratio decreases. The majority (97.5%) of bins passed the bootstrap comparison at the 95% test level. No further bins passed at 90%, but a further two (2-3 and 3-4) passed at 75% to leave 99.2% of bins comparisons passing at the 75% level. The data taken from the developed cells passed the bootstrap test better than those from the vegetative cells, with more bins passing the bootstrap comparison at each level of testing. When considering just adjacent bins, from bin 4 to bin 16, each adjacent bin pair passes the bootstrap comparison at 95%, again including all bins from which the slope was calculated.

The bins that fail the bootstrap comparison are clustered towards the area where the log ratio is lowest. This is opposite to the vegetative cells, where the bins that fail the bootstrap comparison are located towards where the log ratio is highest.

3.3 Flow Chamber

Dictyostelium cells were exposed to shear flow using the Ibidi flow chamber system described in Section 2.3. In Dalous et al. (2008) it was shown that

Dictyostelium cells respond to shear flow by polarising into it in a similar manner to how they respond to a chemotatic gradient. Once flow is removed, this polarisation ends. When using a shear stress between 0.9-2.1 Pa, the majority of cells remain in place and respond to the shear flow.

I aimed to further these experiments using the Ibidi flow chamber system to provide more data for model fitting and to test any possible model predictions. Using a computer controlled air pressure pump to drive the flow, this gives much greater control than the previous system that used gravity to drive flow (Dalous et al. 2008). It allows rapid changes in flow direction and strength, along with long periods of unchanging flow. This would allow the generation of cell polarisation data with a more complex flow pattern.

I attempted to do this using both dual and single-tagged cells. However, I were not able to induce polarisation as in Dalous et al. (2008). Cells did not polarise into flow, and a proportion of cells moved with flow, or became detached from the slide surface. Flow rates were kept between 2-4 ml/min, with a shear stress range of 1-2 Pa. Cells were taken from various stages of development, taken straight from growth media, after having 1-2 hours starvation and after being pulsed with cAMP for 3 or more hours.

Not all cells remained in position when exposed to flow. All extended movement was in the direction of the flow, two examples of which are shown in Figure 3.3. Cell A moved 25µm, and cell B moved 30µm over the 5 minute period over which these images were taken. This gives a cell speed of between 5-6µm per minute, which is within the range of speeds expected (McCann et al. 2014). There was no extended movement against or perpendicular to the flow.

Cells detached from the slide surface at all flow rates and at all levels of development. When some cells detached they could be observed pivoting

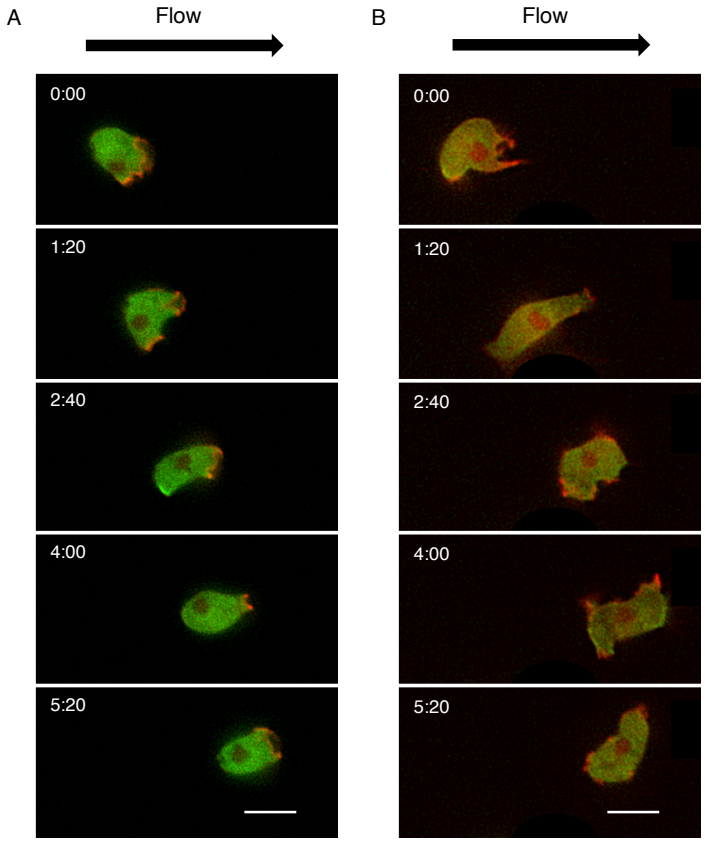

Fig. 3.3: **Cell movement under flow.** Dual-tagged *Dictyostelium* cells were exposed to shear flow in the Ibidi flow chamber system. Some cells did not remain in position, moving with the flow. Flow comes from the left as indicated by the arrow and was present at the beginning of the first image for at least 1 minute. Red and green show the actin and myosin reporter respectively. Scale bar 10µm. (A) Cell moves 25µm under a flow rate of 3ml per minute, generating a shear stress of 1.5 Pa. (B) Cell moves 30µm under a flow rate of 4ml per minute, generating a shear stress of 2 Pa.

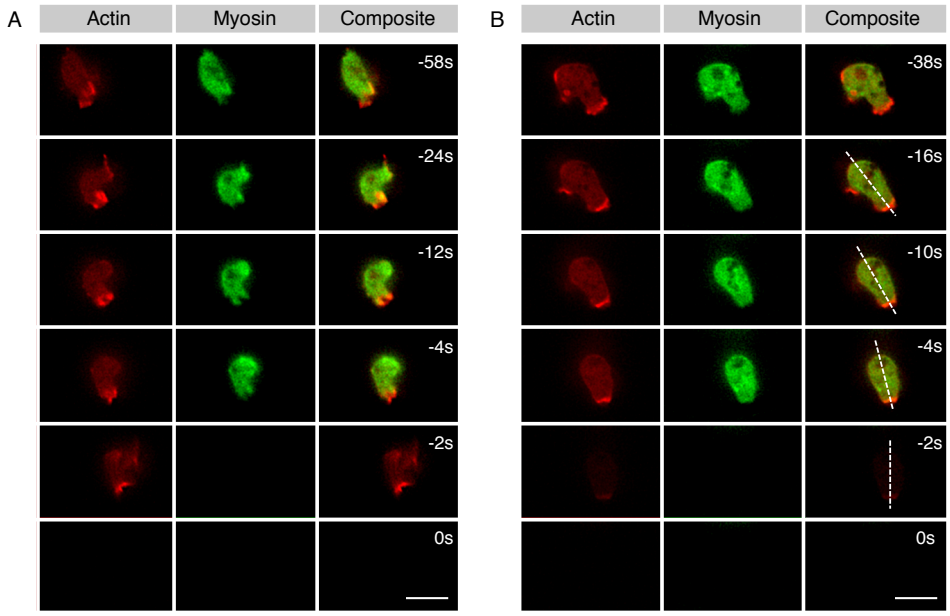

Fig. 3.4: **Cell detachment under flow.** Dual-tagged *Dictyostelium* cells were exposed to shear flow in the Ibidi flow chamber system. Some cells became detached during flow exposure. Flow comes from the left and was present at the beginning of the first image for at least 1 minute, both with a flow rate of 4ml/min, generating a shear stress of 2 Pa. Time $t = 0$ is taken as the point when the cell fully detaches as it is no longer visible on the image. Red and green show the actin and myosin reporter respectively. Scale bar 10µm. The dashed white line indicates the major axis of the cell.

around a point of actin enrichment prior to disappearing, Figure 3.4. For both cells shown there, only the actin reporter could be observed in the last frame before they disappear. Both cells had an area of actin enrichment at the bottom of the cell.

For cell A, it is sending out a protrusion 24s before it detaches. This protrusion then stops, with the cell remaining still until it detaches. The area of actin enrichment at the bottom of the cell remains in the same position until the cell detaches, with the body of the cell moving in the last frame before detachment.

For cell B, there is an area of actin enrichment at the bottom of the cell that remains in the same position. The major axis of the cell (dashed line) rotates clockwise with time, before the cell detaches. Cell detachment during image capture may explain the very faint final image.

Using cell fluorescence data taken from unsitmulated vegetative and developed *Dictyostelium*, the techniques illustrated in Bosgraaf et al. (2009) were implemented on populations of cells. This showed the relationship between the actin/myosin cortex fluorescence ratio and the protrusion/retraction of the cell cortex. The vegetative cell fluorescence data will be used in Chapter 6 for the fitting of cell polarity models to random cell motility. My attempts to replicate and further the cell repolarisation experiments of Dalous et al. (2008) were unsuccessful. Hence all fitting of cell polarity models to repolarisation data will use the data presented in Dalous et al. (2008).

4. MODEL FITTING TO DATA OF DICTYOSTELIUM REPOLARISATION

Comparisons between cell polarity models have been made that focused on the qualitative behaviour of the models and how well they have exhibited various aspects of cell polarity behaviour, (Jilkine & Edelstein-Keshet 2011, Holmes & Edelstein-Keshet 2012). I wished to use a more quantitative method and fit models to repolarisation data of *Dictyostelium*.

Three mathematical models of cell polarity were introduced in Section 2.7, Meinhardt (Meinhardt 1999) (Section 2.7.2), Levchenko (Levchenko & Iglesias 2002) (Section 2.7.3) and Otsuji (Otsuji et al. 2007) (Section 2.7.4). I will begin with providing the details of the diffusion of the inhibitor in the Levchenko model, Equation 2.10, and then the results of the model fitting to the *Dictyostelium* repolarisation data.

Each of these models was implemented in the PottersWheel toolbox (Maiwald & Timmer 2008), with the external signal described in Section 2.7.1. These models were fitted to mean cortical fluorescence data of an actin reporter taken from *Dictyostelium* undergoing repolarisation in response to flow change (Dalous et al. 2008).

The metric that was minimised during fitting was the χ^2 sum of the squared errors difference between the model and the data. The value of the best fit for each model provides a measure by which the fits of the different models can be compared. In addition, the mean relative error between each model

and the data averaged over the number of image frames in the data was calculated. This provides an error measure that is unaffected by the size of the data used for fitting. Both χ^2 and relative error values were calculated for each data condition and for each model as a whole.

Additional qualitative methods can be used to compare model fits. When the direction of flow remains constant the cell can be split into two halves, a 'front' facing into the flow and a 'back' facing away from the flow. When the flow direction is reversed, the two halves swap position. By taking the mean cortical fluorescence from each half of the cell the breakdown and building of actin fronts can be observed. This was done with the model species that was fitted to the cortex fluorescence, allowing a comparison of the relative front formation behaviours. Model fits can also be compared using heat maps, where one axis represents the cortical fluorescence or the fitted species, and the other time. These show the change over the entire cell cortex. Parameter values for the fitted models are in Appendix A. These are tables A.1, A.2 and A.3 for fits to the Meinhardt, Levchenko and Otsuji models respectively.

4.1 Diffusion in the Levchenko Model

In the Levchenko model shown in Equation 2.10, only the inhibitor can diffuse along the cell surface. This was prompted by discussion of the model by Jilkine & Edelstein-Keshet (2011), where the model was formulated as such and it was stated that addition of diffusion to the other two species did not change the behaviour of the model.

I investigated the behaviour of the steady state solution for the model, both with and without diffusion of the inhibitor. In both cases the steady state

for the activator is

$$A_{ss} = \frac{k_A}{k_{-A}} s(x) \tag{4.1}$$

The steady state of the response element depends on the steady state of the activator and inhibitor

$$\begin{aligned} R_{ss} &= R_T \frac{k_R A_{ss}}{k_{-R} I_{ss} + k_R A_{ss}} \\ &= R_T \frac{k_R k_A s(x)}{k_{-R} k_{-A} I_{ss} + k_R k_A s(x)} \end{aligned} \tag{4.2}$$

In the absence of diffusion, $D_I = 0$, the steady state of the inhibitor is

$$I_{ss} = \frac{k_I s(x)}{k_{-I}} \tag{4.3}$$

which gives a steady state for the response element of

$$R_{ss} = R_T \frac{k_R k_A k_{-I}}{k_{-R} k_{-A} k_I + k_R k_A k_{-I}} \tag{4.4}$$

This has no dependence on the external signal $s(x)$, resulting in a flat steady state. This behaviour is illustrated in Figure 4.1 A, where the transient nature of the response is demonstrated. After the external signal appears at $t = 0$, there is an accumulation of the response element opposite the external signal which dies away.

If instead $D_I \neq 0$, the steady state of I is

$$\begin{aligned} I_{ss} =& e^{\gamma x} F_2(t) + e^{-\gamma x} F_1(t) \\ & - \frac{1}{2} \frac{K_I (e^{\gamma x} \int e^{-\gamma x} s(x) dx - e^{-\gamma x} \int e^{\gamma x} s(x) dx)}{\sqrt{D} \sqrt{k_{-I}}} \end{aligned} \tag{4.5}$$

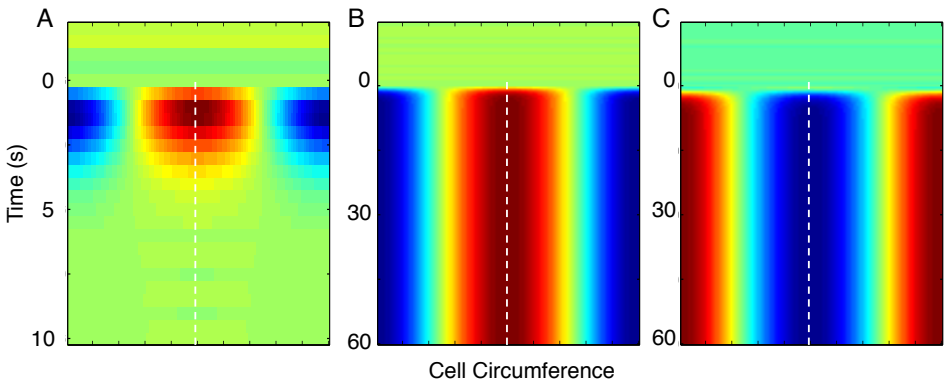

Fig. 4.1: **Varying diffusion of I in the Levchenko model affects the stability of front formation.** The behaviour of the Levchenko model varies depending on the diffusion of the activator and inhibitor. Heat maps show the value of the response element, R, along the cell circumference, with the colour range from red (high) to blue (low). The white dashed line shows the point opposite the external signal, which is present from time $t = 0$ onwards. (A) No diffusion of both the inhibtor and activator. (B) Diffusion of the Inhibitor. (C) Diffusion of the Activator.

where $\gamma = \sqrt{\frac{k_{-I}}{D_I}}$ and $F_1(t)$ and $F_2(t)$ are functions of t depending of the initial conditions. This solution was obtained using the Maple software.

Substituting this into Equation 4.2 gives the steady state for the response element when $D_I \neq 0$;

$$\begin{aligned} R_{ss} =& \frac{k_R A_{ss} R_T}{k_R A_{ss} + k_{-R} I_{ss}} \\ =& \frac{k_R k_A s(x) R_T}{k_R k_A s(x) + k_{-R} k_{-A} (e^{\gamma x} F_2(t) + e^{-\gamma x} F_1(t)) \\ & - \frac{k_I}{2\sqrt{D_I}\sqrt{k_{-I}}} (e^{\gamma x} \int e^{-\gamma x} s(x) dx - e^{-\gamma x} \int e^{\gamma x} s(x) dx)} \end{aligned} \tag{4.6}$$

This steady state has a dependence on s, resulting in a non-transient response to the external signal. This is illustrated in Figure 4.1 B, which shows the stable front forming after the appearence of the external signal at $t = 0$.

Given the similarities between the activator and the inhibitor formulation, adding diffusion to the activator will also result in a steady state for the re-

sponse element that is dependent on $s(x)$. However, simulations show that though this has the effect of removing the transcience of the response to the external signal, the response is now orientated towards the opposite side of the cell to that of the signal point, Figure 4.1 C. This can be explained by the activator diffusing away from the signal, whereas the inhibitor does not. This results in production of the response element on the opposite side of the cell.

4.2 Fitting to Four Conditions

The models were first fitted to all four *Dictyostelium* flow reversal conditions: high shear stress, low shear stress, flow to no-flow and no-flow to flow, (Dalous et al. 2008). Data were processed for fitting as described in Section 2.5.2 and fitted as described in Section 2.5.3. Each data set was aligned so that time $t = 0$ corresponded to the time of flow reversal, switching on or switching off of the flow. The resulting start and end times for each data set are shown in table 4.1. The 4 conditions together total 414 time points of data.

	High Stress	Low Stress	Flow → No Flow	No Flow → Flow
start (s)	-18	-24	-153	-213
end (s)	189	153	282	198

Tab. 4.1: Start and end times for *Dictyostelium* repolarisation data used in model fitting in Section 4.2. Time $t = 0$ corresponds to the point where the flow either changes direction or turns on or off.

Each model was fitted to all data sets simultaneously, with parameter values being conserved between all data sets. The exception to this is dy, the measure of the asymmetry of the external signal, Equation 2.8. This vari-

		High Stress	Low Stress	Flow → No Flow	No Flow → Flow	Total
Meinhardt	χ^2	275	515	267	298	1354
	mean RE	3.91	3.77	3.04	3.37	3.40
Levchenko	χ^2	64.1	140	139	294	637
	mean RE	2.03	2.30	2.31	3.25	2.57
Otsuji	χ^2	109	210	161	215	695
	mean RE	3.09	3.30	2.65	3.11	2.97

Tab. 4.2: χ^2 and relative error values for models fitting to *Dictyostelium* repolarisation data. The χ^2 value is the chi-squared sum of squared errors difference between the model and the data. The mean RE value is the relative error of the model fit averaged over the number of image frames in the data set.

able has a different fitted value corresponding to each data set it is fitted to. The metric minimised during fitting, was the χ^2 sum of errors, Equation 2.6. This is dependent on the data points available for fitting. In order to compare fits to data sets of differing lengths, the mean relative error was calculated for each data set and for all sets combined. It is the mean error for each data set, averaged over the number of image frames in that data set. This gives a measure independent of the length of the data set from which it is calculated.

All three models are able to fit to the data. The χ^2 and mean relative error values for each fit are shown in table 4.2. The Levchenko model has the best fit, with a χ^2 value of 637 and a mean relative error of 2.57. These are lower than the values for either the Meinhardt or the Otsuji models, which have χ^2 values of 1354 and 695 and mean relative errors of 3.4 and 2.97 respectively.

The χ^2 value and mean relative error can be calculated for each individual condition, as opposed ro the entire data set. This shows which conditions models are best at fitting to, and which contribute the most to the error.

With the Meinhardt model, the high and low shear stress conditions contribute the most to the error. These have a higher mean relative error than the other two conditions. For the Levchenko model, the fit to the no-flow to flow condition has the highest error, with the mean relative error highest here by 0.95, an increase of 41.3% over the next highest value. The Otsuji model is best at the fitting to the flow to no-flow condition.

The Levchenko model is best at fitting to all conditions on both metrics except for no-flow to flow, where the Otsuji model fits best. The range of values for the error varies the least over this condition (χ^2 range of 83, mean relative error range of 0.26), showing the fits here are closest to each other in quality.

By splitting the cell into two halves based on its orientation into or away from the flow and comparing mean cortical fluorescence the formation and degradation of actin fronts can be observed, Figure 1.1, (Dalous et al. 2008). The same process is performed with the fitted models and the results compared. The half of the cell facing into the flow during $t \geq 0$ is labelled the 'front', with the opposite side being labelled as the 'back'. In the flow to no-flow condition, where there is no-flow for $t \geq 0$, the front is the half of the cell facing into flow for $t \leq 0$. The results of this are shown in Figure 4.2, with the front coloured red and the back in black. For the two different shear stresses, different behaviour is observed in the speed at which the new front forms. When under the high shear stress there is a delay (30s) in the formation of the new front that is not observed when cells are experiencing the lower shear stress. With the flow to no-flow condition the mean fluorescence in the front and back tended to the same value as expected, and with no-flow to flow the formation of a clear actin front once flow begins can be observed. The standard error for each half of the cell is shown in the shaded

area around the line indicating the mean values. This differs from the error used during fitting, which was the standard deviation of the fluorescence values for each node, as detailed in Section 2.5.2.

With the fit of the Meinhardt model the time of flow change can be clearly identified, Figure 4.2. When fitting to the high and low shear stress conditions, the fit does not capture the observed delay in front formation for high shear stress, nor does it capture the plateau of front activation. Instead there is a continuous increase in the front after the flow is switched. In addition, it misses the crossover point between the mean front and back values, with the crossover occuring later for both shear stresses. For both fits the old and new front degrade and form respectively at the same rate. This is contrasted by the data, where the old and new front degrade and form at different rates depending on the shear stress. This difference in the rates of front formation and degradation explain the failure to match to the cross over points. For flow to no-flow, there is a continuous decrease in the front before flow is removed. At the end of the time course, the values for the mean of the front and back are approaching the same value, as observed in the data. With no-flow to flow, the fit begins with a larger value in the half that will become the front, before gradually decreasing towards the same value as the back. Once the flow begins the back value decreases, with an increase in the front.

With the fit of the Levchenko model, it is not as apparent when the flow changes as with the Meinhardt model. For the high and low shear stress fits, it has not captured any of the period of initial activation that dies away before the new front forms. Instead the old front immediately begins to degrade. This implies that the model has fitted as if the polarisation change happens at the beginning of the time series, not at time $t = 0$. Despite this,

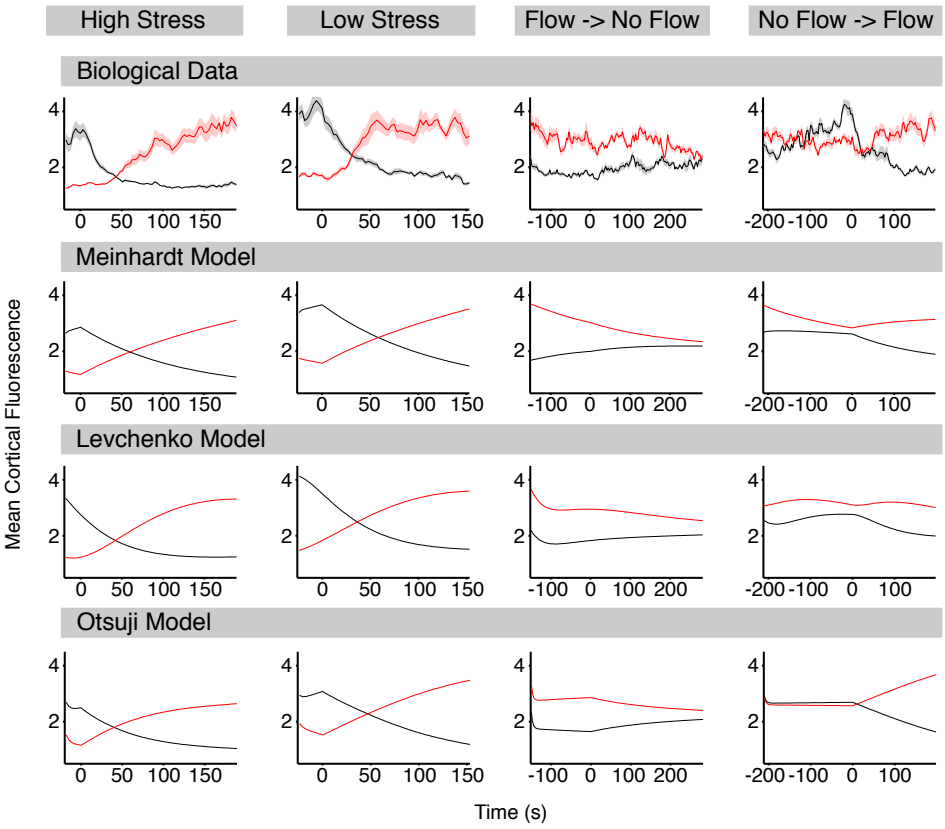

Fig. 4.2: **Comparison of the three mathematical models fitted to *Dictyostelium* repolarisation data.** To provide a comparison between data and model fits each was split into two halves based on the orientation of the external signal, as previously shown in Fig 1.1. For each half the mean was calculated to give the mean cortical fluorescence value. The front half (red line) faces towards the external signal (for $t \leq 0$ in flow to no-flow, $t \geq 0$ in the other conditions), with the back half (black line) facing in the opposite direction. Each column corresponds to a different experiemental condition, as signified by the column headers. The first row shows the repolarisation data, and the remaining three rows shows the fits of the three mathematical models. Shaded area on repolarisation data indicates standard error of the mean. The goodness of fit, χ^2, is 1354, 637 and 695 for the Meinhardt, Levchenko and Otsuji models respectively.

the fit is able to match the crossing point of the old and new fronts for both shear stresses. There is a delay in the formation of the new front for the high shear stress condition compared to the low shear stress. This is not as apparent as what is observed with the data however. The flow to no-flow fit does trend toward both sides having equal value, though it does not reach the point where this is the case. With the fit to the no-flow to flow data there is no clear period where there is no front, followed by the formation of one after the start of flow. There is however a change when the flow begins, with a slight decrease in the level of activation on the side of the cell that is facing away from the flow.

As with the Meinhardt model, the fits of the Otsuji model clearly show the change in flow. When fitting the high and low shear stress conditions, there is a period before the flow changes where it captures the previous front formation. After the flow direction changes, the old front dies away with a new front forming on the opposite side of the cell. For the high shear stress, it fails to capture the delay in new front formation, along with the plateau observed with lower shear stress. For the flow to no-flow condition there is a clear front until flow is removed, and the mean values for each half of the cell approach the same value. For the no-flow to flow condition, whilst there is no-flow both sides of the cell have the same mean value. This is rapidly achieved, in contrast to the fluctuations observed in the data. When flow is introduced, a new front is formed, and the other side of the cell has the activation there reduced. These occur at very linear rates, and do not exhibit the plateauing effect seen in the data, where after the actin front is formed the mean value for the front of the cell remains roughly constant.

In addition, the model fits can be compared to the data using heat maps, where the horizontal axis corresponds to the cell circumference and the ver-

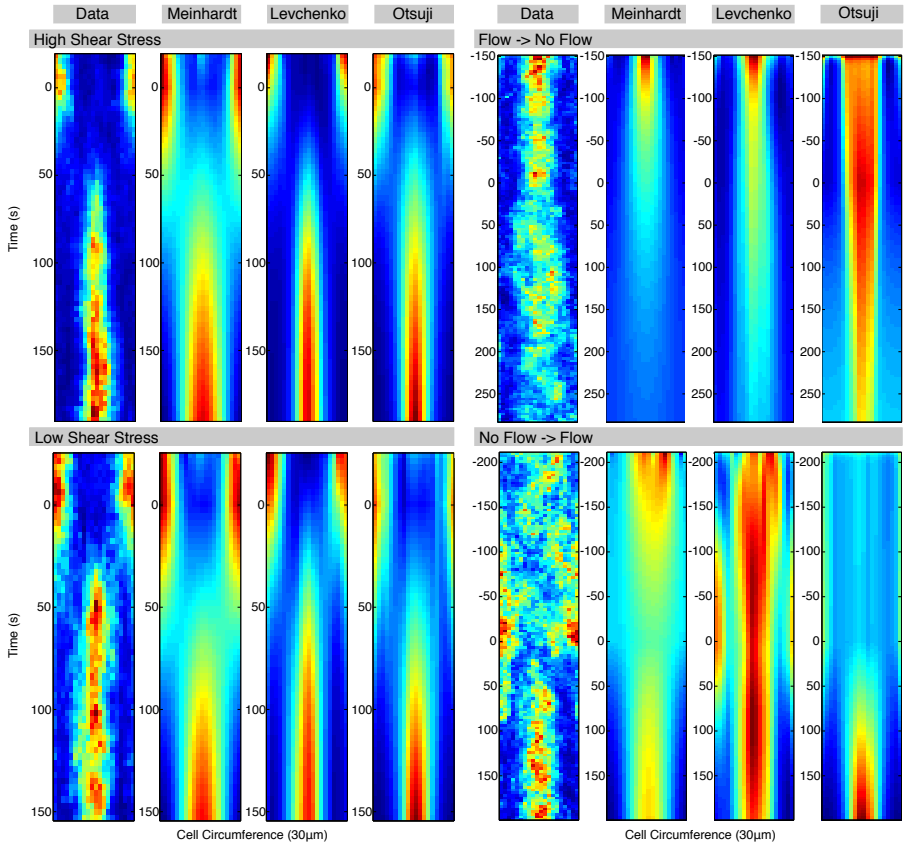

Fig. 4.3: **Heatmaps for *Dictyostelium* repolarisation data and corresponding model fits.** Heat maps are created by taking the fluorescence values for the cell cortex and plotting these over time. Headers indicate the experimental condition and whether the map is of data or which model it is from. The change in flow occurs at time $t = 0$ for all maps. For both shear stress conditions and the no-flow to flow condition, the new position of the external signal is the middle of the plotted cell circumference. In the condition where flow is removed, the external signal was located in the same position before removal. Maps are coloured using the MATLAB heat map Jet, which ranges from blue (low) to red (high).

tical axis corresponds to time. These show the changing levels of activation for the entire time period used during fitting, Figure 4.3.

For the high shear stress condition, all three models can be seen to have an old front that breaks down, and a new front of activation that forms. This is most clear for the Levchenko model. For the Meinhardt and Otsuji fits, the new front is less concentrated. This is more pronounced with the Meinhardt fit. For the low shear stress, the two fronts are less clearly separated. This is replicated in the model fits, with the Meinhardt fit exhibiting this more than the Levchenko or Otsuji fits.

In the flow to no-flow data the old front can be observed to slowly disperse after flow is removed. The Meinhardt fit has a front of activation that decreases throughout the fit. It is most concentrated whilst the flow is happening, and then quickly disperses once it is removed. The Levchenko fit follows a similar pattern, though does not disperse as clearly once flow is removed. With the Otsuji fit, a large front of activation does disperse over time, but not to the extent of the other models. Both the Meinhardt and Levchenko models have large amounts of activation at the start of the fit. This corresponds to a similar peak that can be observed in the data. The Otsuji model starts at a similar level, but does not degrade as with the other models.

In the no-flow to flow data, there is no clear front till after the flow is started, where a front quickly forms. The Otsuji model most clearly shows the most similar behaviour, with a period where there is no front before flow begins, and once flow has begun a clear front is formed. With the Meinhardt model there is a period of activation at the beginning which reduces with time. Once flow has begun a front is formed. In the Levchenko fit, there is a large area of activation that corresponds to the position of the final front

throughout the entire time course. It is more diffuse before flow is begun, with a minor peak of activation on the back of the cell. This corresponds to a peak of activation seen in the data before the flow begins.

To summarise, the Levchenko model achieves the best fit by the numerical metrics calculated from the fitted models, table 4.2. All models have several issues found during qualitative comparisons between the data and the model fits, Figure 4.2 and Figure 4.3. By comparison through heat maps and characterising the front and back behaviour, models are better able to fit the high and low shear stress conditions, as opposed the flow to no-flow and no-flow to flow conditions. This contrasts with the mean relative error, which indicates that for the Meinhardt and Otsuji models, there is a better fit to the flow to no-flow and no-flow to flow data sets than to the two shear stress sets.

Though the quality of the fits, as measured through the χ^2 and mean RE, may be comparable, the dynamics of the fits, shown in Figures 4.2 and 4.3 are quite different. The fit of the Levchenko model does not capture any of the old front plateau before the flow direction changes in the high and low shear stress conditions. The Meinhardt and Otsuji model fits are able to capture this, but are not as successful at capturing the cross over point between the old and new fronts. The heat map plots of Figure 4.3 reveal more differences. When fitting to the flow reversal, all three models have a front that breaks down with a new front forming, with differences on the timing and width of fronts. A similar behaviour is seen for the flow to no flow fit, with all the models starting with a front that breaks down over differing time scales. The fit to the no flow to flow data shows a different behaviour for each model. These differences are not apparent when comparing the χ^2 and mean RE values.

For the model fits, parameter values are shown in Section A, in the first columns of Tables A.1, A.2 and A.3. In the fit of the Meinhardt model, the diffusion parameters, D_a and D_c, take different values, with $D_a \approx 4D_c$. This is contrary to what would be needed for a system to have Turing instabilities. With the Otsuji model fit, the values of the diffusion parameters vary from 3.47×10^{-5} µm^{2}s^{-1} for D_u to 6.17×10^3 µm^{2}s^{-1} for D_v. In this fit the inactive form, v, diffusses 10^8 times faster than the active form, u. Compared to u, v will be much flatter over the cell cortex. Each model fit has 4 different values for the parameter dy, the asymmetry of the external signal, one for each data condition. With the Meinhardt model, all are of order 10^0, with the exception of $dy_{flow-noflow}$, which has the value 4.22×10^{-1}. For the Levchenko model, the fitted values range from 5.32×10^{-1}, for $dy_{noflow-flow}$, to 1×10^{-5} for $dy_{flow-noflow}$. The range of values from the fit of the Otsuji is smaller, ranging from 1.02×10^{-1} for dy_{low} to 2.76×10^{-2} for $dy_{flow-noflow}$. Both the Meinhardt and Otsuji model fits have a range of 10^1, compared to a range of 10^4 for the Levchenko fit. Depending on the condition being fitted, s, the external signal, is much different for the Levchenko model than the Meinhardt and Otsuji, where it is more comparable between conditions.

4.3 Truncation of Data

In the previous section I was able to fit the mathematical models to the *Dictyostelium* repolarisation data. However, the goodness of fit of the models to the data was poor in several cases. In order to improve the quality of these fits, refinement will be made to the selection of the data used for fitting.

In the data obtained by exposing cells to flow after a period of no-flow there is a peak of activation just before flow begins on the opposite side of the

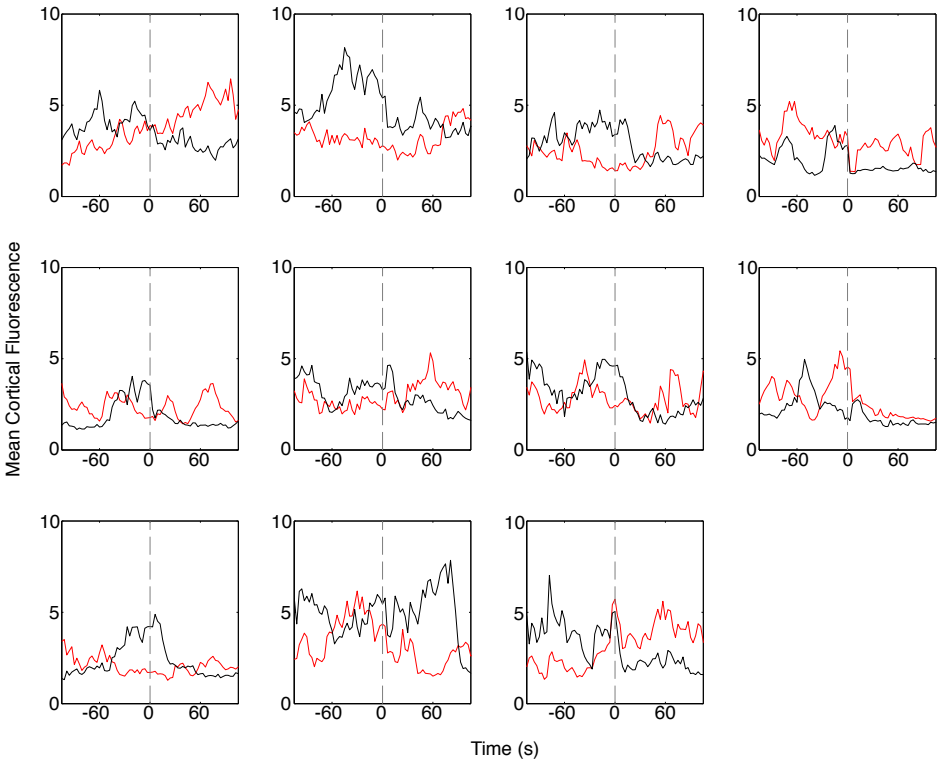

Fig. 4.4: **Individual cell data from *Dictyostelium* cells exposed to flow after a period without flow.** Each plot corresponds to data taken from an individual cell becoming exposed to flow at time $t = 0$ after a period without flow. Cells are split into two halves to obtain the mean cortical fluorescence of the front (red) and back (black) as in Figure 4.2. The cell front corresponds to the half of the cell facing into the flow once it starts.

cell to where flow is about to impinge. Activation there is not expected, and it affects the model fits, most prominently with the fit of the Levchenko model, Figure 4.3. By looking at the individual cells that were exposed to this condition it can see if this is the result of one outlier or the result of more common behaviour between them. Each cell was split into two halves and the mean cortical fluorescence of each calculated. The position of each half was dictated by the direction of flow once it begins, one half facing into the flow (front) and the other facing away from it (back). The same halves and naming were kept for when in the absence of flow and the results are shown in Figure 4.4. It can be seen that only one cell does not have a large amount of activation in the back before the flow begins. Removing the cells with the largest amount of activation does not remove the behaviour seen in the mean data. Given that the models are fitting to this and it may be the results of an experiemental anomaly it was decided to not continue using this data set during future fitting.

Models are currently fitted to data from a period both before and after flow change, and are able to capture the transition from one signal input to another. When fitting to the high and low shear stress conditions, the Levchenko model does not capture any of the old front behaviour before it starts to degrade after the change in flow direction, Figure 4.2. For the flow to no-flow condition, models would need to capture the dissipation of the existing front once the signal is removed. The fit for all three model's consists of a single front of activation that degrades over whole time course, as opposed to only degrading once the signal is removed, Figure 4.3.

Due to this, the data used for model fitting will be truncated such that fitting will only be to the data from after the flow change. These will be the same data as used previously minus all data for time $t < 0$. This will

result in fitting to smaller data sets than previously, totalling a reduction in the size of data for fitting of 49.0% to a combined total of 211 time points of data. For the three remaining conditions, the individual reductions were 8.6% for high shear stress, 13.3% for low shear stress and 34.9% for the flow to no-flow.

This reduction in the data used for fitting will affect the quality of the identifiability analysis. By having fewer data points to fit to, there are fewer constraints on the values of model parameters. Additionally, two parameters were no longer fitted, $dy_{flow-noflow}$ and $dy_{noflow-flow}$. $dy_{noflow-flow}$ was not fitted as the condition it is fitted on was no longer used, and $dy_{flow-noflow}$ was not fitted as the flow to no flow condition no longer used any data points when flow was present. As dy is only non-zero when flow is present, there were no data that could be used to fit it.

4.4 Fitting to Three Truncated Flow Conditions

The models were now fitted to the truncated repolarisation data. This is done in the same manner as with fitting to the full data sets. The models are still able to fit to the data, and an improvement in the quality of the fit is found, which is detailed below.

The χ^2 values and mean relative errors for the new fits are shown in table 4.3. Also shown is the percentage decrease from the corresponding value for the fit to the full data set shown in table 4.2. The Levchenko model has the best fit, with the lowest χ^2 value and mean relative error. The Meinhardt model fit is close to the Levchenko model fit, with the Otsuji model fit being the worst of the three. This contrasts with the previous fit where the Meinhardt model had the worst fit. In the Meinhardt model fit, the flow to no-flow condition contributes the most to the error on the fit, with the

		High Stress	Low Stress	Flow → No Flow	Total
Data	% decrease	8.6	13.3	34.9	49.0
Meinhardt	χ^2	32.4	62.5	83.4	178
	% decrease	88.2	87.9	68.8	86.9
	mean RE	1.93	2.04	2.43	2.18
	% decrease	50.6	45.9	20.0	35.9
Levchenko	χ^2	29.1	58.8	66.7	155
	% decrease	54.6	58.0	52.0	75.7
	mean RE	1.77	1.96	2.21	2.02
	% decrease	12.8	14.8	4.3	21.4
Otsuji	χ^2	90.6	162	109	361
	% decrease	16.9	22.9	32.3	48.1
	mean RE	3.06	3.22	2.69	2.93
	% decrease	1.0	2.4	-1.5	1.3

Tab. 4.3: χ^2 and relative error values for models fitting to truncated *Dictyostelium* repolarisation data. The χ^2 value is the chi-squared sum of squared errors difference between the model and the data. The mean RE value is the relative error of the model fit averaged over the number of image frames in the data set. % decrease details the percentage change for the value compared to that obtained when fitting the full data set, Table 4.2. The bottom row contains the percentage decrease in the amount of data used in the fitting for each individual data set, and total for all data.

two shear stress conditions having a small difference in the mean relative error. With the Levchenko model fit, the error is more spread out over the three conditions. The Otsuji model fit is different to the others in that the low shear stress fit is contributing the most to the error instead. The flow to no-flow condition has the lowest mean relative error, in contrast to the other two models where this condition has the largest error.

The Meinhardt model has the greatest improvement when fitted to the truncated data set, with a decrease in the mean relative error from 3.4 to 2.18, a reduction of 1.22, compared to a reduction of 0.55 and 0.04 for the Levchenko and Otsuji models respectively. The χ^2 value is reduced from 1354 to 178, a drop of 86.9%. This is much greater than the decrease in the amount of data used for fitting, 49%, implying that the model was less able to fit to the data that were removed than the data that remained after truncation. The Levchenko fit shows a similar trend, with a drop of 0.55 for the mean relative error and a drop of 75.5% in the χ^2 value. The Otsuji model is different in that there is a much smaller drop in the mean relative error, 0.04, and a drop of 48.1% in the χ^2 value. This is close to the amount of data removed from the fitting, which was 49%. This shows that reducing the amount of data that the model was fitted to has had a very minor effect on the quality of the fit of the Otsuji model.

Considering the individual conditions change in the χ^2 value, the greatest improvements can be seen in the two shear stresses with the Meinhardt and Levchenko models, both of which are greater that the amount of data removed. There is a smaller reduction in the χ^2 value for the flow to no-flow condition. This contrasts with the amount of data removed, which was greatest for the flow to no-flow condition. This shows that there has been a greater improvement in fit to the two shear stress conditions, which is

confirmed by the greater percentage decrease in the mean relative error for these two conditions.

With the fit of the Otsuji model, the amount of percentage decrease for the three conditons follows the same trend as with the amount of data removed. However, for the flow to no-flow condition, the χ^2 value decreases less than the amount of data removed, and the mean relative error increases. This implies that the Otsuji model is better able to fit to the flow to no-flow data that were removed than to what remains. It is the fitting to this data set that results in the total χ^2 for the Otsuji model fit decreasing by a smaller percentage than the amont of data removed.

The qualitative graph and heatmap comparisons of the model fits was repeated with the fits to the truncated data. As with the full data set the change in front and back behaviour in the fitted models was compared to that in the data. Cells are split into two halves as was done in Figure 4.2, the results of which are shown in Figure 4.5. With the Meinhardt model there is improvement in replicating the different front and back behaviours. For the two shear stresses it is able to capture to two different speeds at which the new front is formed, along with the breakdown of the previous front. It is also able to capture the plateau effect after the front has formed. The fit to the flow to no-flow data roughly follows the data, but does not reach the same value as seen in the data. These are an improvement over the previous fits, Figure 4.2, where it was unable to capture the different rates of front formation, or match the degradation curves well.

With the Levchenko fit, it does replicate to some extent the delay in front formation in the high shear stress condition. It also has a plateauing effect, along with degradation of the old front. For the flow to no-flow condition, it does roughly follow the trend in the data, with the front and back tending

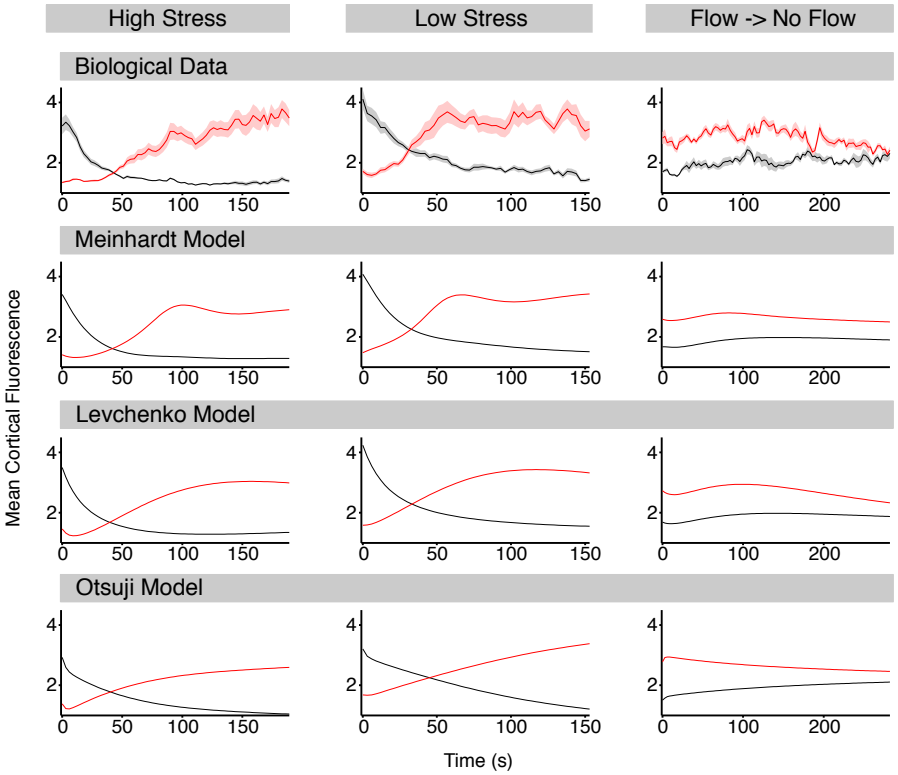

Fig. 4.5: **Comparison of the three mathematical models fitted to the truncated *Dictyostelium* repolarisation data.** Data and model fits were split into two halves based on the orientation of the external signal, as previously shown in Fig 4.2. The front half (red line) faces towards the external signal (for $t \leq 0$ in flow to no-flow, $t \geq 0$ in the other conditions), with the back half (black line) facing in the opposite direction. Each column corresponds to a different experimental condition, as signified by the column headers. The first row shows the repolarisation data, and the remaining three rows show the fits of the three mathematical models. The shaded area n repolarisation data indicates the standard error of the mean. The goodness of fit, χ^2, is 178, 155 and 361 for the Meinhardt, Levchenko and Otsuji models respectively.

to the mean value. These are of similar quality to the previous fit, Figure 4.2, with little difference between them.

The Otsuji model does not replicate the behaviour in the data as well as the other two models. For the flow to no-flow condition, the values for each side of the cell approach each other, but do not reach the same value. For the two shear stress conditions, it does not capture the dynamics well. It is not able to capture the delay in the start of the high shear stress front, though it does begin to plateau towards the end of the fit, albeit to a lower value than seen in the data. For the low shear stress, it does not capture the plateau effect in the formation of the new front, nor does the old front reach a point where it stop degrading. Comparing these fits to the fits to the non-truncated data they are of similar quality.

Additional comparisons can be made between the data and model fits using heatmaps. These are shown in Figure 4.6. With the Meinhardt model, for the two shear stress conditions, it can be seen that the new front forms at the same time as in the data, and it rapidly reaches its peak. Though it is not able to maintain this peak, as evidenced by the fading from the dark to a lighter orange, it maintains the width of the front. With the flow to no-flow condition it can see that it starts with a single peak of activation. This diffuses and decreases in strength with time. In comparison to the previous fitting, it is now able to begin the new front at the same time as one is formed in the data.

With the Levchenko model fit, the amount of activation in the front is lower than in the data for the low shear stress fit. Unlike in the Meinhardt model fit, once the front is formed, the level of activation remains stable with time. With the fit to the flow to no-flow data, it follows a similar pattern to the Meinhardt model fit. It begins with a front of activation that diffuses over

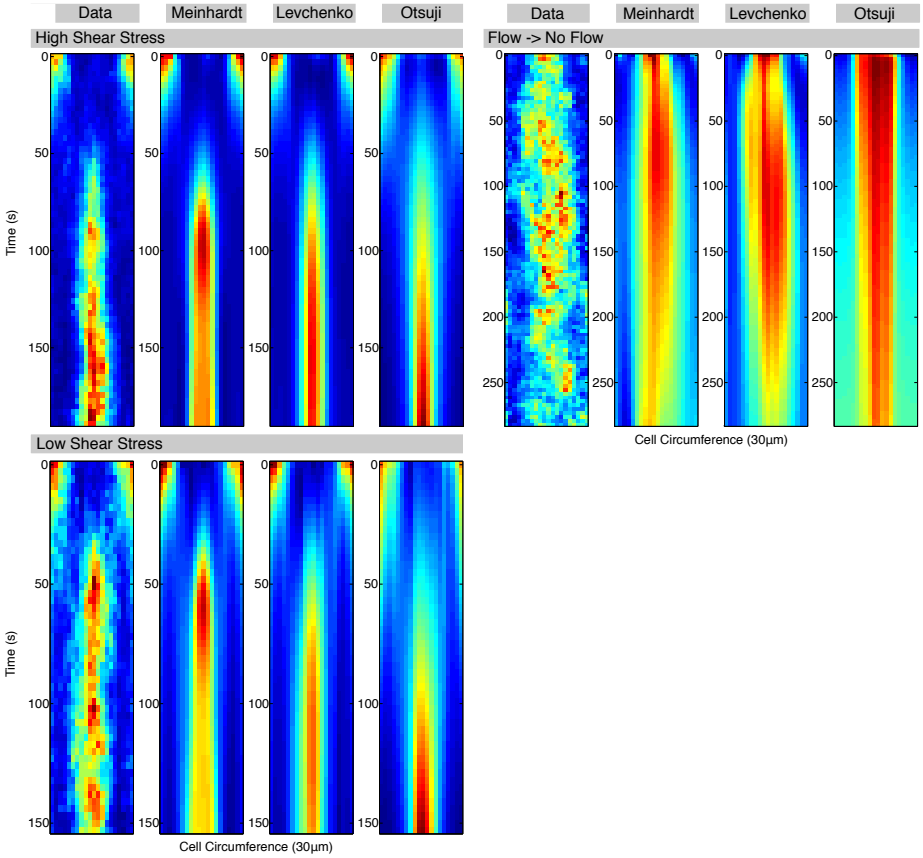

Fig. 4.6: **Heatmaps for truncated *Dictyostelium* repolarisation data and corresponding model fits.** Heat maps are created by taking the fluorescence values on the cell cortex and plotting these over time. Headers indicate the experimental conditions and whether the map is of data or which model it is from. Maps begin at the time $t = 0$, the point from where the data are truncated. For both shear stress conditions the position of the external signal is the middle of the plotted cell circumference. Maps are coloured using the MATLAB heat map Jet, which ranges from blue (low) to red (high).

the cell cortex and decreases over time. Comparing to the previous fit, the fit to the two shear stress data sets shows little difference. The fit to the flow to no-flow data shows a greater amount of activation over the conserved time points.

The Otsuji model begins front formation at the same time as the data, but takes the longest of the model fits to reach the same levels of activation that are seen in the shear stress data. With the fit to the flow to no-flow data, the model begins with a single large front of activation that with time decreases and diffuses over the cell cortex. This behaviour is similar to that shown in the previous fits, with the difference being the strength of the front at time $t = 0$.

When fitting to the truncated data sets, the parameter values obtained during fitting differ to those found when fitting to the full data sets. These parameters are shown alongside the parameters from the first fitting in Section A. With the Meinhardt model fit, the diffusion parameters, D_a and D_c remain of the same order of magnitude as before, but the values have changed so that now $D_c \approx 2D_a$. The parameters b_a, b_c, r_a, r_c and s_c are all order of magnitude 10^{-1}. The parameter r_b, has decreased from the value of $4.78 \times 10^{-1}\text{s}^{-1}$ to $1 \times 10^{-5}\text{s}^{-1}$. The two values for dy, have changed from an order of magnitude of 10^0 to one of 10^{-2}. dy_{low} is still marginally the larger parameter of the two.

With the Levchenko model fit there is a larger change in the parameter values. The greatest changes are with the dy parameters, dy_{low} and dy_{high}, which respectively change from 8.13×10^{-4} and 1.24×10^{-1} to 7.96×10^{-1} and 2.9×10^{-5}. With this change, the parameter values effectively swap.

For the Otsuji fit, D_u remains the same order of magnitude, but D_v shows a larger change, of 2.74×10^3 $\mu\text{m}^2\text{s}^{-1}$ to 47.3 $\mu\text{m}^2\text{s}^{-1}$. The Otsuji model was

first presented with $D_u = 0.01\mu m^2 s^{-1}$ and $D_v = 1\mu m^2 s^{-1}$. Though they differ from the values found in the fits, the fitted values follow the same pattern of $D_u < D_v$.The parameter a_1 remains the same order of magnitude, as does dy_{high}. dy_{low} changes from 1.02×10^{-1} to 7.62×10^{-2}. This is close to value of dy_{high}, which is 8.24×10^{-2}.

The diffusion constants from the model fits can be compared to that of the cAR1 cAMP receptor in *Dictyostelium*, a membrane bound g-protein. Its diffusion coefficient was measured to be $1.4^{-2}\mu m^2 s^{-1}$. This is close to the fitted value of the activator in the Meinhardt model, but is far from the diffusion coefficients observed in the fits of the Levcheno and Otsuji models. Truncating the data for fitting has allowed an improvement in the quality of the Meinhardt and Levchenko model fits, with little change to the quality of the Otsuji fit. The models now fitted to a reduced set of behaviours, no longer fitting to the no-flow to flow condition, nor are they fitted to data taken from both sides of the flow change. This is a weakness in that the fitted models may only be able to replicate the behaviour that they have been fitted to. Simulations are needed to test whether they are able to replicate the behaviour seen in the removed data. These, along with simulations investigating model behaviour outside outside of the time period where data are available, will be covered in the following chapter.

4.5 PLE Analysis

With the models fitted to the *Dictyostelium* repolarisation data, the identifiability of the model parameters was investigated using the Profile Likelihood Estimation (PLE) method, as detailed in Section 2.6. This uses a data based approach to give an indication as to the identifiability of the model parameters. To perform the PLE analysis parameters are varied over a range that

covers the fitted value. Each time the parameter is varied the model is refitted. The change in the χ^2 value is tracked as the parameter is varied. Identifiability estimates are based on when this crosses a threshold determined by the number of parameters in the model. A parameter is considered identifiable if when it is varied, the χ^2 values cross the threshold for when it is both increased and decreased from the fitted value.

The threshold used for determining parameter identifiability was calculated from the $\chi^2(\alpha, df)$ distribution, with α set to a confidence level of 68% and df the number of parameters. When plotting the χ^2 profile, two thresholds are shown. Where these and the χ^2 profile interesect determines the confidence interval for the parameter. The upper threshold is used to calculate the simultaneous confidence interval (df = number of model parameters), and the lower threshold is used to calcuate the pointwise confidence interval ($df = 1$). The simultaneous confidence interval threshold is used to determine whether or not a parameter is identifiable.

4.5.1 Meinhardt Model PLE

The PLE analysis was first performed on the Meinhardt model. There are eleven parameters, nine taken from the model and the two dys from the external signal. In the PLE analysis ten parameters were found to be identifiable, Figure 4.7. One, r_b, was found to be practically unidentifiable. The profile likelihood of the parameter s_a has a kink near the bottom of the curve. As the value of s_a changes, the refitted model gives a χ^2 value that does not follow the curve that the other fits follow. This and other such discontinuities are caused by local minima in the profile likelihood (Raue et al. 2009).

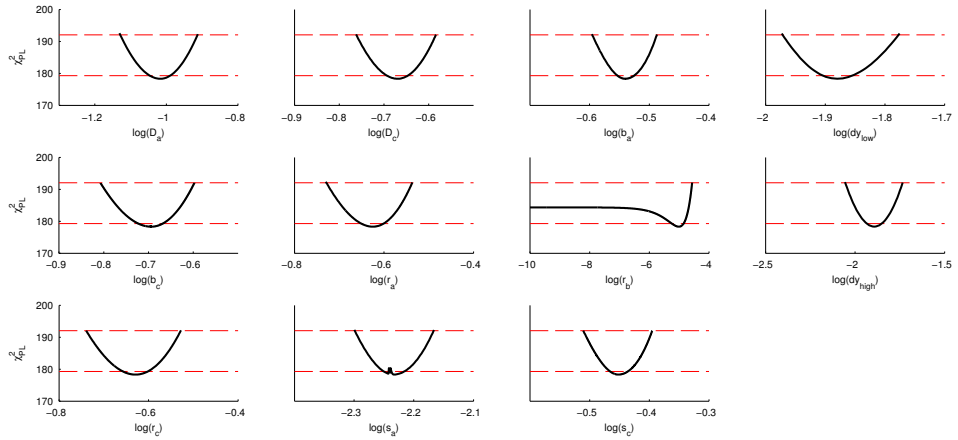

Fig. 4.7: **PLE analysis of the Meinhardt model.** For each parameter in the Meinhardt model the PLE (black line) is shown with the pointwise (lower red dashed horizontal line) and simultaneous (upper red dashed horizontal line) confidence interval thresholds. The intersection between the lines yields the boundaries of the confidence interval. Out of 11 parameters, 10 are identifiable with 1 (r_b) being practically unidentifiable.

4.5.2 Levchenko Model PLE

With the Levchenko model there are also nine model parameters and two *dy*s from the external signal. The results of the PLE analysis are that four parameters are identifiable, with the remaining seven unidentifiable, Figure 4.8. There are three structurally unidentifiable parameters, k_A, k_I and r_a and four practically unidentifiable parameters D_I, k_R, R_T and dy_{high}.

If a parameter is structurally unidentifiable, it may be unidentifiable due to the way the model is formulated. If this is the case, by changing part of the model it is possible to make the parameters identifiable. As each of these parameters is varied during PLE analysis, observations can be made as to how the other structurally unidentifiable parameters change, Figure 4.9 B. As one parameter changes, the other two vary to compensate so that the χ^2 value remains unchanged. This is caused by the model formulation, Equation 2.10, where there are the terms $k_a s(x)$ and $k_i s(x)$. The external

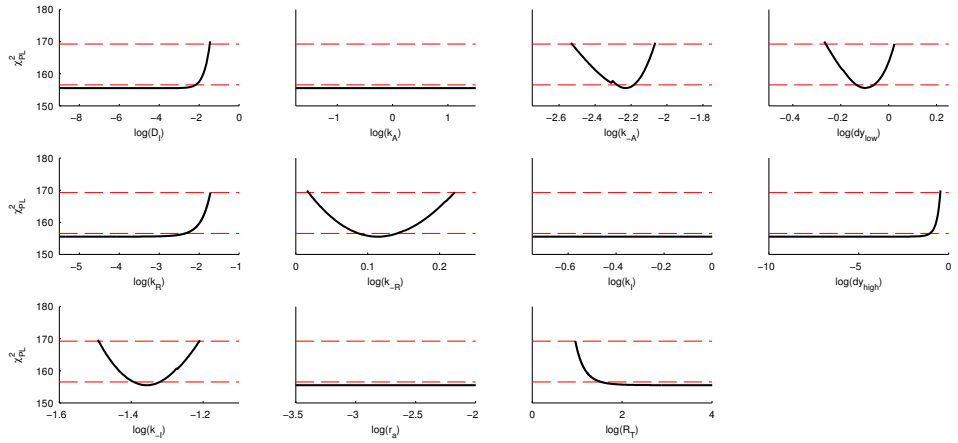

Fig. 4.8: **PLE analysis of the Levchenko model.** For each parameter in the Levchenko model the PLE (black line) is shown with the pointwise (lower red dashed horizontal line) and simultaneous (upper red dashed horizontal line) confidence interval thresholds. The intersection between the lines yields the boundaries of the confidence interval. Out of 11 parameters, 4 are identifiable, 4 practically unidentifiable and 3 structurally unidentifiable.

signal $s(x)$, Equation 2.8, includes the parameter r_a. When substituting in the equation for $s(x)$ into the Levchenko model it is seen that r_a is multipled with k_a and k_i. When r_a is varied, the other two parameters change so that the product remains the same. When either k_a or k_i are varied, r_a can change to keep the product the same, resulting in the third parameter needing to change as well. This is why these parameters are unidentifiable. To resolve this unidentifiability, the product of these parameters needs to be removed. This can be achieved by setting the value of r_a to 1 the external signal and replacing the values of the parameters k_a and k_i. The values used in the replacement are the product of the old parameter value with the value of r_a. With r_a fixed to the value 1, this results in the parameters k_a and k_i becoming identifiable, Figure 4.9 C.

The values of r_a, k_A and k_R have been altered in the model fit to the truncated data. To determine how the parameters have changed between the

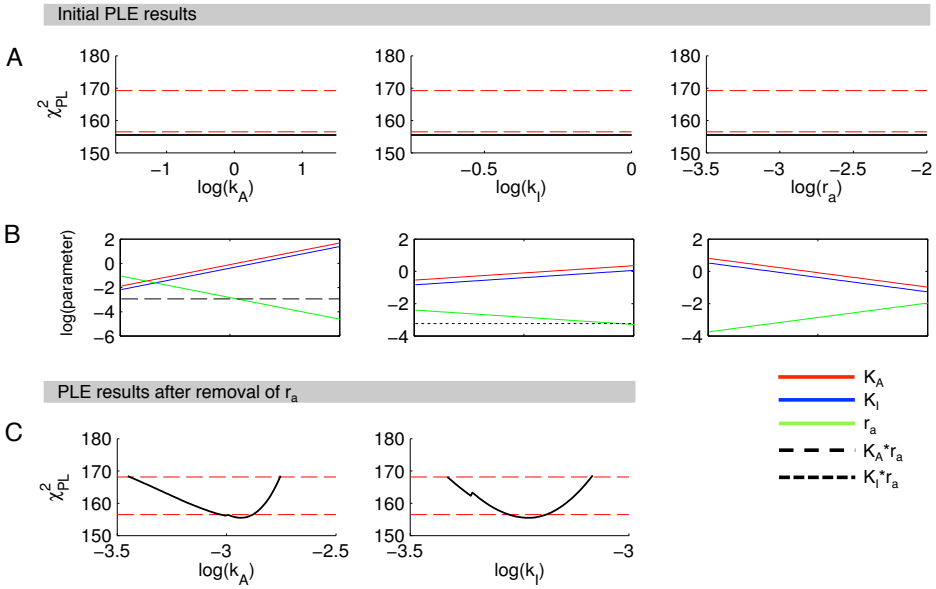

Fig. 4.9: **Resolving Levchenko structural unidentifiabilities.** (A) Using PLE analysis, 3 parameters from the Levchenko model (k_A, k_I and r_a) were found to be unidentifiable. As in Figure 4.8, PLE (black line) is shown with the two confidence interval thresholds (dashed red horizontal lines). (B) Comparison between the variation of the parameters k_A (red line), k_I (blue line), r_a (green line) and the products $k_A * r_a$ and $k_I * r_a$ over the course of the PLE analysis. Each plot details the variation corresponding to the PLE plot above it. (C) PLE analysis of the remaining parameters after the removal of r_a, with both parameters being identifiable.

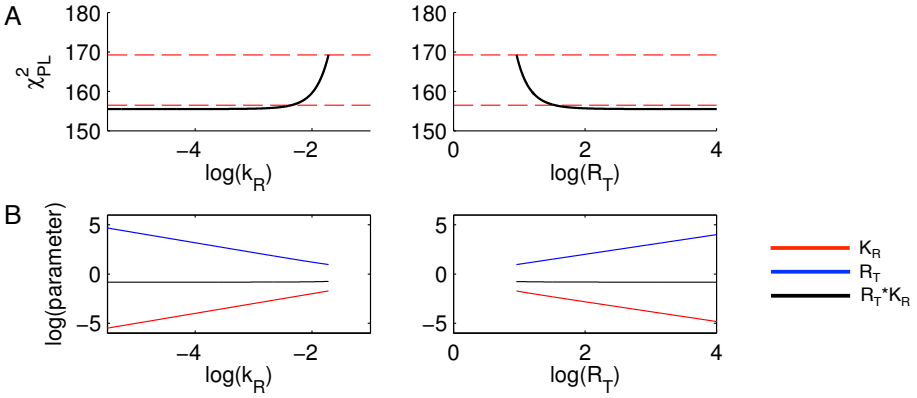

Fig. 4.10: **The relationship between parameters R_T and k_R during PLE analysis.**(A) Using PLE analysis on the Levchenko model, the parameters k_R and R_T were both found to be practically unidentifiable. As in Figure 4.8, PLE (black line) is shown with the two confidence interval thresholds (dashed red horizontal lines). (B) The variation of the k_R (red line), R_T (blue line) parameters and their product (black line) over the course of the PLE analysis. Each plot details the variation corresponding the PLE above it.

2 fits, comparisons are made between the new value for k_A and k_R and the product between r_a and the parameter values from the fit to the full data sets. The values for the products are $k_A r_a = 1.69 \times 10^{-3}\text{s}^{-1}$ and $k_I r_a = 2.03 \times 10^{-3}\text{s}^{-1}$. These compare to parameter values from fitting to the truncated data of $k_A = 1.16 \times 10^{-3}\text{s}^{-1}$ and $k_I = 5.9 \times 10^{-4}\text{s}^{-1}$. This shows that the value for k_A changes little, and the value of k_I decreases, by factors of 0.69 and 0.29 respectively.

There are three practically unidentifiable parameters in the Levchenko model fit. Two of these parameters, k_R and R_T, are linked to one another. When comparing parameter variation during PLE analysis, it was found that these parameters vary linearly with each other, Figure 4.10, with their product remaining constant. For most of the parameter variation the χ^2 value for the model fit remains unchanged. However, it does not do so for the entire parameter range, crossing the thresholds as k_R increases and R_T decreases.

In the model formulation, the parameters are related through the term $k_R A(R_T - R)$ as part of the term detailing the rate of change of R. There is no direct linear relationship between the two parameters. The unidentifiability is caused by the values of the parameters. The value for R_T is of the order 10^4, whereas the values taken by R are of the order 10^0. Using these parameter values $k_R A(R_T - R)$ can be approximated by $k_R A R_T$. In this approximation, both k_R and R_T are unidentifiable. When R_T is decreased, k_R increases the keep the product at the same value. However, eventually R_T decreases sufficiently that the approximation no longer holds and R can no longer be ignored. Here k_R is no longer able to change to compensate for the change in R_T and the χ^2 value for the model fit increases. When k_R is increased, R_T decreases to compensate, but eventually it decreases to a point where the χ^2 value increases as R no longer has a negligible affect. This gives each parameter a single limit, resulting in each being labelled as practically unidentifiable.

This relationship between the parameters explains the variation in the values of the parameters from the two fittings. The product of k_R and R_T can be calculated for each fitting, $6.87 \times 10^{-1}\text{s}^{-1}$ for the first fitting and 1.5×10^{-1} for fitting to the truncated data. These are the same order of magnitude, where as for the individual parameters, each varies by two orders of magnitude. There is a slight change from fitting to the different data sets, but most of the variation in the values for the parameters comes from the same relationship that results in them being unidentifiable.

4.5.3 Otsuji Model PLE

The Otsuji model has five model parameters and two *dy*s from the external signal. The results from the PLE analysis indicate that three are identifi-

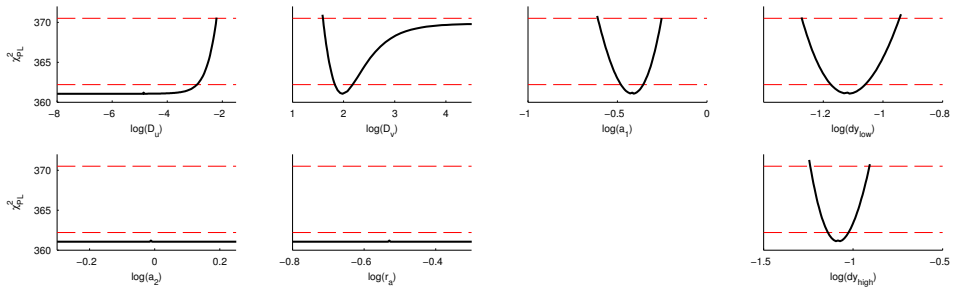

Fig. 4.11: **PLE analysis of the Otsuji model.** For each parameter in the Otsuji model the PLE (black line) is shown with the pointwise (lower red dashed horizontal line) and simultaneous (upper red dashed horizontal line) confidence interval thresholds. The intersection between the lines yields the boundaries of the confidence interval. Out of 7 parameters, 3 are identifiable, 2 practically unidentifiable and 2 structurally unidentifiable.

able, a_1, dy_{high} and dy_{low}, with four being unidentifiable, Figure 4.11. The two practically unidentifiable parameters are D_u and D_v, the diffusion parameters for the active and inactive form of the species in the model.

The two parameters that were found to be structurally unidentifiable were a_2 and r_a. By examining the changes in these two parameters as the other is varied during the PLE analysis, and considering the model formulation, it shows that the unidentifiability is caused by the product of a_2 and r_a in the same manner as for r_a and k_I and k_a in the Levchenko model. When r_a is set to the value 1, and the value of a_2 changed to the product of r_a and a_2, running the PLE analysis on it shows that it is now identifiable, Figure 4.12.

As the values of r_a and a_2 have been changed in the model fit to the truncated data, to determine how the parameters have changed comparisons were made between the new value for a_2 with the product of a_2 and r_a from the fit to the full data sets. From the values for first fit, $a_2 r_a = 2.77 \times 10^{-1}$. This is a similar to the value obtained for a_2 when fitting to the truncated data, which is 2.88×10^{-1}.

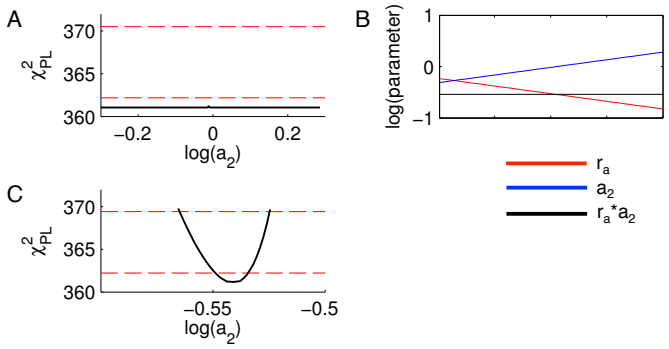

Fig. 4.12: **Resolving Otsuji structural unidentifiabilities.** (A) Using PLE analysis, the parameter a_2 is found to be unidentifiable. As in Figure 4.11, PLE (black line) is shown with the two confidence interval thresholds (dashed red horizontal lines). (B) Variation of the parameters a_2 (blue line), r_a (red line) and their product (black line) over the course of the PLE analysis. (C) PLE analysis of a_2 after the removal of r_a, a_2 now being identifiable.

Neither of the 2 diffusion coefficients are identifiable, but both have a bound. D_u has an upper bound of $1.38 \times 10^{-2}\mu m^2 s^{-1}$, and D_v has a lower bound of $17.1 \times 10^{-2}\mu m^2 s^{-1}$. This indicates that D_v should be always be larger than D_u, meaning that the inactive form of the species will always be diffusing faster than the active form. In the original formulation of the model, $D_u < D_v$, and these bounds show this to be the case here as well.

Three cell polarity models were fitted to mean cell data taken from *Dictyostelium* undergoing shear flow reversal induced repolarisation. After first fitting to all the shear flow data, the data used in fitting were reduced, which improved the quality of the fit. Identifiability analysis was conducted on the fitted models, using the PLE toolbox. Several parameters were found to be unidentifiable. After alterations were made to the models, several of these parameters were found to be identifiable, though not all were.

5. FURTHER MODEL INVESTIGATION AND CHANGES

In Chapter 4 I fitted three cell polarity models, Meinhardt (Meinhardt 1999), Levchenko (Levchenko & Iglesias 2002) and Otsuji (Otsuji et al. 2007), to *Dictyostelium* repolarisation data. For each of these models I obtained a fitted parameter set which I analysed using PLE analysis.

This chapter will focus on further analysis of the Meinhardt and Levchenko models, investigating the behaviour of the models past the point they were fitted. This behaviour, and the results of the PLE analysis, will be used to motivate changes to the models.

5.1 Simulations Past the Point of Fitting

To test the behaviour of the models past the point of fitting simulations were run using the initial conditions and parameters from the fit of the models, but continuing past the point where the data ended. The results of this for the Meinhardt and Levchenko models are shown in Figure 5.1.

For the Meinhardt model, after forming a new front it splits into two after roughly four minutes. This occurs one minute after the end of the part of the simulation that was fitted to data. With the Levchenko model simulation, after initially forming a new front opposite the new signal position, it shows a transient response with the new front dissipating.

This front splitting and transient response is not the desired long term behaviour from the fitted model. In the data to which they were fitted, once a

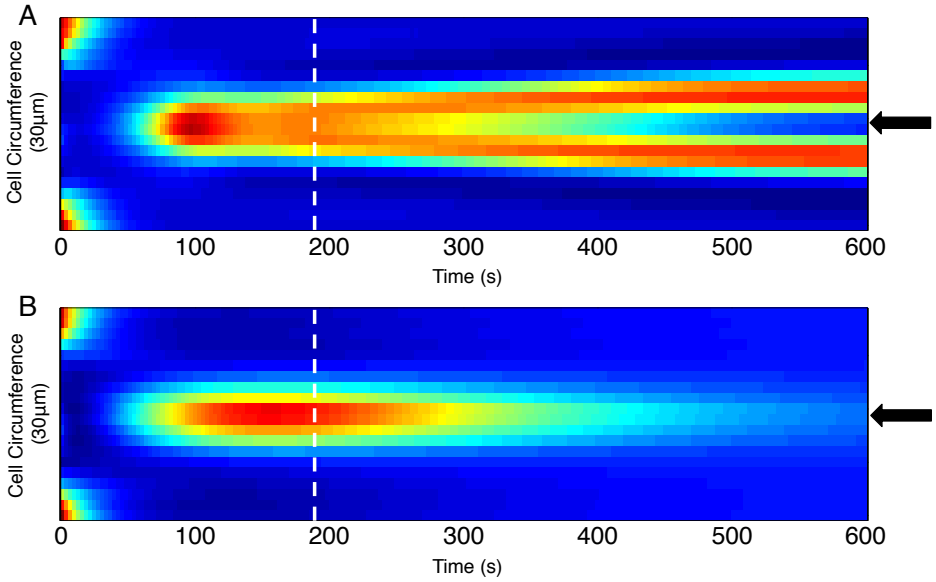

Fig. 5.1: **Long term behaviour of the fitted Meinhardt and Levchenko models.** Simulations were carried out using the fits of the Meinhardt model (A) and the Levchenko model (B) to the high shear stress data. Using the parameters and initial conditions obtained from the best fit (Section 4.4) the models were run for a time period of 10 minutes from the point of flow reversal, $t = 0$, maintaining the external signal throughout. The white dashed line indicates the length of the data used in fitting, which were 189s long. Maps are coloured using the MATLAB heat map Jet, which ranges from blue (low) to red (high).

new front has been formed it plateaus, maintaining the same value and not splitting. For the period where the model is fitted to data, this is what occurs. The models where further modified to attempt to keep this behaviour for the time period after that for which data exists.

5.2 Change in the External Signal

In Sections 4.5.2 and 4.5.3, it was shown how the parameter r_a in the external signal was causing several of the models parameters be unidentifiable for the Levchenko and Otsuji models. By fixing this parameter to the value 1, the PLE analysis was able to indicate that several previously unidentifiable parameters were now identifiable. The external signal in the Levchenko model will be replaced with the signal shown in Equation 5.1, where r_a has been fixed to the value 1.

$$s^*(x) = (1 + dy \times cos(2\pi(x - y)) \tag{5.1}$$

In the Meinhardt model, r_a was an identifiable parameter. To provide a consistent external signal between both models, in the Meinhardt model $s(x)$ will be substituted with $r_a s*(x)$.

5.3 Fixing b to a Constant in the Meinhardt Model

In the fit of the Meinhardt model, the inhibitor b did change much during the time period of the fit. The initial and end values are shown in Table 5.1. For all three conditions, the change in b was of the order 10^{-3}. The value for r_b, the rate of change of b, was $1 \times 10^{-5}\text{s}^{-1}$. This low value for the rate of change would explain why there is so little change in the parameter value

	High Stress	Low Stress	Flow → No Flow
b Initial Value	1.0088	1.0000	1.0048
b End Value	1.0106	1.0022	1.0084
Increase	1.81×10^{-3}	2.22×10^{-3}	3.55×10^{-3}

Tab. 5.1: Initial and end values for inhibitor b in the fitted Meinhardt model. Values are taken from the model fits shown in Section 4.4, with the end value being the value at the end of the fitting time frame.

over the fit.

As b varies very little, this motivated setting $\frac{\partial b}{\partial t} = 0$, thus turning b into a constant b^*. As the initial value for b in the original model is close to 1 for all conditions, $b*$ was set to the value of 1. Including the change in the external signal this results in the following modified Meinhardt model.

$$\begin{aligned} \frac{\partial a}{\partial t}(x,t) &= \frac{s^*(x) r_a (a^2 + b_a)}{(s_c + c)(1 + s_a a^2)} - r_a a + D_a \frac{\partial^2 a}{\partial x^2}(x,t) \\ \frac{\partial c}{\partial t}(x,t) &= b_c a - r_c c + D_c \frac{\partial^2 c}{\partial x^2}(x,t) \end{aligned} \tag{5.2}$$

where a is the activator and c is the inhibitor as described in Section 2.7.2. This is now a two-variable system and now only has parameters that were found to be identifiable when fitted in the full model.

The role of the global inhibitor b was to stop the formation of multiple fronts of activation. By changing it to a constant value, it may be insufficient to prevent the formation of other fronts of activation.

5.3.1 Fitting Results

The modified Meinhardt model was fitted to the same *Dictyostelium* repolarisation data set as used for model fitting in Section 4.4. The χ^2 value for the fit is shown in Table 5.2. The modified model is able to fit to the data almost as well as the original model (change of χ^2 from 178 to 180). There is

	High Stress	Low Stress	Flow → No Flow	Total
χ^2	36.6	68.1	75.6	180
mean RE	1.92	2.08	2.32	2.14

Tab. 5.2: χ^2 and relative error values for the modified Meinhardt model, Equation 5.2, fitting to *Dictyostelium* repolarisation data. χ^2 is the sum of squared errors difference between the model and the data, Equation 2.6. Mean RE is the relative error of the model fit averaged over the number of image frames in the data set.

more variation in the fits to the individual data sets, with the repolarisation fits worsening whilst the flow to no-flow fit improves (χ^2 increase of 4.2 and 7.6 for the high and low shear stress respectively, and a decrease of 7.8 for flow to no-flow).

The front/back behaviour has worsened compared to that of the original model fit, Figure 5.2 A. When comparing the break-down of the old front for the repolarisation conditions, the modified model matches well. It also captures the initial building of the new front, and the point where the front and back fluorescence levels are equal.

For the high shear stress condition, the model matches the increase as the new front is created. For the low shear stress condition, it does not match the building to the plateau, nor does it capture the plateau effect either. After reaching a maximum at 102 seconds, it proceeds to decrease, not plateauing as the data do. With the flow to no-flow data the model is able to match the data well.

When comparing the heat maps of the model fit to the data, the differences in beavhour can be observed. The decrease in the front of the low shear stress fit can be seen, along with the slower build up of activator at the beginning of the front.

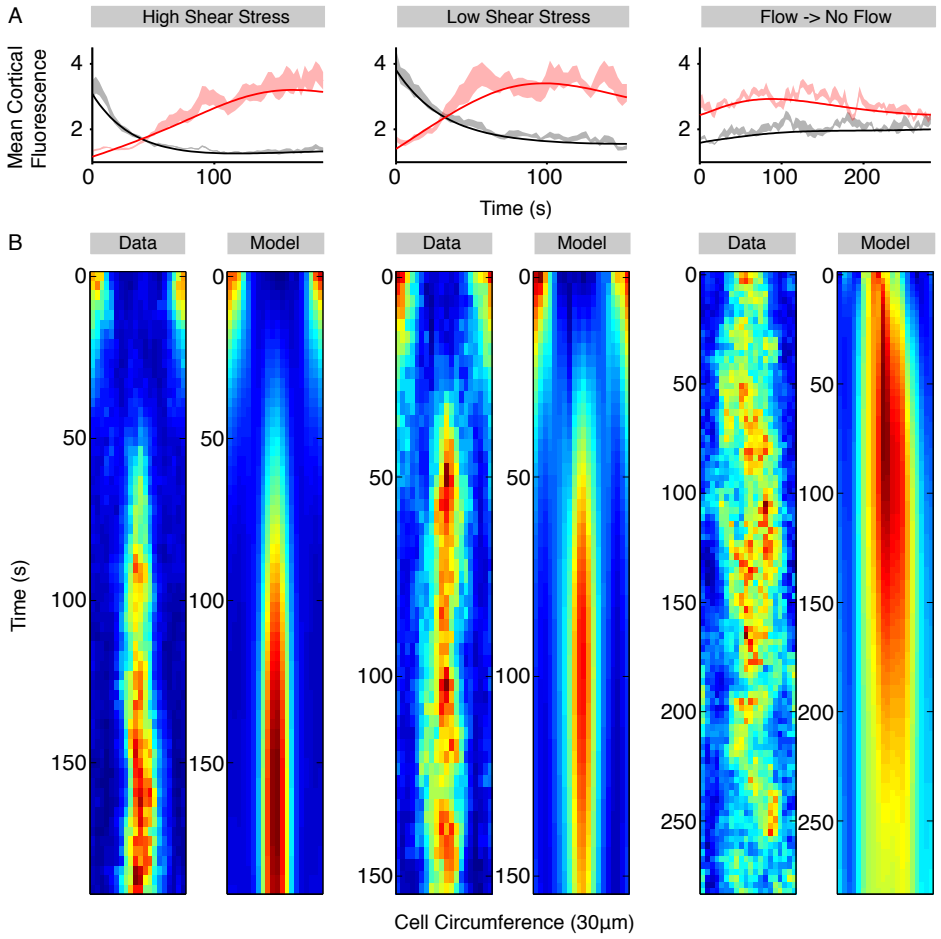

Fig. 5.2: **Fit of the modified Meinhardt model with $b = 1$.** Model fit to *Dictyostelium* repolarisation data are shown through front/back comparison (A) and through heat maps (B). Each column shows the fitting to a separate condition as signified by the header. The model used for fitting is shown in Equation 5.2, with parameters conserved between data sets, with the exception of dy. (A) As in Figure 4.2 the data and model are split into two halves, and the mean for each half plotted. The front half (black line) faces towards the external signal (for $t \leq 0$ for flow to no-flow, $t \geq 0$ otherwise) with the back half (red line) facing in the other direction. The solid line shows the mean for the fitted model, shaded area shows the standard error of the mean for the data. (B) Heat maps show either the data or model fit as indicated by the headers and coloured using the MATLAB heat map Jet.

5.4 Further Modification of the Meinhardt Model

An alternative to setting $b = 1$ is to set it to a constant that can vary over the different conditions. As b varied slightly over the 3 different data conditions in the earlier fitting, Table 5.1 it motivated the use of a function that would be able to achieve a similar variation. It was chosen to set $b = 1 + \beta_0(P^2 - P\beta_1)$, where P is the shear stress of the laminar flow and β_0 and β_1 are new global constants. This dependence on the strength of the shear flow is influenced by the response to differing strengths of flow where a higher strength flow inhibits the formation of the front during repolarisation (Dalous et al. 2008).

Accounting for the change in the external signal, this results in the following modified Meinhardt model.

$$\begin{aligned} \frac{\partial a}{\partial t}(x,t) &= \frac{s^*(x) r_a (\frac{a^2}{1+\beta_0(P^2-P\beta_1)} + b_a)}{(s_c + c)(1 + s_a a^2)} - r_a a + D_a \frac{\partial^2 a}{\partial x^2}(x,t) \\ \frac{\partial c}{\partial t}(x,t) &= b_c a - r_c c + D_c \frac{\partial^2 c}{\partial x^2}(x,t) \end{aligned} \tag{5.3}$$

The model was initially fitted with dy as a local parameter. After the initial fitting, it was found that dy_{high} and dy_{low} had almost identical values. As such dy was set a global parameter that was non-zero whenever there was flow, and zero when there was no flow. After refitting with the global dy, the parameters remained unchanged from when dy was a local parameter.

5.4.1 Fitting Results

The newly modified Meinhardt model was fitted to the same *Dictyostelium* repolarisation data set as used for model fitting in Section 4.4. The χ^2 value for the fit is shown in Table 5.3. The modified model is able to fit to the data almost as well as the original model (change of χ^2 from 178 to 184),

	High Stress	Low Stress	Flow → No Flow	Total
χ^2	32.7	63.2	88.1	184
mean RE	1.94	2.04	2.48	2.21

Tab. 5.3: χ^2 and relative error values for the modified Meinhardt model, Equation 5.3, fitting to *Dictyostelium* repolarisation data. χ^2 is the sum of squared errors difference between the model and the data, Equation 2.6. Mean RE is the relative error of the model fit averaged over the number of image frames in the data set.

though not as well as for the previous modification. The majority of this increase comes from the fit to the flow to no-flow data which has an increase of 4.7, compared to the high and low shear stress which increased by 0.3 and 0.7 respectively.

The front/back behaviour of the model fit is an improvement on the fit of the previous modified model, Figure 5.3 A. It is able to match the degradation of the old front during repolarisation, and the formation of both of the new fronts. It is also able to plateau once the front has been formed, though with a slight curve. With the fit to the flow to no-flow condition, the model is not able to match the data well with the levels of activator in the old front remaining stable throughout. In the other half of the cell, activator levels do increase in line with what was observed in the data.

When comparing the heat maps of the model fit, Figure 5.3 B, the front formation occurring at the same time as that in the data can be observed. The decrease in the intensity after the initial front formation can also be observed. In the front/back plots there is an increase in the concentration in the front of the cell at the end of the data. When consulting this time in the heat maps, there is no increase in concentration, just a slight spreading of the front. The front remains on one half of the cell, so this spreading is noted as an increase in the mean fluorescence in the front of the cell.

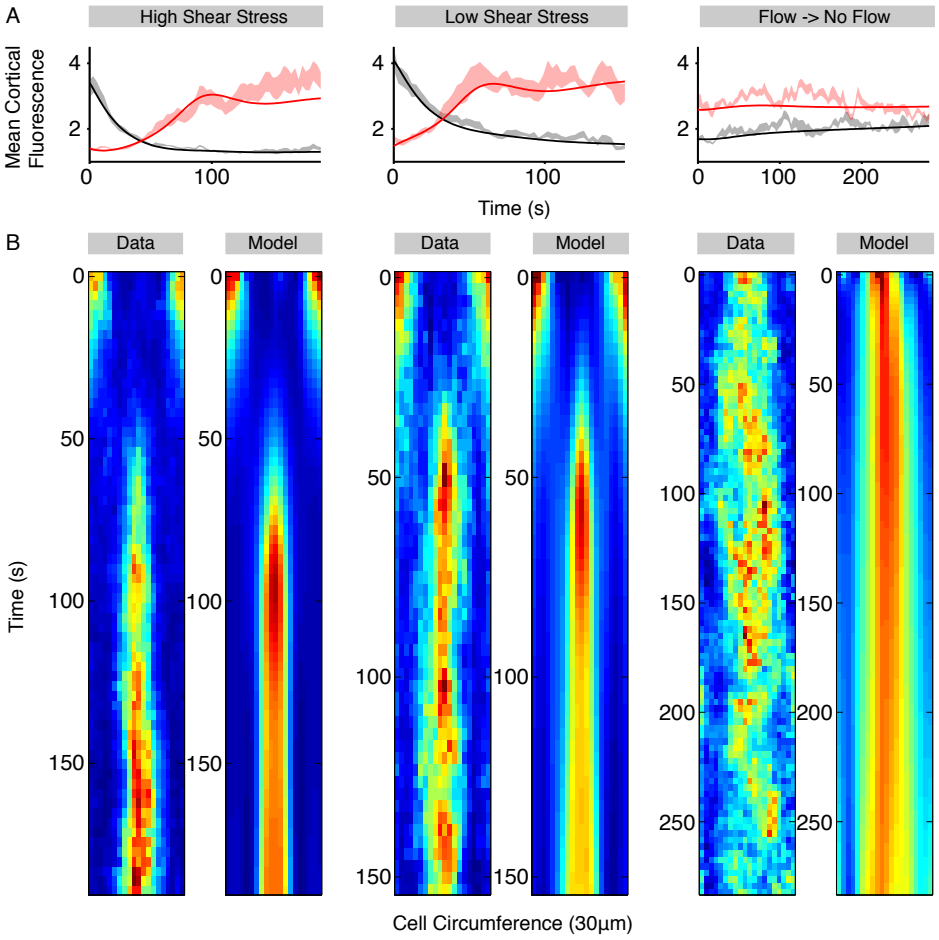

Fig. 5.3: **Fit of the modified Meinhardt model with $b = 1 + \beta_0(P^2 - P\beta_1)$.** Model fit to *Dictyostelium* repolarisation data is shown through front/back comparison (A) and through heat maps (B). Each column shows the fitting to a separate condition as signified by the header. Model used for fitting is shown in Equation 5.3, with parameters conserved between data sets, with the values of P being specified for each fit. (A) As in Figure 4.2 the data and model are split into two halves, and the mean for each half plotted. The front half (black line) faces towards the external signal (for $t \leq 0$ for flow to no-flow, $t \geq 0$ otherwise) with the back half (red line) facing in the other direction. The solid line shows the mean for the fitted model, the shaded area shows the standard error of the mean for the data. (B) Heat maps show either the data or model fit as indicated by the headers and coloured using the MATLAB heat map Jet.

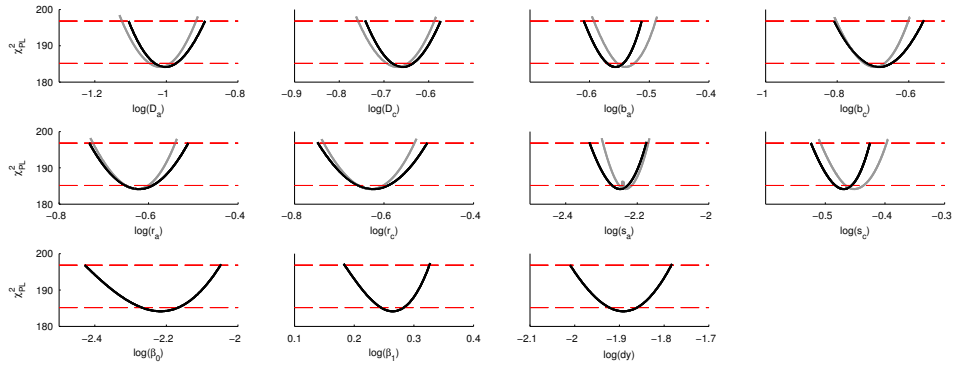

Fig. 5.4: **PLE analysis of the modified Meinhardt model.** For each parameter in the modified Meinhardt model with $b = 1 + \beta_0(P^2 - P\beta_1)$, the PLE (black line) is shown with the pointwise (lower red dashed horizontal line) and simultaneous (upper red dashed horizontal line) confidence interval thresholds. The intersection between the lines yields the boundaries of the confidence interval. Out of 11 parameters, 11 were found to be identifiable. Grey lines show the PLE of parameters conserved with the Meinhardt model analysed in Section 4.5.1, with the addition of $\Delta\chi^2 = 5.833$ to facilitate a direct comparison.

5.4.2 Identifiability Analysis

Having fitted the modified Meinhardt model with $b = 1 + \beta_0(P^2 - P\beta_1)$, I proceeded to perform the PLE analysis on it to determine the identifiability of the fitted parameters. There were eleven parameters in the model, eight of which were conserved with the formulation fitted in Chapter 4. The parameter r_b was no longer in the model, and the differing dy that had taken different local values were replaced with a single global parameter. Two new parameters have been added, β_0 and β_1. The results of the PLE analysis are shown if Figure 5.4.

Out of the eleven model parameters, all were found to be identifiable. For the eight parameters that were conserved with the model formulation used in the earlier analysis, all had similar confidence intervals in the two fits. No parameter value for either fit fell outside of the confidence interval obtained from the PLE analysis on the other fit.

5.5 Linear Stability Analysis of the Two-Variable Meinhardt Model

For the modified Meinhardt model I used linear stability analysis to investigate the stability of the fitted model. I followed the methodology described by Cross & Greenside (2009, chapter 3), using work developed by Turing (1952) and Segel & Jackson (1972). This assumes that the system that is stable in the absence of diffusion, and conditions can be found that cause it to be unstable in the presence of diffusion. This behaviour is a Turing instability.

To begin this analysis the models are formulated using the following terminology,

$$\begin{aligned} \frac{\partial a}{\partial t}(x,t) &= f_1(a,c) + D_a \frac{\partial^2 a}{\partial x^2}(x,t) \\ \frac{\partial c}{\partial t}(x,t) &= f_2(a,c) + D_c \frac{\partial^2 c}{\partial x^2}(x,t) \end{aligned} \tag{5.4}$$

where

$$f_1(a,c) = \frac{s^*(x) r_a (\frac{a^2}{1+\beta_0(P^2-P\beta_1)} + b_a)}{(s_c + c)(1 + s_a a^2)} - r_a a \tag{5.5}$$

and

$$f_2(a,c) = b_c a - r_c c \tag{5.6}$$

The steady state in the absence of diffusion ($D_a = D_c = 0$) is denoted as $\mathbf{u}_b = (a_b, c_b)$ and the matrix $\mathbf{A}$ as the 2×2 jacobian matrix evaluated at the steady state,

$$a_{ij} = \left. \frac{\partial f_i}{\partial u_j} \right|_{\mathbf{u}_b} \tag{5.7}$$

Linearising about the steady state gives the following conditions for the stability of the system with diffusion,

$$trace(\mathbf{A}) = a_{11} + a_{22} - (D_a + D_c)q^2 < 0 \tag{5.8}$$

$$det(\mathbf{A}) = (a_{11} - D_a q^2)(a_{22} - D_c q^2) - a_{12}a_{21} > 0 \tag{5.9}$$

where q is the wave number. For this to be stable in the absence of diffusion, then the following two conditions must be met;

$$a_{11} + a_{22} < 0 \tag{5.10}$$

$$a_{11}a_{22} - a_{12}a_{21} > 0 \tag{5.11}$$

As D_a, D_c and q^2 are always positive, this implies that Equation 5.8 always holds. The only way for diffusion to destabilise the system is for Equation 5.9 to be reversed. This leads to the following condition for instability with diffusion,

$$D_a a_{22} + D_c a_{11} > 2\sqrt{D_a D_c (a_{11}a_{22} - a_{21}a_{12})} \tag{5.12}$$

Using the parameters from the fit of the modified Meinhardt model in the previous section determines for the parameter values where the model will exhibit a Turing instability. I focused in particular on the values of the diffusion parameters D_a and D_c.

The values of the parameters change depending on whether or not there is an external signal present. When there is no external signal, $P = dy = 0$

and $s^*(x) = 1$ for all x. This results in

$$\mathbf{A} = \begin{pmatrix} 0.202 & -0.235 \\ 0.208 & -0.238 \end{pmatrix} \tag{5.13}$$

which satisfies the conditions for stability in the absence of diffusion, Equations 5.8 and 5.9. When diffusions of a and c were added

$$D_a a_{22} + D_c a_{11} = 2.08 \times 10^{-2} \tag{5.14}$$

$$2\sqrt{D_a D_c (a_{11}a_{22} - a_{21}a_{12})} = 8.39 \times 10^{-3} \tag{5.15}$$

which satisfies the condition for diffusion to make the steady state unstable, Equation 5.12. To find a system where the addition of diffusion did not cause instability it was decided to alter the rate of diffusion of the inhibitor, c. A limit on what parameter value could be chosen was given by when Equation 5.12 does not hold,

$$D_a a_{22} + D_c a_{11} \leq 2\sqrt{D_a D_c (a_{11}a_{22} - a_{21}a_{12})} \tag{5.16}$$

Suitable values for D_c were bounded by solutions to

$$D_c^2 a_{11}^2 + D_c(2D_a a_{11}a_{22} - 4D_a(a_{11}a_{22} - a_{21}a_{12}) + D_a^2 a_{22}^2 = 0 \tag{5.17}$$

Only the upper bound matters, as that corresponds to the solution for real eigenvalues. For the case with no signal, this were 1.52×10^{-1} $\mu m^2 s^{-1}$. When there is an external signal present, choosing $P = 1$, and s between 0.9872 and 1.0128. As the above analysis assumes s is a constant, I calculated the bounds on D_c with s being fixed at a value in between this maximum and minimum, see Table 5.4.

Value of s	Upper Bound of D_c
1.0128	2.25×10^{-1} µm^{2}s^{-1}
1.0064	2.02×10^{-1} µm^{2}s^{-1}
1	1.76×10^{-1} µm^{2}s^{-1}
0.9936	1.49×10^{-1} µm^{2}s^{-1}
0.9872	2.07×10^{-1} µm^{2}s^{-1}

Tab. 5.4: Bounds of the diffusion parameter D_c. The interval they describe is where Equation 5.12 does not hold.

The upper bound for D_c from the case with no signal was lower that the upper bound for all values of s, except for $s = 0.9936$, I therefore decided to change the value of D_c to 1.43×10^{-1}, 65% of the value obtained from the fit.

This choice was validated when comparing simulations of the fitted model, with both the original and modified value for D_c, Figure 5.5 A and B respectively. When using the parameters from the model fit, when the cell is exposed to an external signal after coming to equilibrium with no signal, a front is formed opposite the signal. This splits into three distinct fronts within ten minutes. When the external signal is removed there is a decrease in intensity in the central front, with all three fronts continuing.

In contrast, in the simulation with the modified diffusion, when the external signal begins, a front is formed opposite it. This remains for the entirety of the signal duration. Once the signal is removed then the front dies down and there is no more response from the cell.

5.6 Long Term Simulations with the Modified Meinhardt Model

With the modified Meinhardt model fitted to the mean repolarisation data, it would desirable to test the model outside of the time frame and experimental conditions to which it had been fitted. As I had been unable to

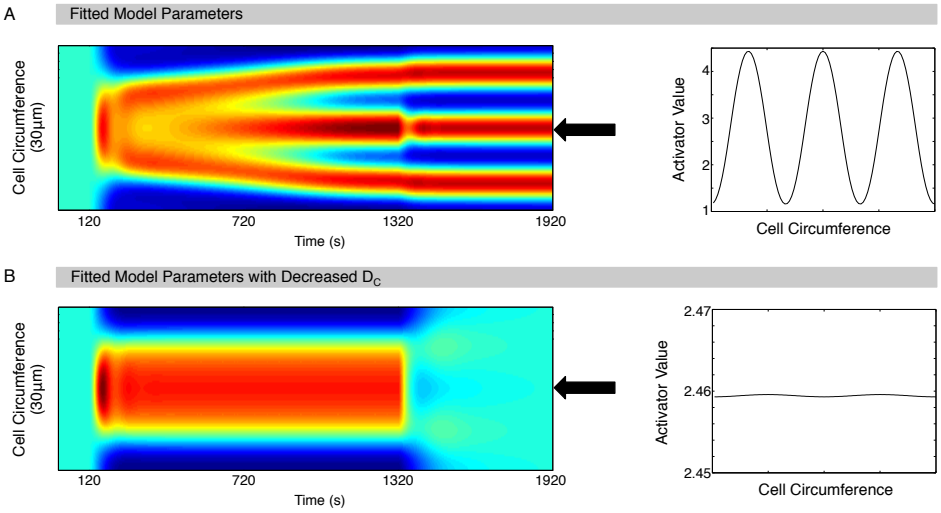

Fig. 5.5: **Long term behaviour of the fitted modified Meinhardt model.** Using the parameters from the fit of the modified Meinhardt model, simulations are used to determine the long term behaviour of the fitted model (A), and again with a modification in the parameter set (B). Simulations are carried out on a cell of 100 nodes with the distance between the node $\Delta x = 0.2$. Starting from uniform initial conditions, models are run for a period without an external signal to reach equilibrium before the signal scheme begins. The activator values around the cell circumference at the end of the simulation are plotted to the right of the heat map. (A) After a period of 2 minutes without a signal, a signal is started opposite node 50 (black arrow) and remains for a period of 30 minutes. (B) The inhibitor diffusion parameter D_c is reduced by 35%. After a period of 2 minutes without a signal, a signal is started opposite node 50 (black arrow) and remains for a period of 20 minutes, before being removed for a period of 10 minutes.

generate new data from the flow chamber experiments with which to compare, I conducted simulations using a range of generalised input signals. These were motivated by other experiments on *Dictyostelium* polarisation, including chemotactic responses. As the flow chamber repolarisation resembled the dynamics of a chemotactic repolarisation, the fitted model may be suitable to represent other chemotactic polarisation responses. These simulations were conducted with the Meinhardt model using the modification to the parameter D_c as described above. These were to investigate its behaviour under a range of conditions. The number of nodes on the cell surface was increased by a factor of 5 to 100, with the model simulated for a period without signal in order for it to reach equilibrium before a signal scheme was applied. All signal schemes consisted of two minutes without an external signal, followed by a change in the external signal. The signal changes were set to occur every 10 minutes, in order to give the model time to fully adjust to the change in the signal.

To calculate plateau timing I measured the value that the plateau reached, and then calculated how long it took for the model to get within 1% of it from the point of signal change. Initial peaks before descending to the plateau value were ignored for this purposes of getting within 1% of the plateau value. The first signal scheme consisted of a signal that moved to the other side of the cell, and then returned before being removed, Figure 5.6 A. This was akin to the shear flow reversal experiments with *Dictyostelium* (Dalous et al. 2008) that the models were fitted to. The model was able to respond to the change in shear flow and repolarise to face into the new direction of flow. When a new front forms, there is an initial peak of activation before it settles into the continuous response. The mean activator level in each half of the cell was calculated, Figure 5.6 B. When the signal

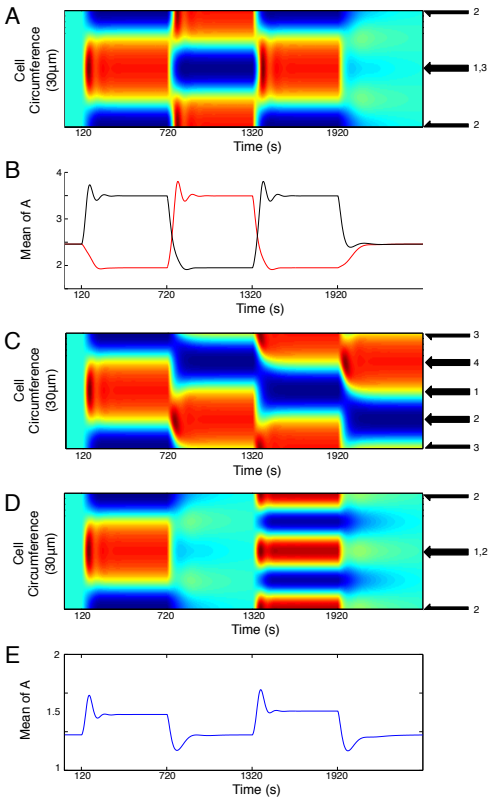

Fig. 5.6: **Response of the modified Meinhardt model to a changing external signal.** Using the parameters from the fit of the modified Meinhardt model with the modified value for D_c, simulations are used to determine the behaviour of the fitted model to varying external stimuli. Simulations are carried out on a cell of 100 nodes with the distance between the nodes of $\Delta x = 0.2$. Starting from uniform initial conditions, models are run for a period without an external signal to reach equilibrium before the signal scheme begins. Each scheme begins with a period of 2 minutes without signal, and each signal is simulated at a strength of 1Pa. (A) A signal is started opposite node 50 (black arrow 1) for a period of 10 minutes. It is then moved to opposite node 100 (black arrow 2) for a period of 10 minutes. The signal is returned to its original position (black arrow 3) for a period of 10 minutes before being removed. (B) The mean value for the activator a in the two halves of the cell. The cell is split into two halves, nodes 25-74 opposite signals 1 and 3 (black line) and nodes 75-24 opposite signal 2 (red line). (C) A signal is started opposite node 50 (black arrow 1). Every 10 minutes in the simulation, the signal is moved 25 nodes around the cell circumference (black arrows, 2, 3, 4). (D) A signal is begun opposite node 50 for a period of 10 minutes (black arrow 1) before being removed for a period of 10 minutes. A second signal begins where the frequency of the external signal has been doubled to create a signal with two peaks, opposite nodes 50 and 100 (black arrows 2). This remains for a period of 10 minutes before being removed for 10 minutes. (E) The mean value for the activator a in simulation C.

is present, the mean of the side of the cell opposite it plateaus at a value of 3.59, reaching it 2.5 minutes after the signal is changed. The back of the cell degrades to a value of 1.68, which takes it 3 minutes.

In comparison, when *Dictyostelium* cells repolarise under a shear flow of $0.9PA$, a new front is formed after 60 seconds, with the old front breaking down after 70 seconds (Dalous et al. 2008). The mean values for each half of the cell are close, with a front mean fluorescence of 3.75 and mean of the back 1.75.

The second signal scheme consisted of a signal moving 90° around the cell every 10 minutes, Figure 5.6 C. As the signal moves around the cell cortex, the front of activation follows it. There is still the peak of activation at the beginning of the front, before it settles into the steady front.

The third signal scheme consists of a signal that starts opposite one side of the cell, before being removed and is then replaced with a signal against two sides of the cell at once, Figure 5.6 D. This new signal is achieved by doubling the frequency of the external signal. It is akin to experiments where two sources of chemoattractant are placed either side of a cell (Janetopoulos et al. 2004). This doubled signal results in a doubling of the fronts, one facing into each signal peak. Increasing the frequency of the external signal causes a corresponding increase in the number of fronts formed.

The mean value for the activator during this signal scheme is shown in Figure 5.6 E. When there is no external signal present, the activator mean is 2.46. When the external signal begins after 2 minutes, the mean tends to a value of 2.72. When the signal frequency is doubled, the mean increases to 2.76. The increase in the mean continues as the frequency is increased (2.93 and 3.04 for 3 and 4 fronts respectively).

In section 3.1, I showed the response of developed *Dictyostelium* to a pulse

of cAMP. This pulse caused a localisation of actin to the cortex, followed by a similar, but smaller, response from myosin. The modified Meinhardt model was tested to a short lived pulse of signal. To simulate the pulse, I used a slight modification of the input signal, s. As the pulse would be equal over the entire cell boundary, the cosine term was removed to give the following external signal

$$s(x) = (1 + dy) \tag{5.18}$$

This signal was in place for a period of 10 seconds, before being removed. The value for dy used was the value obtained when fitting the *Dictyostelium* repolarisation data. The value of $P = 0$, as there is no flow. Simulations run with varying values of P returned the same behaviour as seen with $P = 0$. The result of the simulation is shown in Figure 5.7. As soon as the signal begins, there is an increase in the concentration of the activator over the entire cell. This concentration increases till it reaches a maximum of 2.73 at $t = 153$s, 33s after the signal started. The concentration then decreases to a minimum of 2.42 at $t = 264$s, 144s after the signal began, before returning the equilibrium value.

This response is slower than the cAMP response seen in *Dictyostelium*, which reaches the maximum of its actin response 5-8s after cAMP is added. The increase in the spike of activation in the model simulation is also lower than that in the cAMP response, an increase of 11% compared that of 30%. These show that the model does provide a good replication of the cAMP pulse response.

The value of P in the formulation of the modified Meinhardt model corresponds to the strength of the shear flow, simulations were used to ascertain

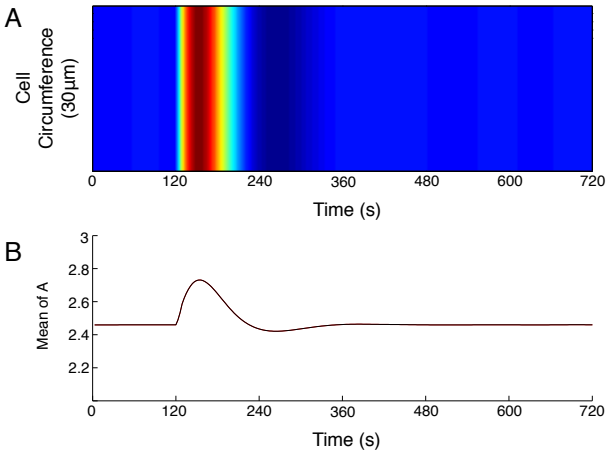

Fig. 5.7: **Response of the modified Meinhardt model to a pulse of activation.** Using the parameters from the fit of the modified Meinhardt model with the modified value for D_c, simulations are used to determine the behaviour of the fitted model to a short lived signal. Simulations are carried out on a cell of 100 nodes with the distance between the nodes of $\Delta x = 0.2$. Starting from uniform initial conditions, models are run for a period without an external signal to reach equilibrium before the signal scheme begins. After a period 2 minutes without signal, the cell is exposed to a signal for a period of 10s. (A) Heat map of the cell surface. (B) The mean value of the activator.

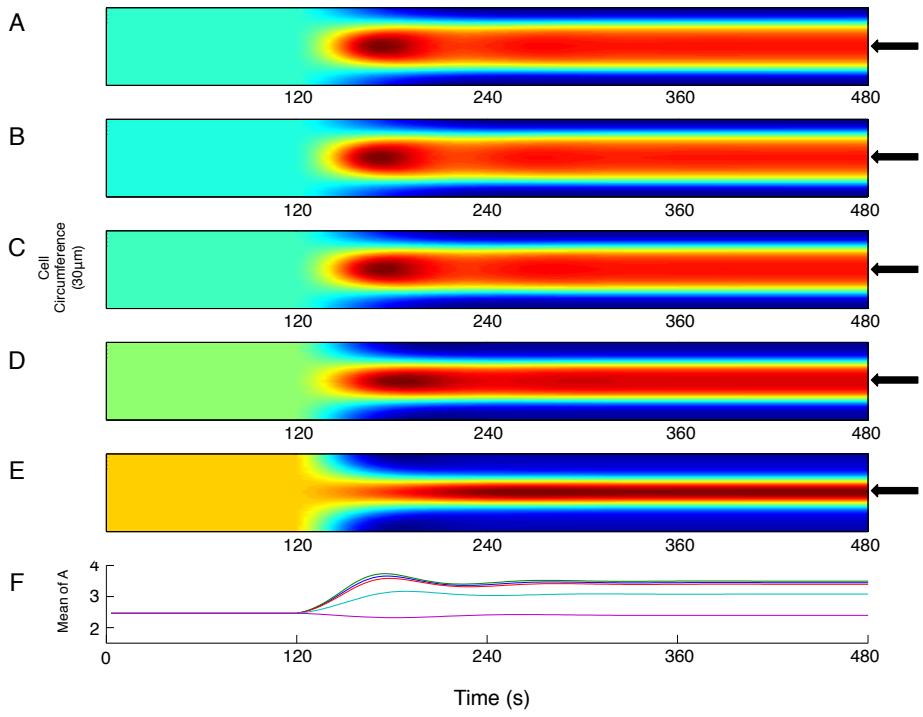

Fig. 5.8: **Response of the modified Meinhardt model to changing the strength of the external signal.** Using the parameters from the fit of the modified Meinhardt model with the modified value for D_c, simulations are used to determine the behaviour of the fitted model to external stimuli of vary strength. Simulations are carried out on a cell of 100 nodes with the distance between the nodes of $\Delta x = 0.2$. Starting from uniform initial conditions, models are run for a period without an external signal to reach equilibrium before the signal scheme begins. Each scheme begins with a period of 2 minutes without signal, and then a signal of varying strength is started opposite node 50 (black arrow) for a period of 10 minutes. (A) Signal strength 0.5Pa. (B) Signal strength 1Pa. (C) Signal strength 1.5Pa. (D) Signal strength 2Pa. (E) Signal strength 2.5Pa. (F) Mean activator concentration in the half of the cell facing into the signal. Dark blue line - 0.5Pa. Green line - 1Pa. Red line 1.5Pa. Light blue 2Pa. Pink line 2.5Pa.

its affect on model behaviour. It was varied in strength between 0.5Pa and 2.5Pa, Figure 5.8. There is little difference between the behaviour when the shear strength is between 0.5-1.5. As the strength increases past this point the front of activation becomes narrower, and the mean value of the activator in the front half of the cell decreases. The total amount of activator on the cell boundary also decreases, but the proportion in the front half of the cell remains the same, at 65%.

When the shear stress is increased to 2Pa front formation is slowed, Figure 5.8 F. This is in accordance with the results from the *Dictyostelium* repolarisation data to which the models were fitted (Dalous et al. 2008), and has not been lost with the change of the parameter D_c. It takes 69s to reach the first peak, as opposed to 57s when $P = 1$Pa. These times are similar to those in the data, but it does not have the delay in front formation that characterises the repolarisation of cells at 2.1Pa.

These simulations have shown some of the limitations of including the shear stress in the model. This is due to the formulation of the replacement for the inhibitor $b = 1 + \beta_0(P^2 - \beta_1 * P)$. When $P < \beta_1$, $b < 1$, and when $P > \beta_1$, $b > 1$. As $\beta_1 = 1.84$Pa, this explains the decrease in the activator levels for $P = 2$Pa and above. In this case, b is playing an inhibitory role on the product of a, where as it facilitates production of a when $P < \beta_1$. Further increasing P leads to further decreases in the strength of the front, till it no longer forms for $P > 3$Pa. At flows of this strength cells would be unlikely to be able to stay on the substrate (Dalous et al. 2008). When the pressure of the flow was reduced to below 0.9Pa, instead of repolarising into the flow, *Dityostelium* cells would reorientate by turning to face into the flow (Dalous et al. 2008). When testing the fitted model with low flow pressures (< 0.5Pa) no evidence was found to indicate that a similar behaviour was

D_I (µm^{2}s^{-1}) value	10^{-4}	10^{-3}	10^{-2}	10^{-1}	10^{0}
Peak of R	4.5	4.48	4.5	4.39	3.89
Time of Peak	147s	147s	150s	153s	147s
Time to Half	324s	321s	297s	339s	489s

Tab. 5.5: Peaks of R when fixing the diffusion constant D_I. The peak of R is the maximum value of R taken by the new front. Time of peak is the time when R reaches this value and time to half is the time taken for the intensity of R to reach half of the peal value. All values are calculated from the central nodes where the external signal is strongest.

happening.

5.7 Fixing Diffusion in the Levchenko Model

As detailed in Section 4.1, diffusion of the inhibitor is necessary for the response to an external signal to be non-transient. The value of the diffusion constant D_I obtained during fitting was $2.39 \times 10^{-}5$ µm^{2}s^{-1}, and found to be practically unidentifiable during PLE analysis, Section 4.5.2. As simulations extending the time period of the Levchenko model fit show that the response to flow reversal is transient (Figure 5.1) the diffusion parameter may not have been of sufficient value to force the system into non-transience.

The Levchenko model was refitted to the *Dictyostelium* repolarisation data with the diffusion constant D_I fixed. Simulations extending the time period were carried out to determine whether or not the response to flow reversal remains transient, Figure 5.9. For all values that the diffusion constant was fixed to, the response to flow reversal remains transient.

The rate at which the new front disperses does change depending on the value of the diffusion constant. The highest value of the new front was calculated, along with when this peak occurred and how long it took for R to reach half this value. The time of the peak did not change with variation of D_I, staying within one frame of 150s. When $D_I = 2.25$ µm^{2}s^{-1}, the value

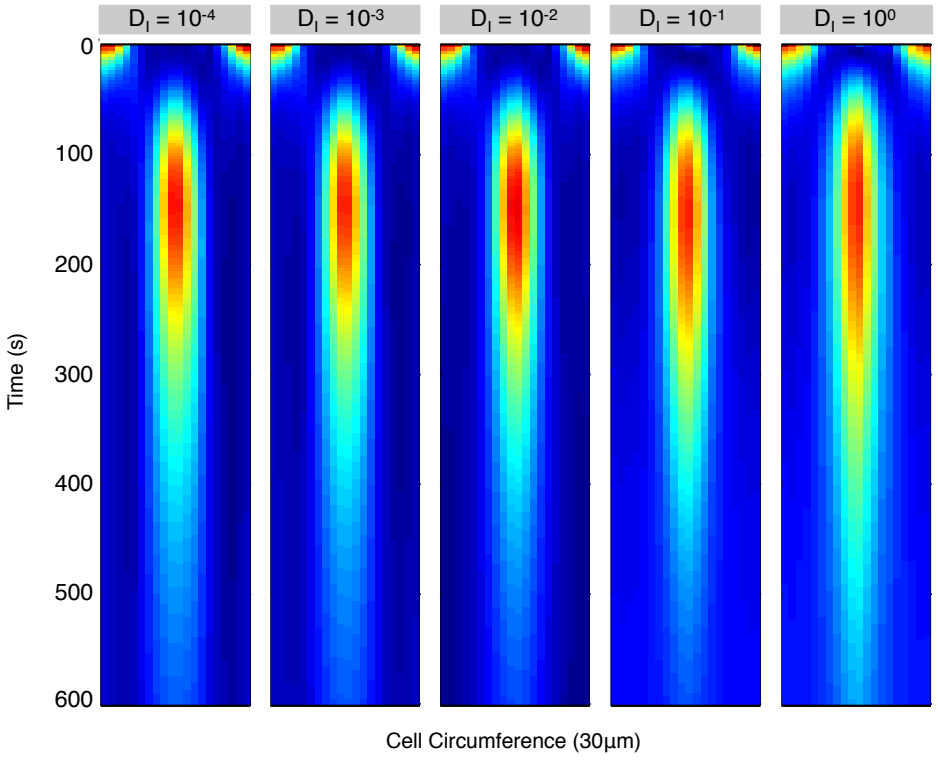

Fig. 5.9: **Long term behaviour of the Levchenko model when fitted with a fixed diffusion constant.** The Levchenko model was fitted with the diffusion constant D_I fixed to a predetermined value, ranging from 2.25×10^{-4} $\mu m^2 s^{-1}$ to 2.25 $\mu m^2 s^{-1}$. Simulations were carried out using the parameter values and initial conditions taken from the fit to the large shear data, for a period of 10 minutes from the point of flow reversal, $t = 0$. Each simulation is shown as heat map using the MATLAB heat map Jet with the header signifying the value that D_I is fixed to.

of the peak was lowest, and took longest to reduce to half the peak value.

5.8 Modifying the Levchenko Model

In the fit of the Levchenko model to the *Dictyostelium* repolarisation data, several parameters were found to be unidentifiable, Section 4.5.2. The model parameters k_R and R_T were found to be linked due to the size of R_T relative to the response element R. When one was varied, the other changed so that the product remained unchanged. Only when R_T is decreased to a sufficiently low value does the fit of the model change (pointwise CI lower bound of 34.8).

To remove this behaviour the term $(R_T - R)$ is removed from the rate of change of R. This is done through simplying the production rate of the response element, R. As $R_T >> R$, $k_R A(R_T - R)$ can be approximated by $k_R A R_T$. The value of R_T was set to 1, and the value of k_R set to the product of the previous values of k_R and R_T. Along with the change in the external signal this results in the following formulation for the modified Levchenko model.

$$\begin{aligned}
\frac{\partial A}{\partial t}(x,t) &= k_A s^*(x) - k_{-A} A \\
\frac{\partial I}{\partial t}(x,t) &= k_I s^*(x) - k_{-I} I + D_I \frac{\partial^2 I}{\partial x^2}(x,t) \\
\frac{\partial R}{\partial t}(x,t) &= k_R A - k_{-R} I R
\end{aligned} \tag{5.19}$$

In the previous model formulation, the reservior term R_T acted as a cap on the level of the response, and would reduce the rate of production of the response element as more was made. In the model fit, the value of R_T was such that this cap was much greater than the amount of the response element ever present, and as such the change in the production of the response

element as more was produced was not occuring. In the new formulation, there is no reservior of unactivated response element, and its production is proportional to the level of the activator.

The steady states for the activator and inhibitor are unchanged from the original Levchenko model, Equations 4.1 and 4.3. The steady state for the response element is

$$\begin{aligned} R_{ss} =& \frac{k_R A_{ss}}{k_{-R} I_{ss}} \\ =& \frac{k_R k_A s^*(x)}{k_{-R} k_{-A} (e^{\gamma x} F_2(t) + e^{-\gamma x} F_1(t)) - \frac{k_I}{2\sqrt{D_I}\sqrt{k_{-I}}} (e^{\gamma x} \int e^{-\gamma x} s(x) dx - e^{-\gamma x} \int e^{\gamma x} s(x) dx)} \end{aligned} \tag{5.20}$$

where $\gamma = \sqrt{\frac{k_{-I}}{D_I}}$ and $F_1(t)$ and $F_2(t)$ are functions of t depending on the initial conditions as in Section 4.1. With diffusion present, the steady state of the response element is still dependent on the external signal.

5.8.1 Fitting Results

The modified Levchenko model was fitted to the same *Dictyostelium* repolarisation data set as used for model fitting in Section 4.4. The χ^2 value for the fit is shown in Table 5.6. The modified model is able to fit to the data as well as the original model (change of χ^2 from 155 to 156), with the values for the change in χ^2 for each data set varying between 0.1 and 0.8 between the modified and the original model.

When comparing the front/back behaviour of the fitted model to the data it is able to match it well, Figure 5.10. In the repolarisation conditions, the degradation of the old front in the model closely follows the degradation observed in the data. Up to the point where the fluorescence levels in the front and back cross the model is able to match the behaviour of the new

	High Stress	Low Stress	Flow → No Flow	Total
χ^2	29.3	59.6	66.8	156
mean RE	1.77	1.97	2.21	2.02

Tab. 5.6: χ^2 and relative error values for the modified Levchenko model, Equation 5.19, fitting to *Dictyostelium* repolarisation data. χ^2 is the sum of squared errors difference between the model and the data, Equation 2.6. Mean RE is the relative error of the model fit averaged over the number of image frames in the data set.

front. This intersection is also conserved in the model fit, occurring at the same time and fluorescence value.

However, after this point the model is not able to match the data from the new front as well. For the high shear stress condition, the model fit matches the data till around 141 seconds, where it plateaus at a value of 3 before beginning a slight decrease. The data continue to increase, reaching a plateau of 3.5. For the low shear stress condition, after the intersection between the front and back values, the model increases at a lower rate than that of the data, reaching the plateau value of 3.5 at 100 seconds. It also then shows slight degradation before the end of the fit. With the flow to no-flow condition, the model is able to match well the front/back behaviour, approaching the equilibrium between the two.

When using heat maps to compare the model fit to the low and high shear stress data, it is able to capture the width of the new front for the flow reversal conditions. The delay in front strength with the low shear stress fit can also be observed.

5.8.2 Identifiability Analysis

With the modified model now fitted to *Dictyostelium* repolarisation I proceeded to perform the PLE analysis to determine the identifiability of the

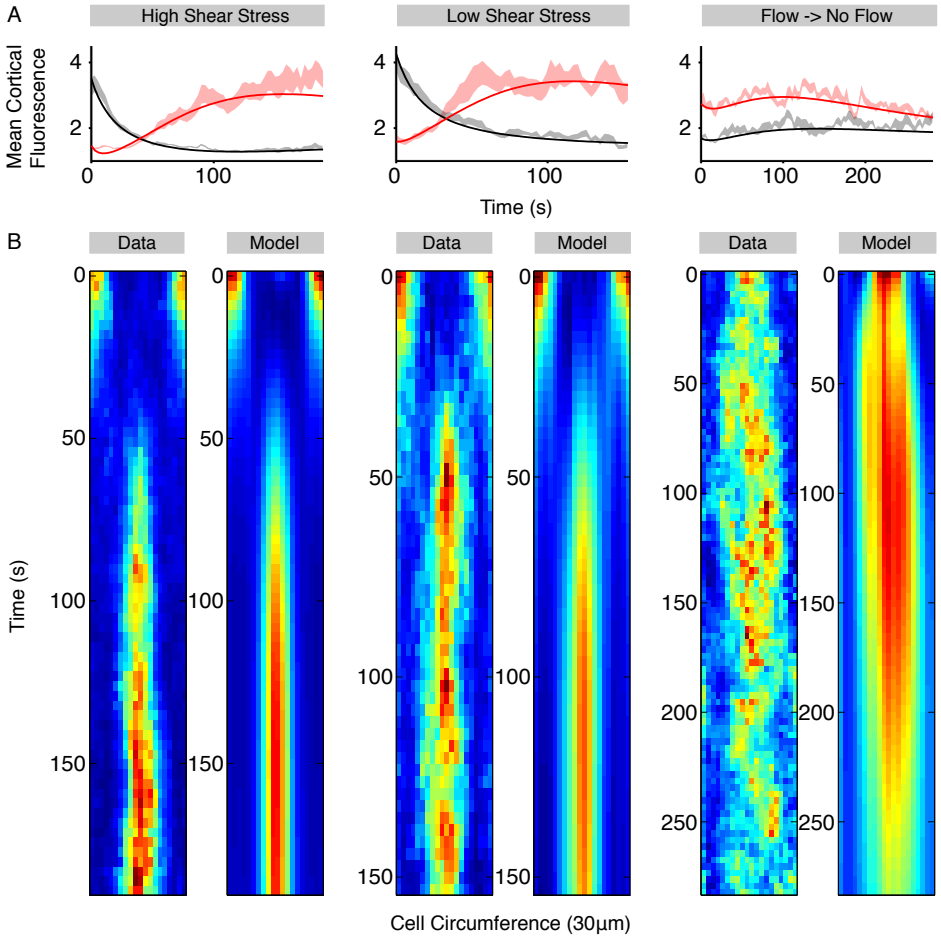

Fig. 5.10: **Fit of the modified Levchenko model.** The model fit to *Dictyostelium* repolarisation data is shown through front/back comparison (A) and through heat maps (B). Each column shows the fitting to a separate condition as signified by the header. The model used for fitting is shown in Equation 5.19, with parameters conserved between data sets, with the exception of dy. (A) The data and model fit are split into two halves, and the mean for each half plotted. The front half (black line) faces towards the external signal (for $t \leq 0$ for flow to no-flow, $t \geq 0$ otherwise) with the back half (red line) facing in the other direction. The solid line shows the mean for the fitted model, the shaded area shows the standard error of the mean for the data. (B) The heat maps show either the data or model fit as indicated by the headers and coloured using the MATLAB heat map Jet.

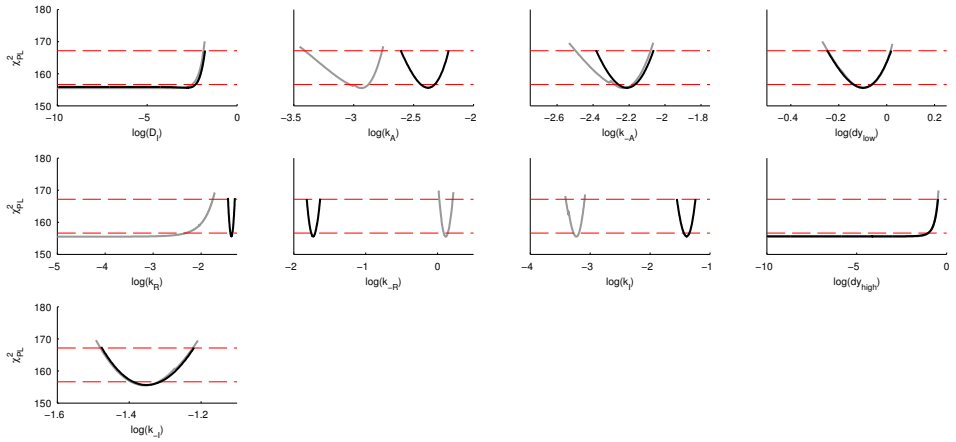

Fig. 5.11: **PLE analysis of the modified Levchenko model.** For each parameter in the modified Levchenko model the PLE (black line) is shown with the pointwise (lower red dashed horizontal line) and simultaneous (upper red dashed horizontal line) confidence interval thresholds. The intersection between the lines yields the boundaries of the confidence interval. Out of 9 parameters, 7 were found to be identifiable with 2 being found to practically unidentifiable. Grey lines show the PLEs of parameters conserved with the Levchenko model analysed in Section 4.5.2.

fitted parameters. From the PLE analysis shown in Section 4.5.2, two parameters, R_T and r_a, are no longer included in the model, leaving nine parameters that are fitted.

Of these parameters, seven were found to be identifiable, and two were found to be practically unidentifiable, Figure 5.11. When compared to the profiles obtained from the analysis of the fit of the original model, five parameters (D_I, k_{-A}, k_{-I}, dy_{low} and dy_{high}) have almost unchanged profiles. The parameters k_A, k_{-R} and k_I are still identifiable, however due to a change in the values obtained during fitting the profiles no longer overlap. The parameter k_R shows the greatest change, now being found to be identifiable after being practically unidentifiable in the earlier analysis. This is due to the reformulation of the model.

5.9 Long Term Simulations with the Modified Levchenko Model

Simulations were conducted using the modified Levchenko model to investigate it's behaviour past the point of fitting. The number of nodes on the cell surface was increased by a factor of 5 to 100 with models simulated for a period without signal to reach equilibrium before a signal scheme is applied. All signal schemes consisted of two minutes without an external signal, to show the equilibrium, followed by a change in the external signal. Simulations are carried out with both the original and modified Levchenko models using the fitted parameters.

Not all parameters in the Levchenko model are identifiable. To minimise the use of unidentifiable parameters, the identifiable parameter dy_{low} will be used in simulations, as opposed to the unidentifiable dy_{high}. The diffusion constant D_I is still unidentifiable however.

The first signal scheme the models were simulated with was an external signal in the same position for 30 minutes, Figure 5.12 A. For both models, there is a lack of response opposite the signal with a large concentration of the response element on the other side of the cell that dissipates after 20 minutes. For both models $k_{-I} > k_{-A}$, the inhibitor degrades faster than the activator. When the signal begins the external signal here decreases (due to the cosine in $s(x)$) resulting in a decrease in production of the activator and inhibitor. The inhibitor decreases at a greater rate than the activator, causing the production of the response element, which decreases as the concentration of the activator goes below the level to sustain it.

Increasing the diffusion constant for the inhibitor, D_I, allows the formation of a stable front opposite the external signal, Figure 5.12 B. The inhibitor diffusion constant for the original model is increased by a factor of 10^4 to 0.239 $\mu m^2 s^{-1}$. The inhibitor diffusion constant for the modified model is

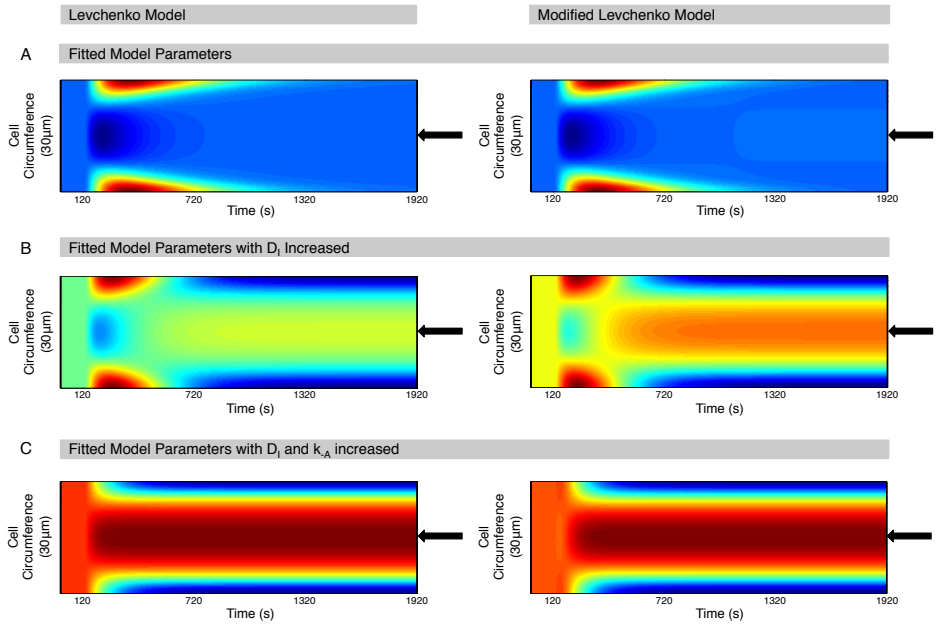

Fig. 5.12: **Long term behaviour of the fitted modified Levchenko model.** Using the parameters from the fit of the non-modified (first column) and modified (second column) Levchenko model, simulations are used to determine the long term behaviour of the fitted model (A), and again with a modification in the parameter set (B,C). Simulations are carried out on a cell of 100 nodes with the distance between the nodes of $\Delta x = 0.2$. Starting from uniform initial conditions, models are run for a period without an external signal to reach equilibrium before the signal scheme begins. The activator values around the cell circumference at the end of the simulation are plotted to the right of the heat map. After a period of 2 minutes without a signal, a signal is started opposite node 50 (black arrow) and remains for a period of 30 minutes. (A) Simulations use the parameter set obtained during fitting. (B) The diffusion constant of the inhibitor, D_I increased. (C) Both the diffusion constant and the parameter k_{-A} are increased. For the modified Levchenko model, the parameter k_A is also increased.

increased by a factor of 100 to 0.398 $\mu m^2 s^{-1}$. Increasing the rate of diffusion of I decreases the concentration that forms opposite the external signal, allowing the front to be formed. For the original Levchenko model, it takes roughly 15 minutes from when the signal is introduced to reach the peak of this front. The modified Levchenko model takes roughly 20 minutes to reach its peak, which is greater than that of the original model.

The peaks of activation that persist on the other side of the cell, are removed by increasing the parameters k_A and k_{-A}, Figure 5.12 C. For the original Levchenko model, the parameter k_{-A} is increased by a factor of 10 to 5.88×10^{-2} s^{-1}. It takes less time to reach the peak value in the front, only 3.5 minutes. However it is to a value that is 7.7% of the previous peak value.

For the modified Levchenko model, both k_A and k_{-A} were increased by a factor of 5 to 2.10×10^{-2} and 3.07×10^{-2} respectively. Increasing just k_{-A} removed the peaks of activation on the other side of the cell, and increasing k_A kept the value of the peak at the front at the same value as when D_I was increased by itself. The time taken to reach the maximum of the peak was decreased to 3 minutes.

To investigate how the model responded to varying stimuli, I used the same signal scheme as with the modified Meinhardt model, Section 5.6. During each scheme the external signal changed every 10 minutes, changing position, turning on/off or doubling the peak of activation.

The first scheme tested the response to a change in the signal direction to the opposite side of the cell and then back, before being removed, Figure 5.13 A. This is akin to the shear flow reversal experiments with *Dictyostelium* (Dalous et al. 2008), to which the models were fitted . The model is able to respond to the change in signal, with the old front dissipating as the new

front is built. The mean fluorescence values for each half of the cell were compared, Figure 5.13 B. When the signal is present, the mean of the side opposite the signal tends to a plateau of value 1.89. On the other side of cell, the mean value reaches 1.26 before the signal changes position. If the signal change did not occur, the minimum reached would have been 1.25.

After the signal is reversed, the new front reaches the plateau value after 4 minutes. This is in contrast to the experimental data, where under a shear stress of $0.9Pa$, *Dictyostelium* cells were able to form a new front after 60 seconds (Dalous et al. 2008). In these data, the new front had a mean fluorescence value of 3.75, compared to the value of 1.89 here. In the data, the fluorescence of the back was found to be 1.75, which is closer to the value of the back in the simulations of 1.25.

When the signal is reversed, there is an increase in the intensity of the front before it dissipates. A possible reason for this to occur may be the difference between the terms k_{-I} and k_{-A}, which are the rate of degradation of I and A respectively. As $K_{-I} > k_{-A}$, the level of inhibitor decreases at a faster rate than that of the activator, resulting in the production of more of the response element before the amount of activator decreases sufficiently. The inhibitor also diffuses, adding to this effect.

The next signal scheme was of a signal that moved 90° around the cell every 10 minutes, Figure 5.13 C. As the signal moves around the cell cortex, the front follows to face the new position of the external signal. After 3.5 minutes the new front reaches the mean plateau of 1.89, the same as for when the signal was reversing. The old front does not break down, but instead travels across the cell cortex to be opposite the new external signal position.

The final signal scheme consists of a signal that starts opposite one side of the cell, before being removed and replaced with a new signal that faces against

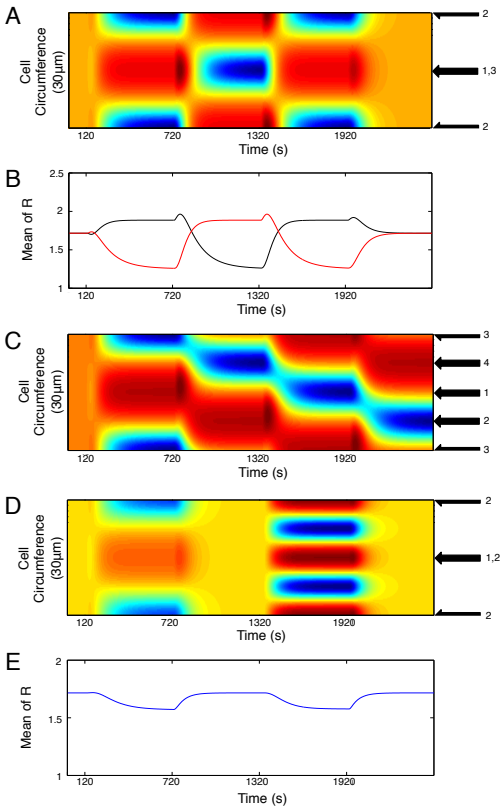

Fig. 5.13: **Response of the modified Levchenko model to a changing external signal.** Using the parameters from the fit of the modified Levchenko model with the modified value for D_I and increased k_A and k_{-A}, simulations are used to determine the behaviour of the fitted model to varying external stimuli. Simulations are carried out on a cell of 100 nodes with the distance between the nodes of $\Delta x = 0.2$. Starting from uniform initial conditions, models are run for a period without an external signal to reach equilibrium before the signal scheme begins. Each scheme begins with a period of 2 minutes without signal, and each signal is simulated using the value for dy obtained from fitting to the low shear stress. (A) A signal is started opposite node 50 (black arrow 1) for a period of 10 minutes. It is then moved to opposite node 100 (black arrow 2) for a period of 10 minutes. The signal is returned to its original position (black arrow 3) for a period of 10 minutes before being removed. (B) The mean value for the response element R in the two halves of the cell. The cell is split into two halves, nodes 25-74 opposite signals 1 and 3 (black line) and nodes 75-24 opposite signal 2 (red line). (C) A signal is started opposite node 50 (black arrow 1). Every 10 minutes in the simulation, the signal is moved 25 nodes around the cell circumference (black arrows, 2, 3, 4). (D) A signal is begun opposite node 50 for a period of 10 minutes (black arrow 1) before being removed for a period of 10 minutes. A second signal begins where the frequency of the external signal has been doubled to create a signal with two peaks, opposite nodes 50 and 100 (black arrows 2). This remains for a period of 10 minutes before being removed for 10 minutes. (E) The mean value for the response element R in simulation C.

two sides of the cell at once, Figure 5.13 D. This new signal is achieved by doubling the frequency of the external signal. This doubled signal results in a doubling on the fronts, with two peaks of activation forming. Tripling and quadrupling the frequency results in a corresponding increase in the number of fronts.

The mean value for the response element, R, around the cell cortex was calculated when exposed to the last signal scheme, Figure 5.13 E. When a signal is started, the mean amount of response element in the cell cortex decreases. Once the signal is removed it returns to equilibrium.

In Chapter 4 3 models cell polarisation models were fitted to *Dictyostelium* repolarisation data. Two of those models, the Meinhardt and Levchenko models, were further analysed and modified to improve their identifiability and behaviour past the point of fitting. The Meinhardt model was reduced to an identifiable two variable model. Linear stability analysis was used to form a constraint on the difussion coeffcients to remove front splitting. The Levchenko model was modified to reduce it to having 2 unidentifiable parameters. A further modification of the parameter set resulted in fronts of activation becoming stable.

6. FITTING TO SINGLE CELL DATA

In Chapters 4 and 5 I fitted models to mean cell repolarisation data. Instead of fitting to this mean repolarisation data, models can instead be fitted to individual cell data. For fitting to cell repolarisation, data was taken fromt the cells that are used to form the mean cell data that were used in fitting earlier chapters. This gives 3 different conditions, flow reversal for high and low shear stress, and the removal of flow.

In addition, the models were fitted to data taken from unstimulated cells. This was conducted using fluorescence data taken from vegetative *Dictyostelium*. For both repolarising and unstimulated cells, the Meinhardt and Levchenko models were fitted using the modified Meinhardt model shown in Section 5.4 and the unmodified Levchenko model shown in Section 2.7.3.

6.1 Single Cell Repolarisation Data

Before being used for fitting, the single cell repolarisation data were inspected to ensure that none of the data sets exhibited anything that would disrupt the fitting. Three of the data sets were found to have problems, and were removed from the sets used during fitting (2 high shear stress, 1 low shear stress). On one, the time appeared to be labelled incorrectly, another appeared to have a 30s period where the cell cortex data was shifted by 90°, and the last a period of 90s where there was no fluorescence measured on the cell cortex during flow. None of the other data sets showed any similar

problems. These data sets had been used in the fitting to mean cell data. Should the fitting be replicated, then new mean cell data should be created that omitted these data sets.

The models were fitted to each experimental condition separately, fitting to all cells in the condition simultaneously. Each model parameter was fitted to be the same value over all cells taken from the same condition. After this the models were fitted to all three conditions simultaneously, resulting in a set of model parameters for the individual cell repolarisation data over all three conditions. The fitting process was the same as for when fitting to mean cell data, with the exception being that the standard deviation in the chi-squared sum was calculated using the formula in Equation 2.7.

6.2 Fitting the Meinhardt model to Single Cell Repolarisation Data

The Meinhardt model used during fitting was the modified Meinhardt model described in Section 5.4, with the variable b replaced the constant $b = 1 + \beta_0(P^2 - P\beta_1)$, and with dy being a global parameter. The χ^2 and mean relative error from the fits are shown in Table 6.1, and the parameter values obtained in the fits in Table A.8. The first row details the χ^2 mean relative error when fitting to the conditions seperately, with the second row showing the values obtained from the combined fitting to all 3 conditions simultaneously.

There is a small difference in quality between the fits when fitting the conditions seperately, and with the combined fitting. As would be expected, the χ^2 and relative error values are lowest with the seperate fittings. The greatest increase in relative error is with the low shear stress condition, increasing by 0.37 (7.51%). The greatest increase in χ^2 is with the flow to no flow condition, increasing by 7.7×10^3 (11.3%). This compares to an

		High Stress	Low Stress	Flow → No Flow	Combined Total
Seperate Fitting	χ^2	4.39×10^4	2.13×10^4	6.80×10^4	1.33×10^5
	mean RE	4.71	4.93	6.00	5.31
Combined Fitting	χ^2	4.62×10^4	2.40×10^4	7.57×10^4	1.46×10^5
	mean RE	4.74	5.30	6.31	5.52

Tab. 6.1: χ^2 and relative error values for the Meinhardt model fitting to *Dictyostelium* repolarisation data. The χ^2 value is the chi-squared sum of squared errors difference between the model and the data. The mean RE value is the relative error of the model fit averaged over the number of image frames in the data set. The seperate fitting details the results of fitting to each condition seperately, and the combined fitting details the results of fitting to all conditions simultaneously. The combined total column indicates the sum of the χ^2 for all 3 conditions, and the mean of the mean relative error from all 3 conditions.

increase of only 5.17% in the relative error.

The high shear stress condition has the least change in both χ^2 and relative error, 5.23% and 0.637% respectively. It is also the condition with the lowest relative error, implying that the model is able to fit best here, and loses the least in terms of quality of fit when considering other conditions.

When comparing the fitted parameter values, Table A.8, the parameters obtained from just fitting to the shear stress conditions are similar to those obtained when fitting to the combined data sets. Out of 11 parameters, only 2 are not of the same order of magnitude, with the difference being no greater than 1. Of the parameters obtained from the fit to just the flow to no-flow condition, only 2 out of 8 are the same order of magnitude, with differences going up to 3 orders of magnitude. The greater change in parameters for the flow to no-flow fit may explain the greater increase in χ^2 relative to that of the shear stress fits.

The diffusion constants can be compared to that of the cAR1 cAMP receptor which was measured to be 1.4×10^{-2} $\mu m^2 s^{-1}$ (Keijzer et al. 2011). This

is the same order of magnitude as the majority of the diffusion constants obtained from the fitting. The value for D_a from the seperate fit to the flow to no flow data was the most different, with an order of magnitude of 10^{-5}. When comparing the quality of fit to that obtained when fitting to the mean repolarisation data, Section 5.4, the mean relative error is used. In the combined fitting, the error more than doubles for all conditions, increasing by 140-160% with an increase of the total error of 150%. This increase shows that the model is better able to fit to the mean cell data. A contributing factor to this increase would have been the increase in the amount of data points used in the fitting, which increased by 1473%.

When comparing the fitted parameters taken from the combined mean and individual cell data fits, only *dy* differed in its order of magnitude, having a lower value when fitted to the individual cell data. This parameter controls the asymmetry of the external signal s. As it is lower, there is a smaller difference in the strength of the signal between the front and the back of the cell.

Of the remaining 10 parameters, 5 were inside the confidence interval obtained from the PLE analysis (D_a,b_c,r_a,r_c,β_1). With the exception of the asymmetry external signal, the dynamics of the fitted model do not change much when going from fitting the mean data to the single cell data.

6.3 Fitting the Levchenko model to Single Cell Repolarisation Data

The Levchenko model used during fitting was the original model with the modifications to improve parameter identifiability shown in Section 4.5.2. The χ^2 and mean relative error from the fits are shown in Table 6.2, and the parameter values obtained in the fits in Table A.9.

As found when fitting the Meinhardt model, the quality of fit was better

		High Stress	Low Stress	Flow → No Flow	Combined Total
Seperate Fitting	χ^2	4.36×10^4	2.04×10^4	6.96×10^4	1.34×10^5
	mean RE	4.69	4.91	6.13	5.35
Combined Fitting	χ^2	4.64×10^4	2.24×10^4	7.39×10^4	1.43×10^5
	mean RE	4.90	5.09	6.36	5.57

Tab. 6.2: χ^2 and relative error values for the Levchenko model fitting to *Dictyostelium* repolarisation data. The χ^2 value is the chi-squared sum of squared errors difference between the model and the data. The mean RE value is the relative error of the model fit averaged over the number of image frames in the data set. The individual fitting details the results of fitting to each condition individually, and the combined fitting details the results of fitting to all conditions simultaneously. The combined total column indicates the sum of the χ^2 for all 3 conditions, and the mean of the mean relative error from all 3 conditions.

when fitting to the data conditions seperately. The greatest increase in the relative error is in the fit to the flow to no-flow condition, increasing by 0.23 (3.75%). The greatest increase in χ^2 in terms of percentage is in the fit to the low shear stress condition, which increases by 9.80%. For all conditions, the percentage increase in χ^2 is greater than the percentage increase in the relative error.

As with the Meinahrdt model fit, the best quality fit in terms of mean relative error was with the fit to the high shear stress condition. However, it does have the highest percentage increase when going from fitting to seperate conditions to the combined fitting (4.48%).

When comparing the combined fit of the Levchenko model to that of the Meinhardt model there is little difference in the χ^2 and relative error values (2.10% for χ^2 and 0.91% for RE). The Meinhardt model fit has the lower relative error, where as the Levchenko fit has the lower χ^2 value.

When comparing the fitted parameter values from fitting to the 3 conditions seperately each parameter varies by at most 1 order of magnitude, Table A.9.

Three parameters, k_R, k_{-R} and k_{-I}, are the same order of magnitude in all 3 conditions. This contrasts with the fit of the Meinhardt model, where the parameters of the fit to the flow to no-flow condition were different to those found when fitting to the shear stress conditions.

In the combined fit, the parameters k_{-R} and k_{-I} keep the same order of magnitude, with the parameter k_R increasing by 2 orders. Every other parameter bar R_T and the 2 dy parameters are within 1 order of magnitude of 2 of the parameter values from the seperate fits. The fitted value for R_T is lower than the values found in the seperate fits by 1-2 orders of magnitude. The fitted values for the parameter dy change the most, changing by 4-7 orders of magnitude.

This level of change contrasts with that experienced by the Meinhardt model. In the Meinhardt model fits, the parameter values of the combined fit were closer to those from the seperate fits to the shear stress conditions than in the Levcehnko model fit.

The combined fitting was compared to the model fitting in Section 4.4 using the mean relative error to judge the quality of fit. The relative error increases for all conditions by between 160-188%. For all conditions in total it increased by 176%. As with the Meinhardt model, it is better able to fit to the mean cell data, which again may be caused by the increase in the number of data points used in the fitting of 1473%.

When comparing the parameter values obtained when fitting to the individual cell data to those obtained from the mean cell data, 3 parameters are of the same order of magnitude, k_A, k_{-A} and k_{-I}. Of these parameters, k_A is inside the PLE confidence interval obtained from the fit to the mean data. Of the remaining parameters, 3 more are within the PLE confidence intervals, k_R, k_{-R} and dy_{high}. When comparing the changes in k_R and R_T, k_R

	Meinhardt	Levchenko
χ^2	2.48×10^3	2.24×10^3
mean RE	1.12	1.04

Tab. 6.3: χ^2 values for the Meinhardt and Levchenko models fitting to individual unstimulated *Dictyostelium*. The χ^2 value is the chi-squared sum of squared errors difference between the model and the data. The mean RE value is the relative error of the model fit averaged over the number of image frames in the data set.

increased by 3 orders of magnitude and R_T decreased by 3 orders of magnitude. This behaviour is consistent with the analysis in Section 4.5.2, where as one increases, the other decreases proportionally.

With a set of fitted parameter closer to that obtained from fitting to the mean cell data, the Meinhardt model has a smaller difference between the 2 fits.

6.4 Unstimulated Cell Motility Fitting

In addition to fitting to repolarisation data, I fitted the Meinhardt and Levchenko models to data taken from unstimulated cells. The models were fitted to actin reporter fluorescence data taken from dual-tagged *Dictyostelium* cells. As the model formulation does not account for the movement of the cell I used vegetative cells to minimise cell movement. Three cells were chosen for fitting and produced data ranging between 3.5-5.5 minutes in length.

Each model was fitted to all 3 cells simultaneously. No values were obtained for the parameters dy, β_0 or β_1 as no external signal was present. χ^2 and mean relative error values for the fit are shown in Table 6.3, and fitted parameter values are shown in Table A.10.

The Levchenko model is able to achieve a better fit, with a lower χ^2 value

and lower relative error. When comparing these values to the ones obtained when fitting the models to the single cell repolarisation data in the previous 2 sections, the relative error for the fit to the unstimulated cells is a fifth of that for the fit to the repolarisation data. This change in the error can be accounted for by the difference in the number of cells used in each fitting, 3 for the unstimulated fitting and 37 for the repolarisation fitting.

With the fit of the Meinhardt model, parameters either remained the same, or dropped by 1, order of magnitude. The exception to this was D_c, which dropped by 6 orders of magnitude to 1.47×10^{-8}. This results in effectively negligible diffusion of the inhibitor, and is similar to what is found in the seperate fit to the flow to no flow condition, where it is 3 orders of magnitude lower than in the fit the shear stress conditions.

With the Levchenko model, there is a greater variation in the values of the parameters. Only 1 parameter, k_A was unchanged in order of magnitude. The rest of the parameters varied by 1-2 orders of magnitude, with the exception of k_I and k_{-I}, which both decreased by 3 orders of magnitude. This slows the rate at which the inhibitor I changes compared to the repolarisation fit.

To see how well it was able to capture the individual cell dynamics the heat maps of cell data were compared to the model fits, Figure 6.1. Notable behaviour is marked on the Meinhardt heat map, labelled with roman numerals. For cell A, there is a front that disappears (i), a front splitting in 2 (ii) and a sustained period of a broad low intensity region (iii). For cell B, there is a front splitting (iv, vi), and merging of two fronts (v). For cell C there is a front moving across the cell cortex (vii), and another example of front splitting (viii). Both models are able to match these behaviours well.

In addition to fitting to mean cell repolarisation data, the Meinhardt and

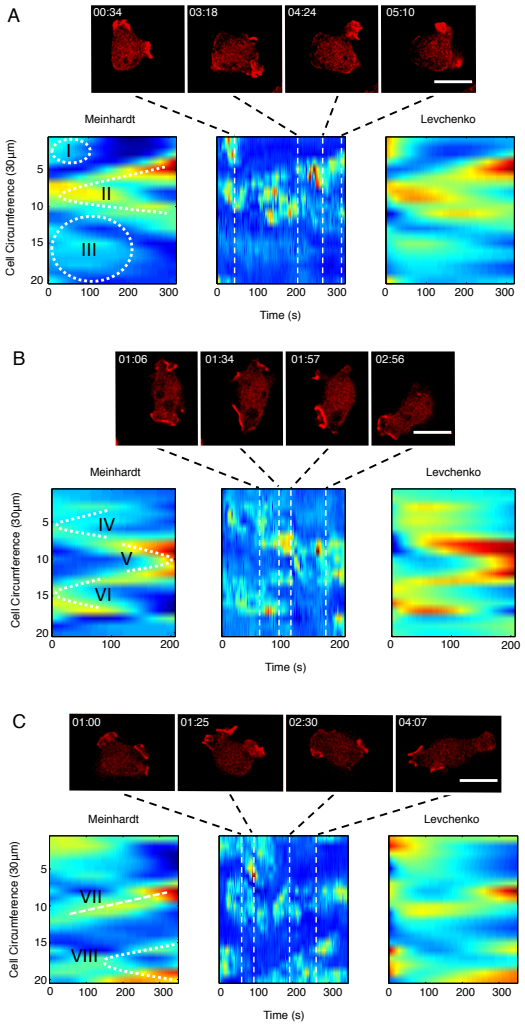

Fig. 6.1: **Comparison of fitting the Meinhardt and Levchenko models to unstimulated *Dictyostelium*.** Cell cortex fluorescence data were extracted from dual-tagged *Dictyostelium* cells using QuimP. The Meinhardt and Levchenko models were fitted to actin reporter fluorescence data taken from 3 cells, A,B and C. The white dashed lines indicate regions of interest, labelled with roman numerals. Heat maps are coloured using the MATLAB colour map Jet. Scale bar is 10µm.

Levchenko models were both able to fit to individual cell repolarisation data, as well as data taken from unstimulated cells. The values of fitted parameters from the fit of the Meinhardt model to the individual cell repolarisation data are closer to those from the fit to the mean cell data than for the Levchenko model. The parameter values obtained when fitting to the unstimulated data follow a similar pattern, with the values from the fit of the Meinhardt model closer to those obtained when fitting to the repolarisation data than with the Levchenko model. The exception to this is the value of the diffusion coefficient for the inhibitor c. It is fitted with a much lower value to data in the absence of flow than to data where there is flow present.

7. DISCUSSION AND CONCLUSIONS

7.1 Dictyostelium *Data Analysis*

I was able to extend the single cell analysis from Bosgraaf et al. (2009) to cell population data. With the analysis of the correlation between cortex fluorescence and protrusion there was a clear difference between vegetative and developed cells. With developed cells there is a clear increase in protrusion, which would be expected given that developed *Dictyostelium* cells are more motile. The rate at which the mean protrusion speed increases in developed cells is 3 times the rate it increases in vegetative cells.

There has been recent work on coupling cell polarity models with dynamic membranes using finite element methods (Croft et al. 2015, Elliott et al. 2012). These use cell polarity models to determine protrusion of the cell membrane. A model incorporating actin and myosin could instead use these values from the protrusion analysis to guide the speed of membrane protrusion and retraction.

The flow chamber experiments were unsuccessful in replicating the repolarisation experiments of Dalous et al. (2008). They failed to respond to flow in the manner shown in Dalous et al. (2008) at any shear stress between 0.9-2.1Pa. I was able to image cells moving with flow, and detaching from the substrate whilst under flow, but non polarised into the flow whilst remaining stationary. Zhu et al. (2014) were able to trigger migratory responses in *Dictyostelium* and demonstrate mechanotactic cellular trapping using flows

with a shear stress $\leq$ 5Pa. These were analysed using phase contrast images, and do not show the details of the actin/myosin response.

I was not able to meet the objective of obtaining more *Dictyostelium* repolarisation data, but I was able to obatin fluorescence data of cells undergoing random motility.

7.2 Model Fitting

I was able to successfully fit three reaction-diffusion models of cell polarity to experimental data of repolarising *dictyostelium*. Identifiability analysis was used to determine parameter identifiability, using the PLE method. This was used to make modifications to the models that resulted in a fully identifiable Meinhardt model. Simulations motivated a change in the Meinhardt and Levchenko model parameters, after which simulations were conducted which showed the models responding to a variety of stimuli. The models were able to follow a moving signal, and respond when the signal was removed. When exposed to 2 sources of signal simultaneously, the models responded to both equally. This behaviour has been shown with PIP3 in latrunculin treated *Dictyostelium*, were cells responded to 2 simultaneous sources of chemoattractant (Janetopoulos et al. 2004). A weakness of these simulations is their use of parameters that were unidentifiable during fitting, the alteration of parameters outside of the their confidence intervals. In all cases of this I tried to minimise the use of unidentifiable parameters to reduce their possible effects.

It is important to remember that these models have been fitted to mean cell data, and as such differ in certain aspects of their behaviour to what is observed in individual *Dictyostelium* cells, where it would expected to see spontaneous polarisation (Insall 2010). It would also be expected to see

waves of surface activation, a behaviour the model was originally designed to replicate (Meinhardt 1999). The Meinhardt model no longer exhibits either of these behaviours. The Levchenko model, after parameter manipulation, has the same behaviour. It is also no longer transient in its response to an external signal (Levchenko & Iglesias 2002). Using the parameters from the fits to the mean cell data, the simulations show a very focused area of activation. There is a complete removal of any of the individual cell variations in the simulations. This limits its use for individual cells, and makes it more akin to a direction sensing module that couples to a more variable protrusion module, as the Levchenko model was used in Shi et al. (2013). The diffusion coefficient for the activator in the Meinhardt model was found to be similar to that of the cAR1 cAMP receptor. Due to the similarities between shear flow and chemotactic repolarisation, the receptor for one may have similar properties to that for the other.

Despite this, the models were able to fit to individual cell data, both repolarising and unstimulated, albeit with a different parameter set. In the Meinhardt model, the fitted value for the diffusion of the inhibitor c are sufficiently low that the diffusion in negligible, leaving a qualitatively different system where the lateral inhibition of activation is no longer present. Membrane tension has been discussed as an inhibitory mechanism in the growth of protruding front (Tyson et al. 2014). This supports the possibility that when cells change to a highly polarised form of movement, there is a corresponding global increase in membrane tension.

All 3 models considered here are conceptual in design and do not pertain directly to specific biological components. Whilst the activator or response element can be fitted to data detailing actin position, there is no data to fit the other model components to, leaving their behaviour unregulated. In-

stead of using a conceptual model with no direct biological components, biochemical models can be built that use reactions where some of the rate constants have already been determined experimentally. If any parameters are unknown, it is possible to obtain estimates based on expected cell behaviour (Maree et al. 2006).

During model fitting and simulations it assumed that there was no movement in the cell cortex. When fitting I used data from cells where movement was minimised, with the cells used for repolarisation data held in place by the flow, and fitting to vegetative unstimulated cells. Models have been developed that account for movement of the cell cortex (Neilson et al. 2011, Elliott et al. 2012, Tweedy et al. 2013) using the Meinhardt model to guide movement of the cell cortex. Numerical methods are being developed to allow the fitting of cell polarity models that included cortex movement (Croft et al. 2015), and would be an area for further investigation.

The behaviour of the mean front and back fluorescence values was used during model fitting to compare how well the models had fitted. The models were not fitted directly to this, but the asymptotic values and crossover points would have been a useful addition to the data used to fit the models.

To determine parameter identifiability I used the PLE method (Raue et al. 2009, 2010), a method that exploits the likelihood to determine whether or not a parameter is identifiable. This approach relies on the data used in fitting, only gives a local result for identifiable parameters. Another method, Ear Indentifiability Analysis (Karlsson et al. 2012), was attempted but was unsuccessful. Methods exist to check a priori for structural non-identifiabilities. In the case of the models presented here, several structural non-identifiabilites were identified by the PLE analysis, and were resolved. Using a prori methods would have resolved these non-identifiabilities before

fitting, and along with a formal reparameterisation would have reduced the number of parameters that needed to be fitted.

In summary, I was able to develop a framework where I was able to fit mathematical models of cell polarity to repolarisation data of *Dictyostelium*, and motivate model changes. Using simulations I can test the models behaviour against different external stimuli. However, I was unable to generate new experimental data of repolarisation for the testing of model predictions, and for further fitting.

APPENDIX

A. FITTED PARAMETER VALUES

In tables A.1, A.2 and A.3 are the parameter values obtained from fitting the mathematical models in Chapter 4, along with the final results of parameter identifiability analysis. The values for Levchenko parameters k_A and k_I and Otsuji parameter a_2 are post removal of parameter r_a.
In tables A.4, A.5, A.6 and A.7 are the parameter values obtained from fitting the mathematical models in Chapter 5, along with the final results of parameter identifiability analysis on these models.
In tables A.8 and A.9 are the parameter values obtained from fitting the mathematical models in Chapter 6.

Parameter	First Fitted Value	Truncated Fitted Value	Parameter Identifiability	Low CI	High CI
D_a ($\mu m^2 s^{-1}$)	1.09×10^{-1}	9.61×10^{-2}	ident.	7.43×10^{-2}	1.22×10^{-1}
D_c ($\mu m^2 s^{-1}$)	2.63×10^{-2}	2.13×10^{-1}	ident.	1.73×10^{-1}	2.61×10^{-1}
b_a	6.63×10^{-1}	2.88×10^{-1}	ident.	2.54×10^{-1}	3.26×10^{-1}
b_c (s^{-1})	2.16×10^{-2}	2.02×10^{-1}	ident.	1.56×10^{-1}	2.53×10^{-1}
r_a (s^{-1})	2.45×10^{-3}	2.37×10^{-1}	ident.	1.87×10^{-1}	2.91×10^{-1}
r_b (s^{-1})	4.78×10^{-1}	1.00×10^{-5}	prac. un.	-	2.73×10^{-5}
r_c (s^{-1})	8.39	2.35×10^{-1}	ident.	1.82×10^{-1}	2.97×10^{-1}
s_a	2.75×10^{-3}	5.83×10^{-3}	ident.	5.02×10^{-3}	6.81×10^{-3}
s_c	3.76×10^{-1}	3.53×10^{-1}	ident.	3.09×10^{-1}	4.02×10^{-1}
dy_{low}	4.56	1.31×10^{-2}	ident.	1.07×10^{-2}	1.67×10^{-2}
dy_{high}	3.71	1.28×10^{-2}	ident.	8.82×10^{-3}	1.84×10^{-2}
dy_{f-nof}	4.22×10^{-1}	-			
dy_{nof-f}	1.71	-			

Tab. A.1: Parameter values for the fitted Meinhardt model for the fits shown in Chapter 4. Parameter column details the name of the parameter. The four different *dy* parameters correspond to the different flow conditions, low shear stress, high shear stress, flow to no flow, no flow to flow. The first fitted value corresponds to the fits detailed in Section 4.2. The truncated fitted value corresponds to the fits detailed in Section 4.4. Parameter identifiability details the results of the PLE analysis after the analysis detailed in Section 4.5.1, either identifiable or practically unidentifiable. Low CI and high CI detail the lower and higher limits on the CI created by the PLE analysis.

Parameter	First Fitted Value	Truncated Fitted Value	Parameter Identifiability	Low CI	High CI
D_I ($\mu m^2 s^{-1}$)	2.27×10^{-5}	2.39×10^{-5}	prac. un.	-	3.44×10^{-2}
k_A (s^{-1})	4.67×10^{-2}	1.16×10^{-3}	ident.	3.62×10^{-4}	8.56×10^{-3}
k_{-A} (s^{-1})	2.31×10^{-2}	5.88×10^{-3}	ident.	2.96×10^{-3}	8.56×10^{-3}
k_R (s^{-1})	1.08×10^{-3}	1.12×10^{-5}	prac. un.	-	1.92×10^{-2}
k_{-R} (s^{-1})	3.25×10^{-2}	1.30	ident.	1.04	1.66
k_I (s^{-1})	5.61×10^{-2}	5.90×10^{-4}	ident.	3.85×10^{-4}	8.21×10^{-4}
k_{-I} (s^{-1})	2.90×10^{-3}	4.40×10^{-2}	ident.	3.23×10^{-2}	6.16×10^{-2}
r_a	3.61×10^{-2}	-			
R_T	636	1.34×10^4	prac. un.	9.113	-
dy_{low}	8.13×10^{-4}	7.96×10^{-1}	ident.	5.47×10^{-1}	1.06
dy_{high}	1.24×10^{-1}	2.90×10^{-5}	prac. un.	-	3.46
dy_{f-nof}	1.00×10^{-5}	-			
dy_{nof-f}	5.32×10^{-1}	-			

Tab. A.2: Parameter values for the fitted Levchenko model for the fits shown in Chapter 4. Parameter column details the name of the parameter. The four different *dy* parameters correspond to the different flow conditions, low shear stress, high shear stress, flow to no flow, no flow to flow. The first fitted value corresponds to the fits detailed in Section 4.2. The truncated fitted value corresponds to the fits detailed in Section 4.4. Values for k_A and K_I is after analysis in Section 4.5.2. Parameter identifiability details the results of the PLE analysis after the analysis detailed in Section 4.5.2, either identifiable or practically unidentifiable. Low CI and high CI detail the lower and higher limits on the CI created by the PLE analysis.

Parameter	First Fitted Value	Truncated Fitted Value	Parameter Identifiability	Low CI	High CI
D_u ($\mu m^2 s^{-1}$)	3.47×10^{-5}	3.13×10^{-5}	prac. un.	-	1.38×10^{-2}
D_v ($\mu m^2 s^{-1}$)	6.17×10^3	1.06×10^2	prac. un.	17.1	-
a_1 (s^{-1})	2.74×10^{-1}	3.83×10^{-1}	ident.	2.46×10^{-1}	5.57×10^{-1}
a_2	4.83×10^{-1}	2.88×10^{-1}	ident.	2.72×10^{-1}	2.99×10^{-1}
r_a	5.73×10^{-1}	-			
dy_{low}	1.02×10^{-1}	7.62×10^{-2}	ident.	5.40×10^{-2}	1.13×10^{-1}
dy_{high}	9.79×10^{-2}	8.24×10^{-2}	ident.	5.78×10^{-2}	1.23×10^{-1}
dy_{f-nof}	2.76×10^{-2}	-			
dy_{nof-f}	3.99×10^{-2}	-			

Tab. A.3: Parameter values for the fitted Otsuji model for the fits shown in Chapter 4. Parameter column details the name of the parameter. The four different *dy* parameters correspond to the different flow conditions, low shear stress, high shear stress, flow to no flow, no flow to flow. The first fitted value corresponds to the fits detailed in Section 4.2. The truncated fitted value corresponds to the fits detailed in Section 4.4. Value for a_2 is after analysis in Section 4.5.3. Parameter identifiability details the results of the PLE analysis after the analysis detailed in Section 4.5.3, either identifiable or practically unidentifiable. Low CI and high CI detail the lower and higher limits on the CI created by the PLE analysis.

Parameter	Fitted Value	Parameter	Fitted Value	Parameter	Fitted Value
D_a ($\mu m^2 s^{-1}$)	5.92×10^{-2}	D_c ($\mu m^2 s^{-1}$)	7.72×10^{-2}	b_a	7.46×10^{-3}
b_c (s^{-1})	2.51×10^{-1}	r_a (s^{-1})	2.38×10^{-1}	r_c (s^{-1})	2.51×10^{-1}
s_a	3.26×10^{-4}	s_c	6.09×10^{-3}		
dy_{low}	1.28×10^{-6}	dy_{high}	1.04×10^{-3}		

Tab. A.4: Parameter values for the fit of the modified Meinhardt model for the fits shown in Section 5.3. Parameter column details the name of the parameter. The two different *dy* parameters correspond to the different flow conditions, low shear stress, high shear stress.

Parameter	Fitted Value	Parameter Identifiability	Low CI	High CI
D_a ($\mu m^2 s^{-1}$)	9.95×10^{-2}	ident.	7.85×10^{-2}	1.28×10^{-1}
D_c ($\mu m^2 s^{-1}$)	2.20×10^{-1}	ident.	1.81×10^{-1}	2.68×10^{-1}
b_a	2.78×10^{-1}	ident.	2.46×10^{-1}	3.07×10^{-1}
b_c (s^{-1})	2.08×10^{-1}	ident.	1.56×10^{-1}	2.76×10^{-1}
r_a (s^{-1})	2.39×10^{-1}	ident.	1.85×10^{-1}	3.09×10^{-1}
r_c (s^{-1})	2.38×10^{-1}	ident.	1.79×10^{-1}	3.14×10^{-1}
s_a	5.65×10^{-3}	ident.	4.64×10^{-3}	6.69×10^{-3}
s_c	3.40×10^{-1}	ident.	2.99×10^{-1}	3.76×10^{-1}
dy	1.28×10^{-2}	ident.	9.77×10^{-3}	1.65×10^{-2}
β_0 (Pa^{-2})	6.07×10^{-3}	ident.	3.74×10^{-3}	8.93×10^{-3}
β_1 (Pa)	1.84	ident.	1.53	2.12

Tab. A.5: Parameter values for the fit of the modified Meinhardt model for the fits shown in Section 5.4. Parameter column details the name of the parameter. The two different *dy* parameters correspond to the different flow conditions, low shear stress, high shear stress. Parameter identifiability details the results of the PLE analysis after the analysis detailed in Section 5.4.2, either identifiable or practically unidentifiable. Low CI and high CI detail the lower and higher limits on the CI created by the PLE analysis.

Parameter	Fitted Values				
	Fit 1	Fit 2	Fit 3	Fit 4	Fit 5
D_I ($\mu m^2 s^{-1}$)	2.25×10^{-4}	2.25×10^{-3}	2.25×10^{-2}	2.25×10^{-1}	2.25
k_A (s^{-1})	4.79×10^{-3}	5.53×10^{-3}	2.62×10^{-3}	5.82×10^{-4}	4.10×10^{-4}
k_{-A} (s^{-1})	1.33×10^{-2}	1.47×10^{-2}	1.90×10^{-2}	6.36×10^{-3}	4.23×10^{-3}
k_R (s^{-1})	1.06×10^{-4}	1.05×10^{-4}	1.51×10^{-4}	1.41×10^{-4}	6.49×10^{-5}
k_{-R} (s^{-1})	1.49×10^{-2}	1.45×10^{-2}	2.69×10^{-2}	3.21×10^{-2}	1.28×10^{-2}
k_I (s^{-1})	9.46×10^{-3}	9.49×10^{-3}	2.87×10^{-3}	1.91×10^{-2}	6.78×10^{-2}
k_{-I} (s^{-1})	2.09×10^{-3}	2.22×10^{-3}	8.91×10^{-4}	4.34×10^{-2}	5.23×10^{-2}
R_T	2.43×10^3	2.25×10^3	4.17×10^3	1.77×10^3	4.09×10^3
dy_{low}	4.76×10^{-1}	4.75×10^{-1}	3.55×10^{-1}	8.99×10^{-1}	4.56×10^{-5}
dy_{high}	3.29×10^{-1}	2.78×10^{-1}	1.54×10^{-1}	1.60×10^{-5}	3.11×10^{-5}

Tab. A.6: Parameter values for the fitted Levchenko model with fixed diffusion values shown in Section 5.7. Parameter column details the name of the parameter. The two different *dy* parameters correspond to the different conditions with flow, low and high shear stress. The values for the diffusion parameter D_I are fixed before fitting to the values presented. All other parameters are fitted as normal.

Parameter	Fitted Value	Parameter Identifiability	Low CI	High CI
D_I ($\mu m^2 s^{-1}$)	3.98×10^{-3}	prac. un.	-	3.71×10^{-2}
k_A (s^{-1})	4.20×10^{-3}	ident.	2.47×10^{-3}	6.21×10^{-3}
k_{-A} (s^{-1})	6.13×10^{-3}	ident.	4.14×10^{-3}	8.62×10^{-3}
k_R (s^{-1})	4.30×10^{-2}	ident.	3.65×10^{-2}	5.05×10^{-2}
k_{-R} (s^{-1})	1.87×10^{-2}	ident.	1.52×10^{-2}	2.33×10^{-2}
k_I (s^{-1})	4.11×10^{-2}	ident.	2.81×10^{-2}	5.73×10^{-2}
k_{-I} (s^{-1})	4.47×10^{-2}	ident.	3.34×10^{-2}	6.02×10^{-2}
dy_{low}	7.95×10^{-1}	ident.	5.65×10^{-1}	1.05
dy_{high}	7.25×10^{-5}	prac. un.	-	3.31×10^{-1}

Tab. A.7: Parameter values for the fitted modified Levchenko model for the fit shown in Section 5.8. Parameter column details the name of the parameter. The two different *dy* parameters correspond to the different conditions with flow, low and high shear stress. Parameter identifiability details the results of the PLE analysis after the analysis detailed in Section 5.8.2, either identifiable or practically unidentifiable. Low CI and high CI detail the lower and higher limits on the CI created by the PLE analysis.

Parameter	High Shear Stress	Low Shear Stress	Flow → No Flow	Combined
D_a (µm^{2}s^{-1})	4.70×10^{-2}	1.74×10^{-2}	1.01×10^{-1}	8.24×10^{-2}
D_c (µm^{2}s^{-1})	5.27×10^{-2}	2.30×10^{-2}	2.25×10^{-5}	1.04×10^{-1}
b_a	6.11×10^{-2}	3.43×10^{-1}	9.83×10^{-2}	1.42×10^{-1}
b_c (s^{-1})	2.07×10^{-1}	1.81×10^{-1}	6.66×10^{-3}	1.73×10^{-1}
r_a (s^{-1})	2.15×10^{-1}	2.53×10^{-1}	1.27×10^{-2}	2.00×10^{-1}
r_c (s^{-1})	2.12×10^{-1}	2.13×10^{-1}	9.70×10^{-3}	1.87×10^{-1}
s_a	1.14×10^{-3}	4.43×10^{-3}	2.29×10^{-2}	3.15×10^{-3}
s_c	8.66×10^{-2}	4.55×10^{-1}	1.30×10^{-1}	2.02×10^{-1}
dy	3.42×10^{-4}	6.16×10^{-4}	-	6.49×10^{-4}
β_0 (Pa^{-2})	6.22×10^{-3}	1.51×10^{-3}	-	1.72×10^{-3}
β_1 (Pa)	2.79	6.64	-	1.75

Tab. A.8: Parameter values for the fitted modified Meinhardt model for the fit shown in Section 6.2. Parameter column details the name of the parameter. The two different dy parameters correspond to the different conditions with flow, low and high shear stress.

Parameter	High Shear Stress	Low Shear Stress	Flow → No Flow	Combined
D_I (µm^{2}s^{-1})	1.56×10^{-1}	8.08×10^{-3}	4.59×10^{-3}	1.09×10^{-1}
k_A (s^{-1})	1.50×10^{-4}	9.45×10^{-4}	7.04×10^{-5}	1.12×10^{-3}
k_{-A} (s^{-1})	1.65×10^{-2}	6.92×10^{-3}	2.00×10^{-3}	1.58×10^{-3}
k_R (s^{-1})	3.91×10^{-4}	2.21×10^{-4}	7.02×10^{-4}	1.77×10^{-2}
k_{-R} (s^{-1})	3.36×10^{-2}	5.39×10^{-2}	6.52×10^{-2}	2.35×10^{-2}
k_I (s^{-1})	1.22×10^{-3}	2.16×10^{-2}	5.04×10^{-3}	9.30×10^{-2}
k_{-I} (s^{-1})	2.80×10^{-2}	3.57×10^{-2}	1.05×10^{-2}	1.79×10^{-2}
R_T	4.29×10^{2}	1.58×10^{3}	2.99×10^{3}	1.57×10^{1}
dy_{low}	-	4.76×10^{-9}	-	2.76×10^{-5}
dy_{high}	5.26×10^{-8}	-	-	3.36×10^{-1}

Tab. A.9: Parameter values for the fitted modified Levchenko model for the fit shown in Section 6.3. Parameter column details the name of the parameter. The two different dy parameters correspond to the different conditions with flow, low and high shear stress.

Meinhardt Model		Levchenko Model	
Parameter	Value	Parameter	Value
D_a (µm^{2}s^{-1})	5.20×10^{-3}	D_I (µm^{2}s^{-1})	7.16×10^{-4}
D_c (µm^{2}s^{-1})	3.31×10^{-8}	k_A (s^{-1})	1.45×10^{-3}
b_a	1.44×10^{-1}	k_{-A} (s^{-1})	1.78×10^{-4}
b_c (s^{-1})	5.64×10^{-2}	k_R (s^{-1})	1.42×10^{-4}
r_a (s^{-1})	9.47×10^{-2}	k_{-R} (s^{-1})	3.33×10^{-1}
r_c (s^{-1})	6.55×10^{-2}	k_I (s^{-1})	1.15×10^{-5}
s_a	3.05×10^{-3}	k_{-I} (s^{-1})	1.01×10^{-5}
s_c	2.79×10^{-1}	R_T	1.55×10^{2}

Tab. A.10: Parameter values for the fitted Levchenko and Meinhardt models for the fit shown in Section 6.4. Parameter column details the name of the parameter. The model parameters dy, β_0 and β_1 are excluded as no fitted value exists due to there not being an external signal present.

B. POTTERSWHEEL MODEL FILES

B.1 Model Files

Models were written as PottersWheel files as described in section 2.5.3. To calculate the external signal it is first necessary to designate the point which is closest to the signal. As a result of the orientation of the nodes around the cell cortex, the nodes 10 and 11 were pointed opposite the external source. Thus the external signal was considered as originating at node 10.5, exactly between nodes 10 and 11. Using this value, $sin((i-j)/n)$ was calculated and inputted directly into the model file.
The driving input function was used to regulate the direction of the external signal, and to allow it to be removed. This corresponds to the flow reversal and removal conditions that the models were fitted to. By taking either the value 1 or -1 it is possible to flip the orientation of the signal to the opposite side of the cell, following the way the signal changes as flow direction changes. The orientation when the input is positive corresponds to the orientation after the flow is reversed, and the negative to the time before flow reversal. In the case where flow is removed, the input is given the value zero. This removes the asymmetry in the system as there is no longer any flow.

```
% PottersWheel model definition file
function m = Meinhardt_Model()

m              = pwGetEmptyModel();

%% Meta information
m.name = 'Meinhardt_Model';
m.description = ' ';
m.authors      = {};
m.dates = {'2013-02-04'};
m.modelFormat = 3;

%% Default sampling time points
m.t = 0:3:120;

%% X: Dynamic variables
% m = pwAddX(m, *ID, *startValue, fitSetting, minValue, maxValue,
    unit, compartment, name, description, typeOfStartValue,
    designerProps, classname)
m = pwAddX(m,'a1',1,'local',0.0000000001,[],[],'c1',[],[],[],[]);
```

```
m = pwAddX(m,'a2',1,'local',0.0000000001,[],[],'c1',[],[],[],[]);
m = pwAddX(m,'a3',1,'local',0.0000000001,[],[],'c1',[],[],[],[]);
m = pwAddX(m,'a4',1,'local',0.0000000001,[],[],'c1',[],[],[],[]);
m = pwAddX(m,'a5',1,'local',0.0000000001,[],[],'c1',[],[],[],[]);
m = pwAddX(m,'a6',1,'local',0.0000000001,[],[],'c1',[],[],[],[]);
m = pwAddX(m,'a7',1,'local',0.0000000001,[],[],'c1',[],[],[],[]);
m = pwAddX(m,'a8',1,'local',0.0000000001,[],[],'c1',[],[],[],[]);
m = pwAddX(m,'a9',1,'local',0.0000000001,[],[],'c1',[],[],[],[]);
m = pwAddX(m,'a10',1,'local',0.0000000001,[],[],'c1',[],[],[],[]);
m = pwAddX(m,'a11',1,'local',0.0000000001,[],[],'c1',[],[],[],[]);
m = pwAddX(m,'a12',1,'local',0.0000000001,[],[],'c1',[],[],[],[]);
m = pwAddX(m,'a13',1,'local',0.0000000001,[],[],'c1',[],[],[],[]);
m = pwAddX(m,'a14',1,'local',0.0000000001,[],[],'c1',[],[],[],[]);
m = pwAddX(m,'a15',1,'local',0.0000000001,[],[],'c1',[],[],[],[]);
m = pwAddX(m,'a16',1,'local',0.0000000001,[],[],'c1',[],[],[],[]);
m = pwAddX(m,'a17',1,'local',0.0000000001,[],[],'c1',[],[],[],[]);
m = pwAddX(m,'a18',1,'local',0.0000000001,[],[],'c1',[],[],[],[]);
m = pwAddX(m,'a19',1,'local',0.0000000001,[],[],'c1',[],[],[],[]);
m = pwAddX(m,'a20',1,'local',0.0000000001,[],[],'c1',[],[],[],[]);
m = pwAddX(m,'c1',1,'local',0.0000000001,[],[],'c1',[],[],[],[]);
m = pwAddX(m,'c2',1,'local',0.0000000001,[],[],'c1',[],[],[],[]);
m = pwAddX(m,'c3',1,'local',0.0000000001,[],[],'c1',[],[],[],[]);
m = pwAddX(m,'c4',1,'local',0.0000000001,[],[],'c1',[],[],[],[]);
m = pwAddX(m,'c5',1,'local',0.0000000001,[],[],'c1',[],[],[],[]);
m = pwAddX(m,'c6',1,'local',0.0000000001,[],[],'c1',[],[],[],[]);
m = pwAddX(m,'c7',1,'local',0.0000000001,[],[],'c1',[],[],[],[]);
m = pwAddX(m,'c8',1,'local',0.0000000001,[],[],'c1',[],[],[],[]);
m = pwAddX(m,'c9',1,'local',0.0000000001,[],[],'c1',[],[],[],[]);
m = pwAddX(m,'c10',1,'local',0.0000000001,[],[],'c1',[],[],[],[]);
m = pwAddX(m,'c11',1,'local',0.0000000001,[],[],'c1',[],[],[],[]);
m = pwAddX(m,'c12',1,'local',0.0000000001,[],[],'c1',[],[],[],[]);
m = pwAddX(m,'c13',1,'local',0.0000000001,[],[],'c1',[],[],[],[]);
m = pwAddX(m,'c14',1,'local',0.0000000001,[],[],'c1',[],[],[],[]);
m = pwAddX(m,'c15',1,'local',0.0000000001,[],[],'c1',[],[],[],[]);
m = pwAddX(m,'c16',1,'local',0.0000000001,[],[],'c1',[],[],[],[]);
m = pwAddX(m,'c17',1,'local',0.0000000001,[],[],'c1',[],[],[],[]);
m = pwAddX(m,'c18',1,'local',0.0000000001,[],[],'c1',[],[],[],[]);
m = pwAddX(m,'c19',1,'local',0.0000000001,[],[],'c1',[],[],[],[]);
m = pwAddX(m,'c20',1,'local',0.0000000001,[],[],'c1',[],[],[],[]);
m = pwAddX(m,'b',1,'local',0.0000000001,[],[],'c1',[],[],[],[]);

%% R: Reactions
% m = pwAddR(m, *ID, *reactants, *products, *modifiers, *type, *
    options, *rateSignature, *parameters, description, name, fast,
     compartments, parameterTrunks, designerPropsR, stoichiometry,
     reversible)
m = pwAddR(m,'R1',{'a1'},{'a20'},{},'A',[],[],{'Difussa'});
m = pwAddR(m,'R2',{'a1'},{'a2'},{},'A',[],[],{'Difussa'});
m = pwAddR(m,'R3',{'a20'},{'a19'},{},'A',[],[],{'Difussa'});
m = pwAddR(m,'R4',{'a20'},{'a1'},{},'A',[],[],{'Difussa'});
m = pwAddR(m,'R5',{'a2'},{'a3'},{},'A',[],[],{'Difussa'});
m = pwAddR(m,'R6',{'a2'},{'a1'},{},'A',[],[],{'Difussa'});
m = pwAddR(m,'R7',{'a3'},{'a4'},{},'A',[],[],{'Difussa'});
m = pwAddR(m,'R8',{'a3'},{'a2'},{},'A',[],[],{'Difussa'});
```

```
m = pwAddR(m,'R9',{'a4'},{'a5'},{},'A',[],[],{'Difussa'});
m = pwAddR(m,'R10',{'a4'},{'a3'},{},'A',[],[],{'Difussa'});
m = pwAddR(m,'R11',{'a5'},{'a6'},{},'A',[],[],{'Difussa'});
m = pwAddR(m,'R12',{'a5'},{'a4'},{},'A',[],[],{'Difussa'});
m = pwAddR(m,'R13',{'a6'},{'a7'},{},'A',[],[],{'Difussa'});
m = pwAddR(m,'R14',{'a6'},{'a5'},{},'A',[],[],{'Difussa'});
m = pwAddR(m,'R15',{'a7'},{'a8'},{},'A',[],[],{'Difussa'});
m = pwAddR(m,'R16',{'a7'},{'a6'},{},'A',[],[],{'Difussa'});
m = pwAddR(m,'R17',{'a8'},{'a9'},{},'A',[],[],{'Difussa'});
m = pwAddR(m,'R18',{'a8'},{'a7'},{},'A',[],[],{'Difussa'});
m = pwAddR(m,'R19',{'a9'},{'a10'},{},'A',[],[],{'Difussa'});
m = pwAddR(m,'R20',{'a9'},{'a8'},{},'A',[],[],{'Difussa'});
m = pwAddR(m,'R21',{'a10'},{'a11'},{},'A',[],[],{'Difussa'});
m = pwAddR(m,'R22',{'a10'},{'a9'},{},'A',[],[],{'Difussa'});
m = pwAddR(m,'R23',{'a11'},{'a12'},{},'A',[],[],{'Difussa'});
m = pwAddR(m,'R24',{'a11'},{'a10'},{},'A',[],[],{'Difussa'});
m = pwAddR(m,'R25',{'a12'},{'a13'},{},'A',[],[],{'Difussa'});
m = pwAddR(m,'R26',{'a12'},{'a11'},{},'A',[],[],{'Difussa'});
m = pwAddR(m,'R27',{'a13'},{'a14'},{},'A',[],[],{'Difussa'});
m = pwAddR(m,'R28',{'a13'},{'a12'},{},'A',[],[],{'Difussa'});
m = pwAddR(m,'R29',{'a14'},{'a15'},{},'A',[],[],{'Difussa'});
m = pwAddR(m,'R30',{'a14'},{'a13'},{},'A',[],[],{'Difussa'});
m = pwAddR(m,'R31',{'a15'},{'a16'},{},'A',[],[],{'Difussa'});
m = pwAddR(m,'R32',{'a15'},{'a14'},{},'A',[],[],{'Difussa'});
m = pwAddR(m,'R33',{'a16'},{'a17'},{},'A',[],[],{'Difussa'});
m = pwAddR(m,'R34',{'a16'},{'a15'},{},'A',[],[],{'Difussa'});
m = pwAddR(m,'R35',{'a17'},{'a18'},{},'A',[],[],{'Difussa'});
m = pwAddR(m,'R36',{'a17'},{'a16'},{},'A',[],[],{'Difussa'});
m = pwAddR(m,'R37',{'a18'},{'a19'},{},'A',[],[],{'Difussa'});
m = pwAddR(m,'R38',{'a18'},{'a17'},{},'A',[],[],{'Difussa'});
m = pwAddR(m,'R39',{'a19'},{'a20'},{},'A',[],[],{'Difussa'});
m = pwAddR(m,'R40',{'a19'},{'a18'},{},'A',[],[],{'Difussa'});
m = pwAddR(m,'R41',{'c1'},{'c20'},{},'A',[],[],{'Difussc'});
m = pwAddR(m,'R42',{'c1'},{'c2'},{},'A',[],[],{'Difussc'});
m = pwAddR(m,'R43',{'c20'},{'c19'},{},'A',[],[],{'Difussc'});
m = pwAddR(m,'R44',{'c20'},{'c1'},{},'A',[],[],{'Difussc'});
m = pwAddR(m,'R45',{'c2'},{'c3'},{},'A',[],[],{'Difussc'});
m = pwAddR(m,'R46',{'c2'},{'c1'},{},'A',[],[],{'Difussc'});
m = pwAddR(m,'R47',{'c3'},{'c4'},{},'A',[],[],{'Difussc'});
m = pwAddR(m,'R48',{'c3'},{'c2'},{},'A',[],[],{'Difussc'});
m = pwAddR(m,'R49',{'c4'},{'c5'},{},'A',[],[],{'Difussc'});
m = pwAddR(m,'R50',{'c4'},{'c3'},{},'A',[],[],{'Difussc'});
m = pwAddR(m,'R51',{'c5'},{'c6'},{},'A',[],[],{'Difussc'});
m = pwAddR(m,'R52',{'c5'},{'c4'},{},'A',[],[],{'Difussc'});
m = pwAddR(m,'R53',{'c6'},{'c7'},{},'A',[],[],{'Difussc'});
m = pwAddR(m,'R54',{'c6'},{'c5'},{},'A',[],[],{'Difussc'});
m = pwAddR(m,'R55',{'c7'},{'c8'},{},'A',[],[],{'Difussc'});
m = pwAddR(m,'R56',{'c7'},{'c6'},{},'A',[],[],{'Difussc'});
m = pwAddR(m,'R57',{'c8'},{'c9'},{},'A',[],[],{'Difussc'});
m = pwAddR(m,'R58',{'c8'},{'c7'},{},'A',[],[],{'Difussc'});
m = pwAddR(m,'R59',{'c9'},{'c10'},{},'A',[],[],{'Difussc'});
m = pwAddR(m,'R60',{'c9'},{'c8'},{},'A',[],[],{'Difussc'});
m = pwAddR(m,'R61',{'c10'},{'c11'},{},'A',[],[],{'Difussc'});
m = pwAddR(m,'R62',{'c10'},{'c9'},{},'A',[],[],{'Difussc'});
```

```
m = pwAddR(m,'R63',{'c11'},{'c12'},{},'A',[],[],{'Difussc'});
m = pwAddR(m,'R64',{'c11'},{'c10'},{},'A',[],[],{'Difussc'});
m = pwAddR(m,'R65',{'c12'},{'c13'},{},'A',[],[],{'Difussc'});
m = pwAddR(m,'R66',{'c12'},{'c11'},{},'A',[],[],{'Difussc'});
m = pwAddR(m,'R67',{'c13'},{'c14'},{},'A',[],[],{'Difussc'});
m = pwAddR(m,'R68',{'c13'},{'c12'},{},'A',[],[],{'Difussc'});
m = pwAddR(m,'R69',{'c14'},{'c15'},{},'A',[],[],{'Difussc'});
m = pwAddR(m,'R70',{'c14'},{'c13'},{},'A',[],[],{'Difussc'});
m = pwAddR(m,'R71',{'c15'},{'c16'},{},'A',[],[],{'Difussc'});
m = pwAddR(m,'R72',{'c15'},{'c14'},{},'A',[],[],{'Difussc'});
m = pwAddR(m,'R73',{'c16'},{'c17'},{},'A',[],[],{'Difussc'});
m = pwAddR(m,'R74',{'c16'},{'c15'},{},'A',[],[],{'Difussc'});
m = pwAddR(m,'R75',{'c17'},{'c18'},{},'A',[],[],{'Difussc'});
m = pwAddR(m,'R76',{'c17'},{'c16'},{},'A',[],[],{'Difussc'});
m = pwAddR(m,'R77',{'c18'},{'c19'},{},'A',[],[],{'Difussc'});
m = pwAddR(m,'R78',{'c18'},{'c17'},{},'A',[],[],{'Difussc'});
m = pwAddR(m,'R79',{'c19'},{'c20'},{},'A',[],[],{'Difussc'});
m = pwAddR(m,'R80',{'c19'},{'c18'},{},'A',[],[],{'Difussc'});
m = pwAddR(m,'R81',{'a1'},{},{},'A',[],[],{'ra'});
m = pwAddR(m,'R82',{'a2'},{},{},'A',[],[],{'ra'});
m = pwAddR(m,'R83',{'a3'},{},{},'A',[],[],{'ra'});
m = pwAddR(m,'R84',{'a4'},{},{},'A',[],[],{'ra'});
m = pwAddR(m,'R85',{'a5'},{},{},'A',[],[],{'ra'});
m = pwAddR(m,'R86',{'a6'},{},{},'A',[],[],{'ra'});
m = pwAddR(m,'R87',{'a7'},{},{},'A',[],[],{'ra'});
m = pwAddR(m,'R88',{'a8'},{},{},'A',[],[],{'ra'});
m = pwAddR(m,'R89',{'a9'},{},{},'A',[],[],{'ra'});
m = pwAddR(m,'R90',{'a10'},{},{},'A',[],[],{'ra'});
m = pwAddR(m,'R91',{'a11'},{},{},'A',[],[],{'ra'});
m = pwAddR(m,'R92',{'a12'},{},{},'A',[],[],{'ra'});
m = pwAddR(m,'R93',{'a13'},{},{},'A',[],[],{'ra'});
m = pwAddR(m,'R94',{'a14'},{},{},'A',[],[],{'ra'});
m = pwAddR(m,'R95',{'a15'},{},{},'A',[],[],{'ra'});
m = pwAddR(m,'R96',{'a16'},{},{},'A',[],[],{'ra'});
m = pwAddR(m,'R97',{'a17'},{},{},'A',[],[],{'ra'});
m = pwAddR(m,'R98',{'a18'},{},{},'A',[],[],{'ra'});
m = pwAddR(m,'R99',{'a19'},{},{},'A',[],[],{'ra'});
m = pwAddR(m,'R100',{'a20'},{},{},'A',[],[],{'ra'});
m = pwAddR(m,'R101',{'c1'},{},{},'A',[],[],{'rc'});
m = pwAddR(m,'R102',{'c2'},{},{},'A',[],[],{'rc'});
m = pwAddR(m,'R103',{'c3'},{},{},'A',[],[],{'rc'});
m = pwAddR(m,'R104',{'c4'},{},{},'A',[],[],{'rc'});
m = pwAddR(m,'R105',{'c5'},{},{},'A',[],[],{'rc'});
m = pwAddR(m,'R106',{'c6'},{},{},'A',[],[],{'rc'});
m = pwAddR(m,'R107',{'c7'},{},{},'A',[],[],{'rc'});
m = pwAddR(m,'R108',{'c8'},{},{},'A',[],[],{'rc'});
m = pwAddR(m,'R109',{'c9'},{},{},'A',[],[],{'rc'});
m = pwAddR(m,'R110',{'c10'},{},{},'A',[],[],{'rc'});
m = pwAddR(m,'R111',{'c11'},{},{},'A',[],[],{'rc'});
m = pwAddR(m,'R112',{'c12'},{},{},'A',[],[],{'rc'});
m = pwAddR(m,'R113',{'c13'},{},{},'A',[],[],{'rc'});
m = pwAddR(m,'R114',{'c14'},{},{},'A',[],[],{'rc'});
m = pwAddR(m,'R115',{'c15'},{},{},'A',[],[],{'rc'});
m = pwAddR(m,'R116',{'c16'},{},{},'A',[],[],{'rc'});
```

```
m = pwAddR(m,'R117',{'c17'},{},{},'A',[],[],{'rc'});
m = pwAddR(m,'R118',{'c18'},{},{},'A',[],[],{'rc'});
m = pwAddR(m,'R119',{'c19'},{},{},'A',[],[],{'rc'});
m = pwAddR(m,'R120',{'c20'},{},{},'A',[],[],{'rc'});
m = pwAddR(m,'R121',{'b'},{},{},'A',[],[],{'rb'});
m = pwAddR(m,'R122',{},{'c1'},{'a1'},'A',[],[],{'bc'});
m = pwAddR(m,'R123',{},{'c2'},{'a2'},'A',[],[],{'bc'});
m = pwAddR(m,'R124',{},{'c3'},{'a3'},'A',[],[],{'bc'});
m = pwAddR(m,'R125',{},{'c4'},{'a4'},'A',[],[],{'bc'});
m = pwAddR(m,'R126',{},{'c5'},{'a5'},'A',[],[],{'bc'});
m = pwAddR(m,'R127',{},{'c6'},{'a6'},'A',[],[],{'bc'});
m = pwAddR(m,'R128',{},{'c7'},{'a7'},'A',[],[],{'bc'});
m = pwAddR(m,'R129',{},{'c8'},{'a8'},'A',[],[],{'bc'});
m = pwAddR(m,'R130',{},{'c9'},{'a9'},'A',[],[],{'bc'});
m = pwAddR(m,'R131',{},{'c10'},{'a10'},'A',[],[],{'bc'});
m = pwAddR(m,'R132',{},{'c11'},{'a11'},'A',[],[],{'bc'});
m = pwAddR(m,'R133',{},{'c12'},{'a12'},'A',[],[],{'bc'});
m = pwAddR(m,'R134',{},{'c13'},{'a13'},'A',[],[],{'bc'});
m = pwAddR(m,'R135',{},{'c14'},{'a14'},'A',[],[],{'bc'});
m = pwAddR(m,'R136',{},{'c15'},{'a15'},'A',[],[],{'bc'});
m = pwAddR(m,'R137',{},{'c16'},{'a16'},'A',[],[],{'bc'});
m = pwAddR(m,'R138',{},{'c17'},{'a17'},'A',[],[],{'bc'});
m = pwAddR(m,'R139',{},{'c18'},{'a18'},'A',[],[],{'bc'});
m = pwAddR(m,'R140',{},{'c19'},{'a19'},'A',[],[],{'bc'});
m = pwAddR(m,'R141',{},{'c20'},{'a20'},'A',[],[],{'bc'});
m = pwAddR(m,'R142',{},{'b'},{'a1','a2','a3','a4','a5','a6','a7','
    a8','a9','a10','a11','a12','a13','a14','a15','a16','a17','a18'
    ,'a19','a20'},'C',[],'k1*(m1 + m2 + m3 + m4 + m5 + m6 + m7 +
    m8 + m9 + m10 + m11 + m12 + m13 + m14 + m15 + m16 + m17 + m18
    + m19 + m20)/20',{'rb'});
m = pwAddR(m,'R143',{},{'a1'},{'b','c1','S'},'C',[],'((1+k1
    *-0.98769*m3)*k5*(p1^2/m1 +k2))/((k3+m2)*(1+k4*p1^2))',{'dy','
    ba','sc','sa','ra'});
m = pwAddR(m,'R144',{},{'a2'},{'b','c2','S'},'C',[],'((1+k1
    *-0.89101*m3)*k5*(p1^2/m1 +k2))/((k3+m2)*(1+k4*p1^2))',{'dy','
    ba','sc','sa','ra'});
m = pwAddR(m,'R145',{},{'a3'},{'b','c3','S'},'C',[],'((1+k1
    *-0.70711*m3)*k5*(p1^2/m1 +k2))/((k3+m2)*(1+k4*p1^2))',{'dy','
    ba','sc','sa','ra'});
m = pwAddR(m,'R146',{},{'a4'},{'b','c4','S'},'C',[],'((1+k1
    *-0.45399*m3)*k5*(p1^2/m1 +k2))/((k3+m2)*(1+k4*p1^2))',{'dy','
    ba','sc','sa','ra'});
m = pwAddR(m,'R147',{},{'a5'},{'b','c5','S'},'C',[],'((1+k1
    *-0.15643*m3)*k5*(p1^2/m1 +k2))/((k3+m2)*(1+k4*p1^2))',{'dy','
    ba','sc','sa','ra'});
m = pwAddR(m,'R148',{},{'a6'},{'b','c6','S'},'C',[],'((1+k1
    *0.15643*m3)*k5*(p1^2/m1 +k2))/((k3+m2)*(1+k4*p1^2))',{'dy','
    ba','sc','sa','ra'});
m = pwAddR(m,'R149',{},{'a7'},{'b','c7','S'},'C',[],'((1+k1
    *0.45399*m3)*k5*(p1^2/m1 +k2))/((k3+m2)*(1+k4*p1^2))',{'dy','
    ba','sc','sa','ra'});
m = pwAddR(m,'R150',{},{'a8'},{'b','c8','S'},'C',[],'((1+k1
    *0.70711*m3)*k5*(p1^2/m1 +k2))/((k3+m2)*(1+k4*p1^2))',{'dy','
    ba','sc','sa','ra'});
```

```
m = pwAddR(m,'R151',{},{'a9'},{'b','c9','S'},'C',[],'((1+k1
    *0.89101*m3)*k5*(p1^2/m1 +k2))/((k3+m2)*(1+k4*p1^2))',{'dy','
    ba','sc','sa','ra'});
m = pwAddR(m,'R152',{},{'a10'},{'b','c10','S'},'C',[],'((1+k1
    *0.98769*m3)*k5*(p1^2/m1 +k2))/((k3+m2)*(1+k4*p1^2))',{'dy','
    ba','sc','sa','ra'});
m = pwAddR(m,'R153',{},{'a11'},{'b','c11','S'},'C',[],'((1+k1
    *0.98769*m3)*k5*(p1^2/m1 +k2))/((k3+m2)*(1+k4*p1^2))',{'dy','
    ba','sc','sa','ra'});
m = pwAddR(m,'R154',{},{'a12'},{'b','c12','S'},'C',[],'((1+k1
    *0.89101*m3)*k5*(p1^2/m1 +k2))/((k3+m2)*(1+k4*p1^2))',{'dy','
    ba','sc','sa','ra'});
m = pwAddR(m,'R155',{},{'a13'},{'b','c13','S'},'C',[],'((1+k1
    *0.70711*m3)*k5*(p1^2/m1 +k2))/((k3+m2)*(1+k4*p1^2))',{'dy','
    ba','sc','sa','ra'});
m = pwAddR(m,'R156',{},{'a14'},{'b','c14','S'},'C',[],'((1+k1
    *0.45399*m3)*k5*(p1^2/m1 +k2))/((k3+m2)*(1+k4*p1^2))',{'dy','
    ba','sc','sa','ra'});
m = pwAddR(m,'R157',{},{'a15'},{'b','c15','S'},'C',[],'((1+k1
    *0.15643*m3)*k5*(p1^2/m1 +k2))/((k3+m2)*(1+k4*p1^2))',{'dy','
    ba','sc','sa','ra'});
m = pwAddR(m,'R158',{},{'a16'},{'b','c16','S'},'C',[],'((1+k1
    *-0.15643*m3)*k5*(p1^2/m1 +k2))/((k3+m2)*(1+k4*p1^2))',{'dy','
    ba','sc','sa','ra'});
m = pwAddR(m,'R159',{},{'a17'},{'b','c17','S'},'C',[],'((1+k1
    *-0.45399*m3)*k5*(p1^2/m1 +k2))/((k3+m2)*(1+k4*p1^2))',{'dy','
    ba','sc','sa','ra'});
m = pwAddR(m,'R160',{},{'a18'},{'b','c18','S'},'C',[],'((1+k1
    *-0.70711*m3)*k5*(p1^2/m1 +k2))/((k3+m2)*(1+k4*p1^2))',{'dy','
    ba','sc','sa','ra'});
m = pwAddR(m,'R161',{},{'a19'},{'b','c19','S'},'C',[],'((1+k1
    *-0.89101*m3)*k5*(p1^2/m1 +k2))/((k3+m2)*(1+k4*p1^2))',{'dy','
    ba','sc','sa','ra'});
m = pwAddR(m,'R162',{},{'a20'},{'b','c20','S'},'C',[],'((1+k1
    *-0.98769*m3)*k5*(p1^2/m1 +k2))/((k3+m2)*(1+k4*p1^2))',{'dy','
    ba','sc','sa','ra'});

%% C: Compartments
% m = pwAddC(m, *ID, *size, outside, spatialDim, name, unit,
    constant, designerProps, classname, description)
m = pwAddC(m,'c1',1,[], [], [], [], [], [100 100 -0.75 160 160
    0.92156862745098 0.92156862745098 0.92156862745098 0 0 0 1],'
    compartment');

%% K: Dynamical parameters
% m = pwAddK(m, *ID, *value, fitSetting, minValue, maxValue, unit,
     name, description)
m = pwAddK(m,'Difussa',0.1,'global');
m = pwAddK(m,'Difussc',0.1,'global');
m = pwAddK(m,'ba',0.1,'global');
m = pwAddK(m,'bc',0.1,'global');
m = pwAddK(m,'ra',0.1,'global');
m = pwAddK(m,'rb',0.1,'global');
m = pwAddK(m,'rc',0.1,'global');
```

```
m = pwAddK(m,'sa',0.1,'global');
m = pwAddK(m,'sc',0.1,'global');
m = pwAddK(m,'dy',0.1,'local');

%% Driving Input
% m = pwAddU(m, *ID, *uType, *uTimes, *uValues, compartment, name,
     description, u2Values, alternativeIDs, designerProps,
    classname, referenceXID, unit, uFormula)
m = pwAddU(m,'S','steps',[-1000 0] ,[-1 1]);

%% Y: Observables
% m = pwAddY(m, *ID, *rhs, errorModelRhs, noiseType, unit, name,
    description, alternativeIDs, designerProps, classname)
m = pwAddY(m,'a1_obs','a1');
m = pwAddY(m,'a2_obs','a2');
m = pwAddY(m,'a3_obs','a3');
m = pwAddY(m,'a4_obs','a4');
m = pwAddY(m,'a5_obs','a5');
m = pwAddY(m,'a6_obs','a6');
m = pwAddY(m,'a7_obs','a7');
m = pwAddY(m,'a8_obs','a8');
m = pwAddY(m,'a9_obs','a9');
m = pwAddY(m,'a10_obs','a10');
m = pwAddY(m,'a11_obs','a11');
m = pwAddY(m,'a12_obs','a12');
m = pwAddY(m,'a13_obs','a13');
m = pwAddY(m,'a14_obs','a14');
m = pwAddY(m,'a15_obs','a15');
m = pwAddY(m,'a16_obs','a16');
m = pwAddY(m,'a17_obs','a17');
m = pwAddY(m,'a18_obs','a18');
m = pwAddY(m,'a19_obs','a19');
m = pwAddY(m,'a20_obs','a20');

%% Designer properties (do not modify)
m.designerPropsM = [1 1 1 0 0 0 400 250 600 400 0.30928668155038 1
     1 -208.311559834423 20 0 1 0 0];
```

```
% PottersWheel model definition file
function m = Levchenko_Model()

m              = pwGetEmptyModel();

%% Meta information
m.name = 'Levchenko_Model';
m.description = ' ';
m.authors     = {};
m.dates = {'2013-02-04'};
m.modelFormat = 3;

%% Default sampling time points
m.t = 0:3:120;
```

```
%% X: Dynamic variables
% m = pwAddX(m, *ID, *startValue, fitSetting, minValue, maxValue,
    unit, compartment, name, description, typeOfStartValue,
    designerProps, classname)
m = pwAddX(m,'R1',1,'local',0.0000000001,[],[],'c1',[],[],[],[]);
m = pwAddX(m,'R2',1,'local',0.0000000001,[],[],'c1',[],[],[],[]);
m = pwAddX(m,'R3',1,'local',0.0000000001,[],[],'c1',[],[],[],[]);
m = pwAddX(m,'R4',1,'local',0.0000000001,[],[],'c1',[],[],[],[]);
m = pwAddX(m,'R5',1,'local',0.0000000001,[],[],'c1',[],[],[],[]);
m = pwAddX(m,'R6',1,'local',0.0000000001,[],[],'c1',[],[],[],[]);
m = pwAddX(m,'R7',1,'local',0.0000000001,[],[],'c1',[],[],[],[]);
m = pwAddX(m,'R8',1,'local',0.0000000001,[],[],'c1',[],[],[],[]);
m = pwAddX(m,'R9',1,'local',0.0000000001,[],[],'c1',[],[],[],[]);
m = pwAddX(m,'R10',1,'local',0.0000000001,[],[],'c1',[],[],[],[]);
m = pwAddX(m,'R11',1,'local',0.0000000001,[],[],'c1',[],[],[],[]);
m = pwAddX(m,'R12',1,'local',0.0000000001,[],[],'c1',[],[],[],[]);
m = pwAddX(m,'R13',1,'local',0.0000000001,[],[],'c1',[],[],[],[]);
m = pwAddX(m,'R14',1,'local',0.0000000001,[],[],'c1',[],[],[],[]);
m = pwAddX(m,'R15',1,'local',0.0000000001,[],[],'c1',[],[],[],[]);
m = pwAddX(m,'R16',1,'local',0.0000000001,[],[],'c1',[],[],[],[]);
m = pwAddX(m,'R17',1,'local',0.0000000001,[],[],'c1',[],[],[],[]);
m = pwAddX(m,'R18',1,'local',0.0000000001,[],[],'c1',[],[],[],[]);
m = pwAddX(m,'R19',1,'local',0.0000000001,[],[],'c1',[],[],[],[]);
m = pwAddX(m,'R20',1,'local',0.0000000001,[],[],'c1',[],[],[],[]);
m = pwAddX(m,'A1',1,'local',0.0000000001,[],[],'c1',[],[],[],[]);
m = pwAddX(m,'A2',1,'local',0.0000000001,[],[],'c1',[],[],[],[]);
m = pwAddX(m,'A3',1,'local',0.0000000001,[],[],'c1',[],[],[],[]);
m = pwAddX(m,'A4',1,'local',0.0000000001,[],[],'c1',[],[],[],[]);
m = pwAddX(m,'A5',1,'local',0.0000000001,[],[],'c1',[],[],[],[]);
m = pwAddX(m,'A6',1,'local',0.0000000001,[],[],'c1',[],[],[],[]);
m = pwAddX(m,'A7',1,'local',0.0000000001,[],[],'c1',[],[],[],[]);
m = pwAddX(m,'A8',1,'local',0.0000000001,[],[],'c1',[],[],[],[]);
m = pwAddX(m,'A9',1,'local',0.0000000001,[],[],'c1',[],[],[],[]);
m = pwAddX(m,'A10',1,'local',0.0000000001,[],[],'c1',[],[],[],[]);
m = pwAddX(m,'A11',1,'local',0.0000000001,[],[],'c1',[],[],[],[]);
m = pwAddX(m,'A12',1,'local',0.0000000001,[],[],'c1',[],[],[],[]);
m = pwAddX(m,'A13',1,'local',0.0000000001,[],[],'c1',[],[],[],[]);
m = pwAddX(m,'A14',1,'local',0.0000000001,[],[],'c1',[],[],[],[]);
m = pwAddX(m,'A15',1,'local',0.0000000001,[],[],'c1',[],[],[],[]);
m = pwAddX(m,'A16',1,'local',0.0000000001,[],[],'c1',[],[],[],[]);
m = pwAddX(m,'A17',1,'local',0.0000000001,[],[],'c1',[],[],[],[]);
m = pwAddX(m,'A18',1,'local',0.0000000001,[],[],'c1',[],[],[],[]);
m = pwAddX(m,'A19',1,'local',0.0000000001,[],[],'c1',[],[],[],[]);
m = pwAddX(m,'A20',1,'local',0.0000000001,[],[],'c1',[],[],[],[]);
m = pwAddX(m,'I1',1,'local',0.0000000001,[],[],'c1',[],[],[],[]);
m = pwAddX(m,'I2',1,'local',0.0000000001,[],[],'c1',[],[],[],[]);
m = pwAddX(m,'I3',1,'local',0.0000000001,[],[],'c1',[],[],[],[]);
m = pwAddX(m,'I4',1,'local',0.0000000001,[],[],'c1',[],[],[],[]);
m = pwAddX(m,'I5',1,'local',0.0000000001,[],[],'c1',[],[],[],[]);
m = pwAddX(m,'I6',1,'local',0.0000000001,[],[],'c1',[],[],[],[]);
m = pwAddX(m,'I7',1,'local',0.0000000001,[],[],'c1',[],[],[],[]);
m = pwAddX(m,'I8',1,'local',0.0000000001,[],[],'c1',[],[],[],[]);
m = pwAddX(m,'I9',1,'local',0.0000000001,[],[],'c1',[],[],[],[]);
```

```
m = pwAddX(m,'I10',1,'local',0.0000000001,[],[],'c1',[],[],[],[]);
m = pwAddX(m,'I11',1,'local',0.0000000001,[],[],'c1',[],[],[],[]);
m = pwAddX(m,'I12',1,'local',0.0000000001,[],[],'c1',[],[],[],[]);
m = pwAddX(m,'I13',1,'local',0.0000000001,[],[],'c1',[],[],[],[]);
m = pwAddX(m,'I14',1,'local',0.0000000001,[],[],'c1',[],[],[],[]);
m = pwAddX(m,'I15',1,'local',0.0000000001,[],[],'c1',[],[],[],[]);
m = pwAddX(m,'I16',1,'local',0.0000000001,[],[],'c1',[],[],[],[]);
m = pwAddX(m,'I17',1,'local',0.0000000001,[],[],'c1',[],[],[],[]);
m = pwAddX(m,'I18',1,'local',0.0000000001,[],[],'c1',[],[],[],[]);
m = pwAddX(m,'I19',1,'local',0.0000000001,[],[],'c1',[],[],[],[]);
m = pwAddX(m,'I20',1,'local',0.0000000001,[],[],'c1',[],[],[],[]);

%% R: Reactions
% m = pwAddR(m, *ID, *reactants, *products, *modifiers, *type, *
    options, *rateSignature, *parameters, description, name, fast,
     compartments, parameterTrunks, designerPropsR, stoichiometry,
     reversible)
m = pwAddR(m,'R1',{'I1'},{'I20'},{},'A',[],[],{'DifussI'});
m = pwAddR(m,'R2',{'I1'},{'I2'},{},'A',[],[],{'DifussI'});
m = pwAddR(m,'R3',{'I20'},{'I19'},{},'A',[],[],{'DifussI'});
m = pwAddR(m,'R4',{'I20'},{'I1'},{},'A',[],[],{'DifussI'});
m = pwAddR(m,'R5',{'I2'},{'I3'},{},'A',[],[],{'DifussI'});
m = pwAddR(m,'R6',{'I2'},{'I1'},{},'A',[],[],{'DifussI'});
m = pwAddR(m,'R7',{'I3'},{'I4'},{},'A',[],[],{'DifussI'});
m = pwAddR(m,'R8',{'I3'},{'I2'},{},'A',[],[],{'DifussI'});
m = pwAddR(m,'R9',{'I4'},{'I5'},{},'A',[],[],{'DifussI'});
m = pwAddR(m,'R10',{'I4'},{'I3'},{},'A',[],[],{'DifussI'});
m = pwAddR(m,'R11',{'I5'},{'I6'},{},'A',[],[],{'DifussI'});
m = pwAddR(m,'R12',{'I5'},{'I4'},{},'A',[],[],{'DifussI'});
m = pwAddR(m,'R13',{'I6'},{'I7'},{},'A',[],[],{'DifussI'});
m = pwAddR(m,'R14',{'I6'},{'I5'},{},'A',[],[],{'DifussI'});
m = pwAddR(m,'R15',{'I7'},{'I8'},{},'A',[],[],{'DifussI'});
m = pwAddR(m,'R16',{'I7'},{'I6'},{},'A',[],[],{'DifussI'});
m = pwAddR(m,'R17',{'I8'},{'I9'},{},'A',[],[],{'DifussI'});
m = pwAddR(m,'R18',{'I8'},{'I7'},{},'A',[],[],{'DifussI'});
m = pwAddR(m,'R19',{'I9'},{'I10'},{},'A',[],[],{'DifussI'});
m = pwAddR(m,'R20',{'I9'},{'I8'},{},'A',[],[],{'DifussI'});
m = pwAddR(m,'R21',{'I10'},{'I11'},{},'A',[],[],{'DifussI'});
m = pwAddR(m,'R22',{'I10'},{'I9'},{},'A',[],[],{'DifussI'});
m = pwAddR(m,'R23',{'I11'},{'I12'},{},'A',[],[],{'DifussI'});
m = pwAddR(m,'R24',{'I11'},{'I10'},{},'A',[],[],{'DifussI'});
m = pwAddR(m,'R25',{'I12'},{'I13'},{},'A',[],[],{'DifussI'});
m = pwAddR(m,'R26',{'I12'},{'I11'},{},'A',[],[],{'DifussI'});
m = pwAddR(m,'R27',{'I13'},{'I14'},{},'A',[],[],{'DifussI'});
m = pwAddR(m,'R28',{'I13'},{'I12'},{},'A',[],[],{'DifussI'});
m = pwAddR(m,'R29',{'I14'},{'I15'},{},'A',[],[],{'DifussI'});
m = pwAddR(m,'R30',{'I14'},{'I13'},{},'A',[],[],{'DifussI'});
m = pwAddR(m,'R31',{'I15'},{'I16'},{},'A',[],[],{'DifussI'});
m = pwAddR(m,'R32',{'I15'},{'I14'},{},'A',[],[],{'DifussI'});
m = pwAddR(m,'R33',{'I16'},{'I17'},{},'A',[],[],{'DifussI'});
m = pwAddR(m,'R34',{'I16'},{'I15'},{},'A',[],[],{'DifussI'});
m = pwAddR(m,'R35',{'I17'},{'I18'},{},'A',[],[],{'DifussI'});
m = pwAddR(m,'R36',{'I17'},{'I16'},{},'A',[],[],{'DifussI'});
m = pwAddR(m,'R37',{'I18'},{'I19'},{},'A',[],[],{'DifussI'});
```

```
m = pwAddR(m,'R38',{'I18'},{'I17'},{},'A',[],[],{'DifussI'});
m = pwAddR(m,'R39',{'I19'},{'I20'},{},'A',[],[],{'DifussI'});
m = pwAddR(m,'R40',{'I19'},{'I18'},{},'A',[],[],{'DifussI'});
m = pwAddR(m,'R41',{'A1'},{},{},'A',[],[],{'K-A'});
m = pwAddR(m,'R42',{'A2'},{},{},'A',[],[],{'K-A'});
m = pwAddR(m,'R43',{'A3'},{},{},'A',[],[],{'K-A'});
m = pwAddR(m,'R44',{'A4'},{},{},'A',[],[],{'K-A'});
m = pwAddR(m,'R45',{'A5'},{},{},'A',[],[],{'K-A'});
m = pwAddR(m,'R46',{'A6'},{},{},'A',[],[],{'K-A'});
m = pwAddR(m,'R47',{'A7'},{},{},'A',[],[],{'K-A'});
m = pwAddR(m,'R48',{'A8'},{},{},'A',[],[],{'K-A'});
m = pwAddR(m,'R49',{'A9'},{},{},'A',[],[],{'K-A'});
m = pwAddR(m,'R50',{'A10'},{},{},'A',[],[],{'K-A'});
m = pwAddR(m,'R51',{'A11'},{},{},'A',[],[],{'K-A'});
m = pwAddR(m,'R52',{'A12'},{},{},'A',[],[],{'K-A'});
m = pwAddR(m,'R53',{'A13'},{},{},'A',[],[],{'K-A'});
m = pwAddR(m,'R54',{'A14'},{},{},'A',[],[],{'K-A'});
m = pwAddR(m,'R55',{'A15'},{},{},'A',[],[],{'K-A'});
m = pwAddR(m,'R56',{'A16'},{},{},'A',[],[],{'K-A'});
m = pwAddR(m,'R57',{'A17'},{},{},'A',[],[],{'K-A'});
m = pwAddR(m,'R58',{'A18'},{},{},'A',[],[],{'K-A'});
m = pwAddR(m,'R59',{'A19'},{},{},'A',[],[],{'K-A'});
m = pwAddR(m,'R60',{'A20'},{},{},'A',[],[],{'K-A'});
m = pwAddR(m,'R61',{},{'R1'},{'A1'},'C',[],'k1*m1*(k2-p1)',{'KR','
    RT'});
m = pwAddR(m,'R62',{},{'R2'},{'A2'},'C',[],'k1*m1*(k2-p1)',{'KR','
    RT'});
m = pwAddR(m,'R63',{},{'R3'},{'A3'},'C',[],'k1*m1*(k2-p1)',{'KR','
    RT'});
m = pwAddR(m,'R64',{},{'R4'},{'A4'},'C',[],'k1*m1*(k2-p1)',{'KR','
    RT'});
m = pwAddR(m,'R65',{},{'R5'},{'A5'},'C',[],'k1*m1*(k2-p1)',{'KR','
    RT'});
m = pwAddR(m,'R66',{},{'R6'},{'A6'},'C',[],'k1*m1*(k2-p1)',{'KR','
    RT'});
m = pwAddR(m,'R67',{},{'R7'},{'A7'},'C',[],'k1*m1*(k2-p1)',{'KR','
    RT'});
m = pwAddR(m,'R68',{},{'R8'},{'A8'},'C',[],'k1*m1*(k2-p1)',{'KR','
    RT'});
m = pwAddR(m,'R69',{},{'R9'},{'A9'},'C',[],'k1*m1*(k2-p1)',{'KR','
    RT'});
m = pwAddR(m,'R70',{},{'R10'},{'A10'},'C',[],'k1*m1*(k2-p1)',{'KR'
    ,'RT'});
m = pwAddR(m,'R71',{},{'R11'},{'A11'},'C',[],'k1*m1*(k2-p1)',{'KR'
    ,'RT'});
m = pwAddR(m,'R72',{},{'R12'},{'A12'},'C',[],'k1*m1*(k2-p1)',{'KR'
    ,'RT'});
m = pwAddR(m,'R73',{},{'R13'},{'A13'},'C',[],'k1*m1*(k2-p1)',{'KR'
    ,'RT'});
m = pwAddR(m,'R74',{},{'R14'},{'A14'},'C',[],'k1*m1*(k2-p1)',{'KR'
    ,'RT'});
m = pwAddR(m,'R75',{},{'R15'},{'A15'},'C',[],'k1*m1*(k2-p1)',{'KR'
    ,'RT'});
```

```
m = pwAddR(m,'R76',{},{'R16'},{'A16'},'C',[],'k1*m1*(k2-p1)',{'KR'
    ,'RT'});
m = pwAddR(m,'R77',{},{'R17'},{'A17'},'C',[],'k1*m1*(k2-p1)',{'KR'
    ,'RT'});
m = pwAddR(m,'R78',{},{'R18'},{'A18'},'C',[],'k1*m1*(k2-p1)',{'KR'
    ,'RT'});
m = pwAddR(m,'R79',{},{'R19'},{'A19'},'C',[],'k1*m1*(k2-p1)',{'KR'
    ,'RT'});
m = pwAddR(m,'R80',{},{'R20'},{'A20'},'C',[],'k1*m1*(k2-p1)',{'KR'
    ,'RT'});
m = pwAddR(m,'R81',{'R1'},{},{'I1'},'A',[],[],{'K-R'});
m = pwAddR(m,'R82',{'R2'},{},{'I2'},'A',[],[],{'K-R'});
m = pwAddR(m,'R83',{'R3'},{},{'I3'},'A',[],[],{'K-R'});
m = pwAddR(m,'R84',{'R4'},{},{'I4'},'A',[],[],{'K-R'});
m = pwAddR(m,'R85',{'R5'},{},{'I5'},'A',[],[],{'K-R'});
m = pwAddR(m,'R86',{'R6'},{},{'I6'},'A',[],[],{'K-R'});
m = pwAddR(m,'R87',{'R7'},{},{'I7'},'A',[],[],{'K-R'});
m = pwAddR(m,'R88',{'R8'},{},{'I8'},'A',[],[],{'K-R'});
m = pwAddR(m,'R89',{'R9'},{},{'I9'},'A',[],[],{'K-R'});
m = pwAddR(m,'R90',{'R10'},{},{'I10'},'A',[],[],{'K-R'});
m = pwAddR(m,'R91',{'R11'},{},{'I11'},'A',[],[],{'K-R'});
m = pwAddR(m,'R92',{'R12'},{},{'I12'},'A',[],[],{'K-R'});
m = pwAddR(m,'R93',{'R13'},{},{'I13'},'A',[],[],{'K-R'});
m = pwAddR(m,'R94',{'R14'},{},{'I14'},'A',[],[],{'K-R'});
m = pwAddR(m,'R95',{'R15'},{},{'I15'},'A',[],[],{'K-R'});
m = pwAddR(m,'R96',{'R16'},{},{'I16'},'A',[],[],{'K-R'});
m = pwAddR(m,'R97',{'R17'},{},{'I17'},'A',[],[],{'K-R'});
m = pwAddR(m,'R98',{'R18'},{},{'I18'},'A',[],[],{'K-R'});
m = pwAddR(m,'R99',{'R19'},{},{'I19'},'A',[],[],{'K-R'});
m = pwAddR(m,'R100',{'R20'},{},{'I20'},'A',[],[],{'K-R'});
m = pwAddR(m,'R101',{'I1'},{},{},'A',[],[],{'K-I'});
m = pwAddR(m,'R102',{'I2'},{},{},'A',[],[],{'K-I'});
m = pwAddR(m,'R103',{'I3'},{},{},'A',[],[],{'K-I'});
m = pwAddR(m,'R104',{'I4'},{},{},'A',[],[],{'K-I'});
m = pwAddR(m,'R105',{'I5'},{},{},'A',[],[],{'K-I'});
m = pwAddR(m,'R106',{'I6'},{},{},'A',[],[],{'K-I'});
m = pwAddR(m,'R107',{'I7'},{},{},'A',[],[],{'K-I'});
m = pwAddR(m,'R108',{'I8'},{},{},'A',[],[],{'K-I'});
m = pwAddR(m,'R109',{'I9'},{},{},'A',[],[],{'K-I'});
m = pwAddR(m,'R110',{'I10'},{},{},'A',[],[],{'K-I'});
m = pwAddR(m,'R111',{'I11'},{},{},'A',[],[],{'K-I'});
m = pwAddR(m,'R112',{'I12'},{},{},'A',[],[],{'K-I'});
m = pwAddR(m,'R113',{'I13'},{},{},'A',[],[],{'K-I'});
m = pwAddR(m,'R114',{'I14'},{},{},'A',[],[],{'K-I'});
m = pwAddR(m,'R115',{'I15'},{},{},'A',[],[],{'K-I'});
m = pwAddR(m,'R116',{'I16'},{},{},'A',[],[],{'K-I'});
m = pwAddR(m,'R117',{'I17'},{},{},'A',[],[],{'K-I'});
m = pwAddR(m,'R118',{'I18'},{},{},'A',[],[],{'K-I'});
m = pwAddR(m,'R119',{'I19'},{},{},'A',[],[],{'K-I'});
m = pwAddR(m,'R120',{'I20'},{},{},'A',[],[],{'K-I'});
m = pwAddR(m,'R121',{},{'A1'},{'S'},'C',[],'k1*k2*(1+k3*-0.98769*
    m1)',{'KA','ra','dy'});
m = pwAddR(m,'R122',{},{'A2'},{'S'},'C',[],'k1*k2*(1+k3*-0.89101*
    m1)',{'KA','ra','dy'});
```

```
m = pwAddR(m,'R123',{},{'A3'},{'S'},'C',[],'k1*k2*(1+k3*-0.70711*
    m1)',{'KA','ra','dy'});
m = pwAddR(m,'R124',{},{'A4'},{'S'},'C',[],'k1*k2*(1+k3*-0.45399*
    m1)',{'KA','ra','dy'});
m = pwAddR(m,'R125',{},{'A5'},{'S'},'C',[],'k1*k2*(1+k3*-0.15643*
    m1)',{'KA','ra','dy'});
m = pwAddR(m,'R126',{},{'A6'},{'S'},'C',[],'k1*k2*(1+k3*0.15643*m1
    )',{'KA','ra','dy'});
m = pwAddR(m,'R127',{},{'A7'},{'S'},'C',[],'k1*k2*(1+k3*0.45399*m1
    )',{'KA','ra','dy'});
m = pwAddR(m,'R128',{},{'A8'},{'S'},'C',[],'k1*k2*(1+k3*0.70711*m1
    )',{'KA','ra','dy'});
m = pwAddR(m,'R129',{},{'A9'},{'S'},'C',[],'k1*k2*(1+k3*0.89101*m1
    )',{'KA','ra','dy'});
m = pwAddR(m,'R130',{},{'A10'},{'S'},'C',[],'k1*k2*(1+k3*0.98769*
    m1)',{'KA','ra','dy'});
m = pwAddR(m,'R131',{},{'A11'},{'S'},'C',[],'k1*k2*(1+k3*0.98769*
    m1)',{'KA','ra','dy'});
m = pwAddR(m,'R132',{},{'A12'},{'S'},'C',[],'k1*k2*(1+k3*0.89101*
    m1)',{'KA','ra','dy'});
m = pwAddR(m,'R133',{},{'A13'},{'S'},'C',[],'k1*k2*(1+k3*0.70711*
    m1)',{'KA','ra','dy'});
m = pwAddR(m,'R134',{},{'A14'},{'S'},'C',[],'k1*k2*(1+k3*0.45399*
    m1)',{'KA','ra','dy'});
m = pwAddR(m,'R135',{},{'A15'},{'S'},'C',[],'k1*k2*(1+k3*0.15643*
    m1)',{'KA','ra','dy'});
m = pwAddR(m,'R136',{},{'A16'},{'S'},'C',[],'k1*k2*(1+k3*-0.15643*
    m1)',{'KA','ra','dy'});
m = pwAddR(m,'R137',{},{'A17'},{'S'},'C',[],'k1*k2*(1+k3*-0.45399*
    m1)',{'KA','ra','dy'});
m = pwAddR(m,'R138',{},{'A18'},{'S'},'C',[],'k1*k2*(1+k3*-0.70711*
    m1)',{'KA','ra','dy'});
m = pwAddR(m,'R139',{},{'A19'},{'S'},'C',[],'k1*k2*(1+k3*-0.89101*
    m1)',{'KA','ra','dy'});
m = pwAddR(m,'R140',{},{'A20'},{'S'},'C',[],'k1*k2*(1+k3*-0.98769*
    m1)',{'KA','ra','dy'});
m = pwAddR(m,'R141',{},{'I1'},{'S'},'C',[],'k1*k2*(1+k3*-0.98769*
    m1)',{'KI','ra','dy'});
m = pwAddR(m,'R142',{},{'I2'},{'S'},'C',[],'k1*k2*(1+k3*-0.89101*
    m1)',{'KI','ra','dy'});
m = pwAddR(m,'R143',{},{'I3'},{'S'},'C',[],'k1*k2*(1+k3*-0.70711*
    m1)',{'KI','ra','dy'});
m = pwAddR(m,'R144',{},{'I4'},{'S'},'C',[],'k1*k2*(1+k3*-0.45399*
    m1)',{'KI','ra','dy'});
m = pwAddR(m,'R145',{},{'I5'},{'S'},'C',[],'k1*k2*(1+k3*-0.15643*
    m1)',{'KI','ra','dy'});
m = pwAddR(m,'R146',{},{'I6'},{'S'},'C',[],'k1*k2*(1+k3*0.15643*m1
    )',{'KI','ra','dy'});
m = pwAddR(m,'R147',{},{'I7'},{'S'},'C',[],'k1*k2*(1+k3*0.45399*m1
    )',{'KI','ra','dy'});
m = pwAddR(m,'R148',{},{'I8'},{'S'},'C',[],'k1*k2*(1+k3*0.70711*m1
    )',{'KI','ra','dy'});
m = pwAddR(m,'R149',{},{'I9'},{'S'},'C',[],'k1*k2*(1+k3*0.89101*m1
    )',{'KI','ra','dy'});
```

```
m = pwAddR(m,'R150',{},{'I10'},{'S'},'C',[],'k1*k2*(1+k3*0.98769*
    m1)',{'KI','ra','dy'});
m = pwAddR(m,'R151',{},{'I11'},{'S'},'C',[],'k1*k2*(1+k3*0.98769*
    m1)',{'KI','ra','dy'});
m = pwAddR(m,'R152',{},{'I12'},{'S'},'C',[],'k1*k2*(1+k3*0.89101*
    m1)',{'KI','ra','dy'});
m = pwAddR(m,'R153',{},{'I13'},{'S'},'C',[],'k1*k2*(1+k3*0.70711*
    m1)',{'KI','ra','dy'});
m = pwAddR(m,'R154',{},{'I14'},{'S'},'C',[],'k1*k2*(1+k3*0.45399*
    m1)',{'KI','ra','dy'});
m = pwAddR(m,'R155',{},{'I15'},{'S'},'C',[],'k1*k2*(1+k3*0.15643*
    m1)',{'KI','ra','dy'});
m = pwAddR(m,'R156',{},{'I16'},{'S'},'C',[],'k1*k2*(1+k3*-0.15643*
    m1)',{'KI','ra','dy'});
m = pwAddR(m,'R157',{},{'I17'},{'S'},'C',[],'k1*k2*(1+k3*-0.45399*
    m1)',{'KI','ra','dy'});
m = pwAddR(m,'R158',{},{'I18'},{'S'},'C',[],'k1*k2*(1+k3*-0.70711*
    m1)',{'KI','ra','dy'});
m = pwAddR(m,'R159',{},{'I19'},{'S'},'C',[],'k1*k2*(1+k3*-0.89101*
    m1)',{'KI','ra','dy'});
m = pwAddR(m,'R160',{},{'I20'},{'S'},'C',[],'k1*k2*(1+k3*-0.98769*
    m1)',{'KI','ra','dy'});

%% C: Compartments
% m = pwAddC(m, *ID, *size, outside, spatialDim, name, unit,
    constant, designerProps, classname, description)
m = pwAddC(m,'c1',1,[], [], [], [], [], [100 100 -0.75 160 160
    0.92156862745098 0.92156862745098 0.92156862745098 0 0 0 1],'
    compartment');

%% K: Dynamical parameters
% m = pwAddK(m, *ID, *value, fitSetting, minValue, maxValue, unit,
     name, description)
m = pwAddK(m,'DifussI',0.1,'global');
m = pwAddK(m,'KA',0.1,'global');
m = pwAddK(m,'K-A',0.1,'global');
m = pwAddK(m,'KR',0.1,'global');
m = pwAddK(m,'K-R',0.1,'global');
m = pwAddK(m,'KI',0.1,'global');
m = pwAddK(m,'K-I',0.1,'global');
m = pwAddK(m,'ra',0.1,'global');
m = pwAddK(m,'RT',0.1,'global');
m = pwAddK(m,'dy',0.1,'local');

%% Driving Input
% m = pwAddU(m, *ID, *uType, *uTimes, *uValues, compartment, name,
     description, u2Values, alternativeIDs, designerProps,
    classname, referenceXID, unit, uFormula)
m = pwAddU(m,'S','steps',[-1000 0] ,[-1 1]);

%% Y: Observables
% m = pwAddY(m, *ID, *rhs, errorModelRhs, noiseType, unit, name,
    description, alternativeIDs, designerProps, classname)
m = pwAddY(m,'R1_obs','R1');
```

```
m = pwAddY(m,'R2_obs','R2');
m = pwAddY(m,'R3_obs','R3');
m = pwAddY(m,'R4_obs','R4');
m = pwAddY(m,'R5_obs','R5');
m = pwAddY(m,'R6_obs','R6');
m = pwAddY(m,'R7_obs','R7');
m = pwAddY(m,'R8_obs','R8');
m = pwAddY(m,'R9_obs','R9');
m = pwAddY(m,'R10_obs','R10');
m = pwAddY(m,'R11_obs','R11');
m = pwAddY(m,'R12_obs','R12');
m = pwAddY(m,'R13_obs','R13');
m = pwAddY(m,'R14_obs','R14');
m = pwAddY(m,'R15_obs','R15');
m = pwAddY(m,'R16_obs','R16');
m = pwAddY(m,'R17_obs','R17');
m = pwAddY(m,'R18_obs','R18');
m = pwAddY(m,'R19_obs','R19');
m = pwAddY(m,'R20_obs','R20');

%% Designer properties (do not modify)
m.designerPropsM = [1 1 1 0 0 0 400 250 600 400 0.30928668155038 1
     1 -208.311559834423 20 0 1 0 0];
```

```
% PottersWheel model definition file
function m = Otsuji_Model()

m              = pwGetEmptyModel();

%% Meta information
m.name = 'Otsuji_Model';
m.description = ' ';
m.authors      = {};
m.dates = {'2013-02-04'};
m.modelFormat = 3;

%% Default sampling time points
m.t = 0:3:120;

%% X: Dynamic variables
% m = pwAddX(m, *ID, *startValue, fitSetting, minValue, maxValue,
    unit, compartment, name, description, typeOfStartValue,
    designerProps, classname)
m = pwAddX(m,'u1',1,'local',0.0000000001,[],[],'c1',[],[],[],[]);
m = pwAddX(m,'u2',1,'local',0.0000000001,[],[],'c1',[],[],[],[]);
m = pwAddX(m,'u3',1,'local',0.0000000001,[],[],'c1',[],[],[],[]);
m = pwAddX(m,'u4',1,'local',0.0000000001,[],[],'c1',[],[],[],[]);
m = pwAddX(m,'u5',1,'local',0.0000000001,[],[],'c1',[],[],[],[]);
m = pwAddX(m,'u6',1,'local',0.0000000001,[],[],'c1',[],[],[],[]);
m = pwAddX(m,'u7',1,'local',0.0000000001,[],[],'c1',[],[],[],[]);
m = pwAddX(m,'u8',1,'local',0.0000000001,[],[],'c1',[],[],[],[]);
m = pwAddX(m,'u9',1,'local',0.0000000001,[],[],'c1',[],[],[],[]);
```

```
m = pwAddX(m,'u10',1,'local',0.0000000001,[],[],'c1',[],[],[],[]);
m = pwAddX(m,'u11',1,'local',0.0000000001,[],[],'c1',[],[],[],[]);
m = pwAddX(m,'u12',1,'local',0.0000000001,[],[],'c1',[],[],[],[]);
m = pwAddX(m,'u13',1,'local',0.0000000001,[],[],'c1',[],[],[],[]);
m = pwAddX(m,'u14',1,'local',0.0000000001,[],[],'c1',[],[],[],[]);
m = pwAddX(m,'u15',1,'local',0.0000000001,[],[],'c1',[],[],[],[]);
m = pwAddX(m,'u16',1,'local',0.0000000001,[],[],'c1',[],[],[],[]);
m = pwAddX(m,'u17',1,'local',0.0000000001,[],[],'c1',[],[],[],[]);
m = pwAddX(m,'u18',1,'local',0.0000000001,[],[],'c1',[],[],[],[]);
m = pwAddX(m,'u19',1,'local',0.0000000001,[],[],'c1',[],[],[],[]);
m = pwAddX(m,'u20',1,'local',0.0000000001,[],[],'c1',[],[],[],[]);
m = pwAddX(m,'v1',1,'local',0.0000000001,[],[],'c1',[],[],[],[]);
m = pwAddX(m,'v2',1,'local',0.0000000001,[],[],'c1',[],[],[],[]);
m = pwAddX(m,'v3',1,'local',0.0000000001,[],[],'c1',[],[],[],[]);
m = pwAddX(m,'v4',1,'local',0.0000000001,[],[],'c1',[],[],[],[]);
m = pwAddX(m,'v5',1,'local',0.0000000001,[],[],'c1',[],[],[],[]);
m = pwAddX(m,'v6',1,'local',0.0000000001,[],[],'c1',[],[],[],[]);
m = pwAddX(m,'v7',1,'local',0.0000000001,[],[],'c1',[],[],[],[]);
m = pwAddX(m,'v8',1,'local',0.0000000001,[],[],'c1',[],[],[],[]);
m = pwAddX(m,'v9',1,'local',0.0000000001,[],[],'c1',[],[],[],[]);
m = pwAddX(m,'v10',1,'local',0.0000000001,[],[],'c1',[],[],[],[]);
m = pwAddX(m,'v11',1,'local',0.0000000001,[],[],'c1',[],[],[],[]);
m = pwAddX(m,'v12',1,'local',0.0000000001,[],[],'c1',[],[],[],[]);
m = pwAddX(m,'v13',1,'local',0.0000000001,[],[],'c1',[],[],[],[]);
m = pwAddX(m,'v14',1,'local',0.0000000001,[],[],'c1',[],[],[],[]);
m = pwAddX(m,'v15',1,'local',0.0000000001,[],[],'c1',[],[],[],[]);
m = pwAddX(m,'v16',1,'local',0.0000000001,[],[],'c1',[],[],[],[]);
m = pwAddX(m,'v17',1,'local',0.0000000001,[],[],'c1',[],[],[],[]);
m = pwAddX(m,'v18',1,'local',0.0000000001,[],[],'c1',[],[],[],[]);
m = pwAddX(m,'v19',1,'local',0.0000000001,[],[],'c1',[],[],[],[]);
m = pwAddX(m,'v20',1,'local',0.0000000001,[],[],'c1',[],[],[],[]);

%% R: Reactions
% m = pwAddR(m, *ID, *reactants, *products, *modifiers, *type, *
    options, *rateSignature, *parameters, description, name, fast,
     compartments, parameterTrunks, designerPropsR, stoichiometry,
     reversible)
m = pwAddR(m,'R1',{'v1'},{'v20'},{},'A',[],[],{'Difussv'});
m = pwAddR(m,'R2',{'v1'},{'v2'},{},'A',[],[],{'Difussv'});
m = pwAddR(m,'R3',{'v20'},{'v19'},{},'A',[],[],{'Difussv'});
m = pwAddR(m,'R4',{'v20'},{'v1'},{},'A',[],[],{'Difussv'});
m = pwAddR(m,'R5',{'v2'},{'v3'},{},'A',[],[],{'Difussv'});
m = pwAddR(m,'R6',{'v2'},{'v1'},{},'A',[],[],{'Difussv'});
m = pwAddR(m,'R7',{'v3'},{'v4'},{},'A',[],[],{'Difussv'});
m = pwAddR(m,'R8',{'v3'},{'v2'},{},'A',[],[],{'Difussv'});
m = pwAddR(m,'R9',{'v4'},{'v5'},{},'A',[],[],{'Difussv'});
m = pwAddR(m,'R10',{'v4'},{'v3'},{},'A',[],[],{'Difussv'});
m = pwAddR(m,'R11',{'v5'},{'v6'},{},'A',[],[],{'Difussv'});
m = pwAddR(m,'R12',{'v5'},{'v4'},{},'A',[],[],{'Difussv'});
m = pwAddR(m,'R13',{'v6'},{'v7'},{},'A',[],[],{'Difussv'});
m = pwAddR(m,'R14',{'v6'},{'v5'},{},'A',[],[],{'Difussv'});
m = pwAddR(m,'R15',{'v7'},{'v8'},{},'A',[],[],{'Difussv'});
m = pwAddR(m,'R16',{'v7'},{'v6'},{},'A',[],[],{'Difussv'});
m = pwAddR(m,'R17',{'v8'},{'v9'},{},'A',[],[],{'Difussv'});
```

```
m = pwAddR(m,'R18',{'v8'},{'v7'},{},'A',[],[],{'Difussv'});
m = pwAddR(m,'R19',{'v9'},{'v10'},{},'A',[],[],{'Difussv'});
m = pwAddR(m,'R20',{'v9'},{'v8'},{},'A',[],[],{'Difussv'});
m = pwAddR(m,'R21',{'v10'},{'v11'},{},'A',[],[],{'Difussv'});
m = pwAddR(m,'R22',{'v10'},{'v9'},{},'A',[],[],{'Difussv'});
m = pwAddR(m,'R23',{'v11'},{'v12'},{},'A',[],[],{'Difussv'});
m = pwAddR(m,'R24',{'v11'},{'v10'},{},'A',[],[],{'Difussv'});
m = pwAddR(m,'R25',{'v12'},{'v13'},{},'A',[],[],{'Difussv'});
m = pwAddR(m,'R26',{'v12'},{'v11'},{},'A',[],[],{'Difussv'});
m = pwAddR(m,'R27',{'v13'},{'v14'},{},'A',[],[],{'Difussv'});
m = pwAddR(m,'R28',{'v13'},{'v12'},{},'A',[],[],{'Difussv'});
m = pwAddR(m,'R29',{'v14'},{'v15'},{},'A',[],[],{'Difussv'});
m = pwAddR(m,'R30',{'v14'},{'v13'},{},'A',[],[],{'Difussv'});
m = pwAddR(m,'R31',{'v15'},{'v16'},{},'A',[],[],{'Difussv'});
m = pwAddR(m,'R32',{'v15'},{'v14'},{},'A',[],[],{'Difussv'});
m = pwAddR(m,'R33',{'v16'},{'v17'},{},'A',[],[],{'Difussv'});
m = pwAddR(m,'R34',{'v16'},{'v15'},{},'A',[],[],{'Difussv'});
m = pwAddR(m,'R35',{'v17'},{'v18'},{},'A',[],[],{'Difussv'});
m = pwAddR(m,'R36',{'v17'},{'v16'},{},'A',[],[],{'Difussv'});
m = pwAddR(m,'R37',{'v18'},{'v19'},{},'A',[],[],{'Difussv'});
m = pwAddR(m,'R38',{'v18'},{'v17'},{},'A',[],[],{'Difussv'});
m = pwAddR(m,'R39',{'v19'},{'v20'},{},'A',[],[],{'Difussv'});
m = pwAddR(m,'R40',{'v19'},{'v18'},{},'A',[],[],{'Difussv'});
m = pwAddR(m,'R41',{'u1'},{'u20'},{},'A',[],[],{'Difussu'});
m = pwAddR(m,'R42',{'u1'},{'u2'},{},'A',[],[],{'Difussu'});
m = pwAddR(m,'R43',{'u20'},{'u19'},{},'A',[],[],{'Difussu'});
m = pwAddR(m,'R44',{'u20'},{'u1'},{},'A',[],[],{'Difussu'});
m = pwAddR(m,'R45',{'u2'},{'u3'},{},'A',[],[],{'Difussu'});
m = pwAddR(m,'R46',{'u2'},{'u1'},{},'A',[],[],{'Difussu'});
m = pwAddR(m,'R47',{'u3'},{'u4'},{},'A',[],[],{'Difussu'});
m = pwAddR(m,'R48',{'u3'},{'u2'},{},'A',[],[],{'Difussu'});
m = pwAddR(m,'R49',{'u4'},{'u5'},{},'A',[],[],{'Difussu'});
m = pwAddR(m,'R50',{'u4'},{'u3'},{},'A',[],[],{'Difussu'});
m = pwAddR(m,'R51',{'u5'},{'u6'},{},'A',[],[],{'Difussu'});
m = pwAddR(m,'R52',{'u5'},{'u4'},{},'A',[],[],{'Difussu'});
m = pwAddR(m,'R53',{'u6'},{'u7'},{},'A',[],[],{'Difussu'});
m = pwAddR(m,'R54',{'u6'},{'u5'},{},'A',[],[],{'Difussu'});
m = pwAddR(m,'R55',{'u7'},{'u8'},{},'A',[],[],{'Difussu'});
m = pwAddR(m,'R56',{'u7'},{'u6'},{},'A',[],[],{'Difussu'});
m = pwAddR(m,'R57',{'u8'},{'u9'},{},'A',[],[],{'Difussu'});
m = pwAddR(m,'R58',{'u8'},{'u7'},{},'A',[],[],{'Difussu'});
m = pwAddR(m,'R59',{'u9'},{'u10'},{},'A',[],[],{'Difussu'});
m = pwAddR(m,'R60',{'u9'},{'u8'},{},'A',[],[],{'Difussu'});
m = pwAddR(m,'R61',{'u10'},{'u11'},{},'A',[],[],{'Difussu'});
m = pwAddR(m,'R62',{'u10'},{'u9'},{},'A',[],[],{'Difussu'});
m = pwAddR(m,'R63',{'u11'},{'u12'},{},'A',[],[],{'Difussu'});
m = pwAddR(m,'R64',{'u11'},{'u10'},{},'A',[],[],{'Difussu'});
m = pwAddR(m,'R65',{'u12'},{'u13'},{},'A',[],[],{'Difussu'});
m = pwAddR(m,'R66',{'u12'},{'u11'},{},'A',[],[],{'Difussu'});
m = pwAddR(m,'R67',{'u13'},{'u14'},{},'A',[],[],{'Difussu'});
m = pwAddR(m,'R68',{'u13'},{'u12'},{},'A',[],[],{'Difussu'});
m = pwAddR(m,'R69',{'u14'},{'u15'},{},'A',[],[],{'Difussu'});
m = pwAddR(m,'R70',{'u14'},{'u13'},{},'A',[],[],{'Difussu'});
m = pwAddR(m,'R71',{'u15'},{'u16'},{},'A',[],[],{'Difussu'});
```

```
m = pwAddR(m,'R72',{'u15'},{'u14'},{},'A',[],[],{'Difussu'});
m = pwAddR(m,'R73',{'u16'},{'u17'},{},'A',[],[],{'Difussu'});
m = pwAddR(m,'R74',{'u16'},{'u15'},{},'A',[],[],{'Difussu'});
m = pwAddR(m,'R75',{'u17'},{'u18'},{},'A',[],[],{'Difussu'});
m = pwAddR(m,'R76',{'u17'},{'u16'},{},'A',[],[],{'Difussu'});
m = pwAddR(m,'R77',{'u18'},{'u19'},{},'A',[],[],{'Difussu'});
m = pwAddR(m,'R78',{'u18'},{'u17'},{},'A',[],[],{'Difussu'});
m = pwAddR(m,'R79',{'u19'},{'u20'},{},'A',[],[],{'Difussu'});
m = pwAddR(m,'R80',{'u19'},{'u18'},{},'A',[],[],{'Difussu'});
m = pwAddR(m,'R81',{'v1'},{'u1'},{},'A',[],[],{'a1'});
m = pwAddR(m,'R82',{'v2'},{'u2'},{},'A',[],[],{'a1'});
m = pwAddR(m,'R83',{'v3'},{'u3'},{},'A',[],[],{'a1'});
m = pwAddR(m,'R84',{'v4'},{'u4'},{},'A',[],[],{'a1'});
m = pwAddR(m,'R85',{'v5'},{'u5'},{},'A',[],[],{'a1'});
m = pwAddR(m,'R86',{'v6'},{'u6'},{},'A',[],[],{'a1'});
m = pwAddR(m,'R87',{'v7'},{'u7'},{},'A',[],[],{'a1'});
m = pwAddR(m,'R88',{'v8'},{'u8'},{},'A',[],[],{'a1'});
m = pwAddR(m,'R89',{'v9'},{'u9'},{},'A',[],[],{'a1'});
m = pwAddR(m,'R90',{'v10'},{'u10'},{},'A',[],[],{'a1'});
m = pwAddR(m,'R91',{'v11'},{'u11'},{},'A',[],[],{'a1'});
m = pwAddR(m,'R92',{'v12'},{'u12'},{},'A',[],[],{'a1'});
m = pwAddR(m,'R93',{'v13'},{'u13'},{},'A',[],[],{'a1'});
m = pwAddR(m,'R94',{'v14'},{'u14'},{},'A',[],[],{'a1'});
m = pwAddR(m,'R95',{'v15'},{'u15'},{},'A',[],[],{'a1'});
m = pwAddR(m,'R96',{'v16'},{'u16'},{},'A',[],[],{'a1'});
m = pwAddR(m,'R97',{'v17'},{'u17'},{},'A',[],[],{'a1'});
m = pwAddR(m,'R98',{'v18'},{'u18'},{},'A',[],[],{'a1'});
m = pwAddR(m,'R99',{'v19'},{'u19'},{},'A',[],[],{'a1'});
m = pwAddR(m,'R100',{'v20'},{'u20'},{},'A',[],[],{'a1'});
m = pwAddR(m,'R101',{'u1'},{'v1'},{'S'},'C',[],'k1*((r1+p1)/(k2*k3
    *(1+k4*m1*-0.98769)*(r1+p1)+1)^2)',{'a1','a2','ra','dy'});
m = pwAddR(m,'R102',{'u2'},{'v2'},{'S'},'C',[],'k1*((r1+p1)/(k2*k3
    *(1+k4*m1*-0.89101)*(r1+p1)+1)^2)',{'a1','a2','ra','dy'});
m = pwAddR(m,'R103',{'u3'},{'v3'},{'S'},'C',[],'k1*((r1+p1)/(k2*k3
    *(1+k4*m1*-0.70711)*(r1+p1)+1)^2)',{'a1','a2','ra','dy'});
m = pwAddR(m,'R104',{'u4'},{'v4'},{'S'},'C',[],'k1*((r1+p1)/(k2*k3
    *(1+k4*m1*-0.45399)*(r1+p1)+1)^2)',{'a1','a2','ra','dy'});
m = pwAddR(m,'R105',{'u5'},{'v5'},{'S'},'C',[],'k1*((r1+p1)/(k2*k3
    *(1+k4*m1*-0.15643)*(r1+p1)+1)^2)',{'a1','a2','ra','dy'});
m = pwAddR(m,'R106',{'u6'},{'v6'},{'S'},'C',[],'k1*((r1+p1)/(k2*k3
    *(1+k4*m1*0.15643)*(r1+p1)+1)^2)',{'a1','a2','ra','dy'});
m = pwAddR(m,'R107',{'u7'},{'v7'},{'S'},'C',[],'k1*((r1+p1)/(k2*k3
    *(1+k4*m1*0.45399)*(r1+p1)+1)^2)',{'a1','a2','ra','dy'});
m = pwAddR(m,'R108',{'u8'},{'v8'},{'S'},'C',[],'k1*((r1+p1)/(k2*k3
    *(1+k4*m1*0.70711)*(r1+p1)+1)^2)',{'a1','a2','ra','dy'});
m = pwAddR(m,'R109',{'u9'},{'v9'},{'S'},'C',[],'k1*((r1+p1)/(k2*k3
    *(1+k4*m1*0.89101)*(r1+p1)+1)^2)',{'a1','a2','ra','dy'});
m = pwAddR(m,'R110',{'u10'},{'v10'},{'S'},'C',[],'k1*((r1+p1)/(k2*
    k3*(1+k4*m1*0.98769)*(r1+p1)+1)^2)',{'a1','a2','ra','dy'});
m = pwAddR(m,'R111',{'u11'},{'v11'},{'S'},'C',[],'k1*((r1+p1)/(k2*
    k3*(1+k4*m1*0.98769)*(r1+p1)+1)^2)',{'a1','a2','ra','dy'});
m = pwAddR(m,'R112',{'u12'},{'v12'},{'S'},'C',[],'k1*((r1+p1)/(k2*
    k3*(1+k4*m1*0.89101)*(r1+p1)+1)^2)',{'a1','a2','ra','dy'});
```

```
m = pwAddR(m,'R113',{'u13'},{'v13'},{'S'},'C',[],'k1*((r1+p1)/(k2*
    k3*(1+k4*m1*0.70711)*(r1+p1)+1)^2)',{'a1','a2','ra','dy'});
m = pwAddR(m,'R114',{'u14'},{'v14'},{'S'},'C',[],'k1*((r1+p1)/(k2*
    k3*(1+k4*m1*0.45399)*(r1+p1)+1)^2)',{'a1','a2','ra','dy'});
m = pwAddR(m,'R115',{'u15'},{'v15'},{'S'},'C',[],'k1*((r1+p1)/(k2*
    k3*(1+k4*m1*0.15643)*(r1+p1)+1)^2)',{'a1','a2','ra','dy'});
m = pwAddR(m,'R116',{'u16'},{'v16'},{'S'},'C',[],'k1*((r1+p1)/(k2*
    k3*(1+k4*m1*-0.15643)*(r1+p1)+1)^2)',{'a1','a2','ra','dy'});
m = pwAddR(m,'R117',{'u17'},{'v17'},{'S'},'C',[],'k1*((r1+p1)/(k2*
    k3*(1+k4*m1*-0.45399)*(r1+p1)+1)^2)',{'a1','a2','ra','dy'});
m = pwAddR(m,'R118',{'u18'},{'v18'},{'S'},'C',[],'k1*((r1+p1)/(k2*
    k3*(1+k4*m1*-0.70711)*(r1+p1)+1)^2)',{'a1','a2','ra','dy'});
m = pwAddR(m,'R119',{'u19'},{'v19'},{'S'},'C',[],'k1*((r1+p1)/(k2*
    k3*(1+k4*m1*-0.89101)*(r1+p1)+1)^2)',{'a1','a2','ra','dy'});
m = pwAddR(m,'R120',{'u20'},{'v20'},{'S'},'C',[],'k1*((r1+p1)/(k2*
    k3*(1+k4*m1*-0.98769)*(r1+p1)+1)^2)',{'a1','a2','ra','dy'});

%% C: Compartments
% m = pwAddC(m, *ID, *size, outside, spatialDim, name, unit,
    constant, designerProps, classname, description)
m = pwAddC(m,'c1',1,[], [], [], [], [], [100 100 -0.75 160 160
    0.92156862745098 0.92156862745098 0.92156862745098 0 0 0 1],'
    compartment');

%% K: Dynamical parameters
% m = pwAddK(m, *ID, *value, fitSetting, minValue, maxValue, unit,
     name, description)
m = pwAddK(m,'Difussu',0.1,'global');
m = pwAddK(m,'Difussv',0.1,'global');
m = pwAddK(m,'a1',0.1,'global');
m = pwAddK(m,'a2',0.1,'global');
m = pwAddK(m,'ra',0.1,'global');
m = pwAddK(m,'dy',0.1,'local');

%% Driving Input
% m = pwAddU(m, *ID, *uType, *uTimes, *uValues, compartment, name,
     description, u2Values, alternativeIDs, designerProps,
    classname, referenceXID, unit, uFormula)
m = pwAddU(m,'S','steps',[-1000 0] ,[-1 1]);

%% Y: Observables
% m = pwAddY(m, *ID, *rhs, errorModelRhs, noiseType, unit, name,
    description, alternativeIDs, designerProps, classname)
m = pwAddY(m,'u1_obs','u1');
m = pwAddY(m,'u2_obs','u2');
m = pwAddY(m,'u3_obs','u3');
m = pwAddY(m,'u4_obs','u4');
m = pwAddY(m,'u5_obs','u5');
m = pwAddY(m,'u6_obs','u6');
m = pwAddY(m,'u7_obs','u7');
m = pwAddY(m,'u8_obs','u8');
m = pwAddY(m,'u9_obs','u9');
m = pwAddY(m,'u10_obs','u10');
m = pwAddY(m,'u11_obs','u11');
```

```
m = pwAddY(m,'u12_obs','u12');
m = pwAddY(m,'u13_obs','u13');
m = pwAddY(m,'u14_obs','u14');
m = pwAddY(m,'u15_obs','u15');
m = pwAddY(m,'u16_obs','u16');
m = pwAddY(m,'u17_obs','u17');
m = pwAddY(m,'u18_obs','u18');
m = pwAddY(m,'u19_obs','u19');
m = pwAddY(m,'u20_obs','u20');


%% Designer properties (do not modify)
m.designerPropsM = [1 1 1 0 0 0 400 250 600 400 0.30928668155038 1
     1 -208.311559834423 20 0 1 0 0];
```

C. PUBLICATION

Lockley R, Ladds G, Bretschneider T. (2015) 'Image based validation of dynamical models for cell reorientation.', *Cytometry A.* **87**, 471-80

Cytometry
PART A
Journal of the International Society for Advancement of Cytometry

Image Based Validation of Dynamical Models for Cell Reorientation

Robert Lockley,[1] Graham Ladds,[2] Till Bretschneider[1]*

[1]Warwick Systems Biology Centre, Senate House, University of Warwick, Coventry, CV4 7AL, United Kingdom

[2]Division of Biomedical Cell Biology, Warwick Medical School, University of Warwick, Coventry, CV4 7AL, United Kingdom

Received 15 June 2014; Revised 2 October 2014; Accepted 6 November 2014

Grant sponsor: EPSRC through the Warwick Systems Biology Doctoral Training Centre; Grant sponsor: BBSRC; Grant number: BB/G01227X/1; Grant sponsor: Birmingham Science City Research Alliance; Grant sponsor: Wellcome Trust; Grant number: WT094131MA; Grant sponsor: Royal Society Research Grant.

Additional Supporting Information may be found in the online version of this article.

*Correspondence to: Till Bretschneider, Warwick Systems Biology Centre, Senate House, University of Warwick, Coventry, CV4 7AL, United Kingdom.
E-mail: T.Bretschneider@warwick.ac.uk

Published online 4 December 2014 in Wiley Online Library (wileyonlinelibrary.com)

DOI: 10.1002/cyto.a.22600

Abstract

A key feature of directed cell movement is the ability of cells to reorient quickly in response to changes in the direction of an extracellular stimulus. Mathematical models have suggested quite different regulatory mechanisms to explain reorientation, raising the question of how we can validate these models in a rigorous way. In this study, we fit three reaction–diffusion models to experimental data of *Dictyostelium* amoebae reorienting in response to alternating gradients of mechanical shear flow. The experimental readouts we use to fit are spatio-temporal distributions of a fluorescent reporter for cortical F-actin labeling the cell front. Experiments performed under different conditions are fitted simultaneously to challenge the models with different types of cellular dynamics. Although the model proposed by Otsuji is unable to provide a satisfactory fit, those suggested by Meinhardt and Levchenko fit equally well. Further, we show that reduction of the three-variable Meinhardt model to a two-variable model also provides an excellent fit, but has the advantage of all parameters being uniquely identifiable. Our work demonstrates that model selection and identifiability analysis, commonly applied to temporal dynamics problems in systems biology, can be a powerful tool when extended to spatio-temporal imaging data. © 2014 The Authors. Published by Wiley Periodicals, Inc.

Key terms

cell reorientation; *Dictyostelium*; actin; image based model fitting; spatio-temporal pattern formation; fluorescence microscopy; identifiability analysis

DIRECTED cell motion is based on three functional modules (i) the formation of cellular protrusions driven by polymerization of actin, (ii) a mechanism to sense extracellular signals, for example, a gradient of chemoattractant, and direct protrusions to the cell front, and (iii) polarization, which is the establishment of a front-rear axis, whereby myosin-II mediates retraction of the cell rear (1–3). The modular design of cell motility has resulted in it becoming a paradigm of systems biology. In particular, how these modules are integrated to allow cells to navigate in rapidly changing environments has become a focus of theoretical and computational research.

Most models employ a Turing-like (4) local-excitation global-inhibition mechanism, whereby the stronger stimulation of the up-gradient cell end results in local autocatalytic activation of the cell front. At the same time, a fast propagating inhibitory mechanism renders the cell rear unresponsive to stimulation. The theory of reaction–diffusion models is well established and Meinhardt first implemented a model for cell reorientation on a circular domain to study how cells could regain sensitivity at the rear and thus are able to respond to changes in direction of a signaling gradient (5). Most recently, several groups have coupled the Meinhardt model with biophysical models of deformable contours to simulate the deformation and movement of cells in response to a signal gradient (6–8). Other models have been proposed to address specific questions of signal amplification, sensitivity, and adaptation (9–13).

Here, we want to compare three representative models for cell reorientation, each of which employs a different regulatory mechanism. The original model by Meinhardt (5), a model by Levchenko and Iglesias (13), and one by Otsuji et al. (12). We are more focused on the problem of model selection, so for their internal workings and their derivation, we refer the reader to an excellent review by Jilkine and Edlestein-Keshet which discusses, among others, all three models in detail (11).

In brief, the Levchenko model has been engineered to achieve perfect adaptation to spatially uniform stimuli, which result in a transient response only, before a new steady-state is achieved. In a gradient, persistent stimulation of a cell front is possible, without the need to temporarily break-down the pattern as in the Meinhardt model. The rationale behind the model by Otsuji et al. (12) is that many signaling components involved in gradient sensing, such as small GTPases of the Rho family are known to exist in an either active or inactive state. Whereas in the models by Meinhardt and Levchenko an increase in signal always causes a stronger response, mass conservation in the Otsuji model takes into account that the total amount of signaling molecules is limited. Specific features of this model are the formation of a strong unique axis of cell polarization and an increased sensitivity at the cell front. The motivation for selecting these models was simply to investigate how more modern models compare to their ancestor, the Meinhardt model. As we wanted to use the same fitting approach for each model we limited ourselves to continuum reaction–diffusion equations, all of which, however, display quite distinct features in their behavior.

In all three models, some of the regulatory mechanisms can be loosely mapped to known biochemical signaling pathways, but all employ a minimal set of regulatory feedback loops, and therefore have a comparatively small number of parameters. This is an important requirement in terms of quantitative modeling that prevents over-fitting and enables selection of structurally identifiable models with unique solutions (14).

Here, we build on our previous work on quantifying actin dynamics in the cortex of moving cells using active contour based methods for cell segmentation and tracking (15–17). Using fluorescent reporters for polymerized actin as a proxy for cell front activation, we ask: (i) Can we validate different reaction–diffusion models by directly fitting models to time series image data of moving cells? (ii) Will we be able to identify unique sets of parameters?

Materials And Methods

General Laboratory Reagents

HL5 growth media containing 75 mM glucose was obtained from ForMedium™ (Hunstanton, UK). All other general reagents were purchased from Sigma-Aldrich (St Louis, MO) unless stated.

Experimental Data. The experimental data are fluorescence distributions of a reporter for F-actin (LimEΔ-GFP) in the cortex of *Dictyostelium* (JH10) cells reorienting in alternating gradients of shear flow as described in (18). Previously, we have shown that the response to shear stress is very similar to that toward a chemoattractant with cells producing a front against the flow. Cells were segmented and tracked using QuimP software [http://go.warwick.ac.uk] (15,19) and fluorescence sampled at 20 equidistant points along the cell cortex. All fluorescence data presented are normalized by dividing through the mean fluorescence in the cell body to account for differences in expression levels, fluctuations in laser intensity and bleaching. Details on microscopy are described in Dalous et al. (18).

Random Motility Experiments. Wild-type *Dictyostelium* (AX2) cells expressing LimEΔ-RFP were cultured at room temperature in HL5 media containing 75 mM glucose with appropriate antibiotics. Cells were washed twice with KK2 buffer and transferred to glass-bottomed imaging culture plates (Fisher Scientific UK, Loughborough, UK). Actin was visualized using a Personal DeltaVision microscope (Applied Precision, Issaquah, WA) comprising an Olympus UPlanSApo 100×, NA 1.4, oil immersion objective and a Photometric CoolSNAP HQ camera (Roper Scientific, Martinsried, Germany). Captured images were processed by iterative constrained deconvolution using SoftWoRx (Applied Precession) and analyzed using ImageJ (20).

Long Duration Flow Experiments

Wild-type *Dictyostelium* (AX2) cells expressing ABP120-GFP as a marker for F-actin were cultured in HL5 media containing 75 mM glucose. Cells were washed with KK2 and after 1 h in shaking culture seeded into flow chambers (L × W × H $50 \times 5 \times 0.2$ mm^3), with flow of buffer driven by an air pressure pump system (IB-10902, Ibidi, Martinsried, Germany). A 1 Pa shear flow was applied for 600 s, followed by a 120 s period of no flow. This cycle was repeated once. ABP120-GFP was imaged using a True Confocal Scanner Leica TCS SP5 microscope (Leica Microsystems, Milton Keynes, UK).

Model Fitting

Model fitting and analysis were performed in PottersWheel (21), a Matlab toolbox that offers advanced tools for identifiability analyses. The spatial reaction–diffusion models under investigation are systems of coupled, partial differential equations (PDE) with two or three variables. Using a finite difference approximation of the diffusion operator $\partial^2 C/\partial x^2 \approx (C_{i-1} - 2C_i + C_{i+1})/(\Delta x)^2$, where C_i, C_{i-1} and C_{i+1} denote fluorescence intensities at point i and to the left and right of it, with $1 \leq i \leq N$, and $N = 20$ being the number of grid points, Δx the physical spacing between them, the system of PDEs can be transformed into a system of $N \times V$ coupled ordinary differential equations (ODEs), V being the number of variables. The problem is solved on a circular 1D domain with periodic boundary conditions by letting $C_0 = C_N$ and $C_{N+1} = C_1$.

When exposed to shear flow cells are aligned with the flow and do not exhibit much variation in shape. We therefore use, for simplicity, an equidistant spacing of fluorescence samples so that Δx is constant. In principle, our approach could

158

be adapted to sampling at arbitrary positions, then requiring interpolation between intensity values at previous time points.

We simulate a spatial profile of shear flow input (source term) using $s=(dy\cos(2\pi(n-1)/N))$ where dy is initially treated as a free parameter which describes the strength of the signal. Later, dy is replaced by an explicit polynomial function $dy(P)$ in terms of the absolute shear stress P. Node $i=n$ denotes the up-gradient position on the cell cortex. In the absence of a signal dy is set to zero.

Parameters are fitted by nonlinear least-square minimization using PottersWheel's built-in Trust Region optimization, fitting in logarithmic parameter space (22,23). To avoid getting caught in local minima, models were fitted 10–25 times from different starting points. Where indicated, we fitted to different experimental conditions simultaneously, obtaining a combined χ^2 value.

Parameter Profile Likelihood Estimation

To determine the sensitivity and identifiability of parameters, we used PottersWheel's parameter profile likelihood estimation (PLE) tool (24). By iteratively varying a parameter p_i about its optimum value and refitting the remaining parameters a χ^2 profile of the likelihood for p_i can be generated. Where this profile crosses a threshold, $\chi^2(\alpha, df)$, lower or upper limits for the confidence interval of p_i can be found, here at level $\alpha=68\%$. If both limits exist, the parameter is considered identifiable. A value of $df=1$ yields point-wise confidence intervals, whereas for simultaneous confidence intervals, df equals the number of parameters. The latter is used to determine identifiability.

Results

Our goal is to validate commonly used reaction–diffusion models for cell reorientation by fitting them to time-series image data of cells under well-controlled experimental conditions. The reaction networks of the different models under investigation are depicted in Figure 1A with S denoting the extracellular signal (experimentally we use a gradient of shear flow (18)). Meinhardt's model is based on one autocatalytic activator, A, that produces two inhibitors, B and C (5). The second inhibitor, C, was proposed as an extension to a two-variable model, consisting of only A and B, in order to achieve permanent sensitivity. In the Levchenko model, S promotes simultaneous production of activator A and inhibitor I, which act on a response element R (13). The Otsuji model considers mass conservation of a signaling component, which can be either in an activated form, U, or inactivated, V, whereby S promotes formation of U (12).

Ultimately, activation of a cell front in response to an extracellular stimulus results in formation of a F-actin rich protrusion, which is why we consider F-actin as a reliable readout for front activation. The *Dictyostelium* cell shown in Figure 1B responds toward shear flow of 2.1 Pa, with the F-actin label clearly marking the front facing the flow. Shear flow as signal input can be easily reversed, and the cell can be seen to reorient after changing the flow direction at $t = 0$ s. The old front is rapidly degraded, while the new front facing the flow appears at ~40 s after flow reversal.

Space-time plots of the cortical fluorescence sampled at 20 nodes allow capturing the entire dynamics in one plot (Fig. 1C). Normalizing the data with respect to the cell circumference has the advantage that data of multiple cells can be averaged, after synchronizing sequences with respect to the time of flow reversal. As illustrated in Figure 1D the population mean of $N = 14$ cells responding to 18 flow reversals, provides a clearer indication of F-actin disassembly and reassembly when compared to noisy single cell data. Later, we show that it is possible to fit single cell data, but for our initial model fitting we proceed with population averages. Fitting to single cell data can become computationally demanding when fitting to many cells simultaneously. Figure 1E gives an example of how the fluorescence profile of the averaged cell data along the normalized cell outline is fitted for selected time points using Meinhardt's model. The fitting procedure starts with the flow reversal at $t = 0$ s (For details on fitting see Materials and Methods).

The Meinhardt and Levchenko Model Both Fit the Shear-Flow Reorientation Data Well

Having demonstrated how we extract experimental data in form of spatio-temporal maps of F-actin fluorescence and fit them to dynamical models we proceed to compare how each of the three different models could fit to three experimental conditions: reorientation of cells in response to high shear stress of 2.1 Pa; to low shear stress (0.9 Pa); and flow/no-flow experiments where cells were first oriented under 2.1 Pa, with the flow subsequently being switched off resulting in slow depolarization of cells. These values were chosen since below 0.9 Pa cells respond by making U-turns instead of reversing their orientation and above 2.1 Pa they have difficulties remaining attached to the substratum. We fitted the data using the entire spatial fluorescence profile as shown in Figure 1E, but we summarize the data (Fig. 2) by only plotting the mean fluorescence of the two cell halves (up-gradient and down-gradient). Parameter values and initial conditions are given in Supporting Information Tables S1 and S2. It is apparent that disassembly of F-actin at the old front follows a simple exponential decay under 2.1 and 0.9 Pa with half-lives of $T_{1/2} = 38$ s and 59 s, respectively; assembly of F-actin at the new front is faster under low shear stress of 0.9 Pa where it plateaus after 60 s (Fig. 2). Under the shear stress of 2.1 Pa there is a marked delay of about 30 s before actin polymerization begins leveling around 3 min. The flow/no-flow experiments show slow loss of orientation on the timescale of minutes, but initially there is a slight increase in F-actin after removal of the stimulus. Thus shear flow clearly promotes F-actin assembly, but interestingly, at the same time, a higher shear stress slows F-actin assembly. This could be either due to increased mechanical load on the F-actin network at higher shear stresses, or negative feedback in the biochemical signal transduction pathway.

Shear flow affects the time-scales of loss and gain of fluorescence in intricate ways. Initially, we avoided dealing with absolute values of shear stresses as signal input, and let the

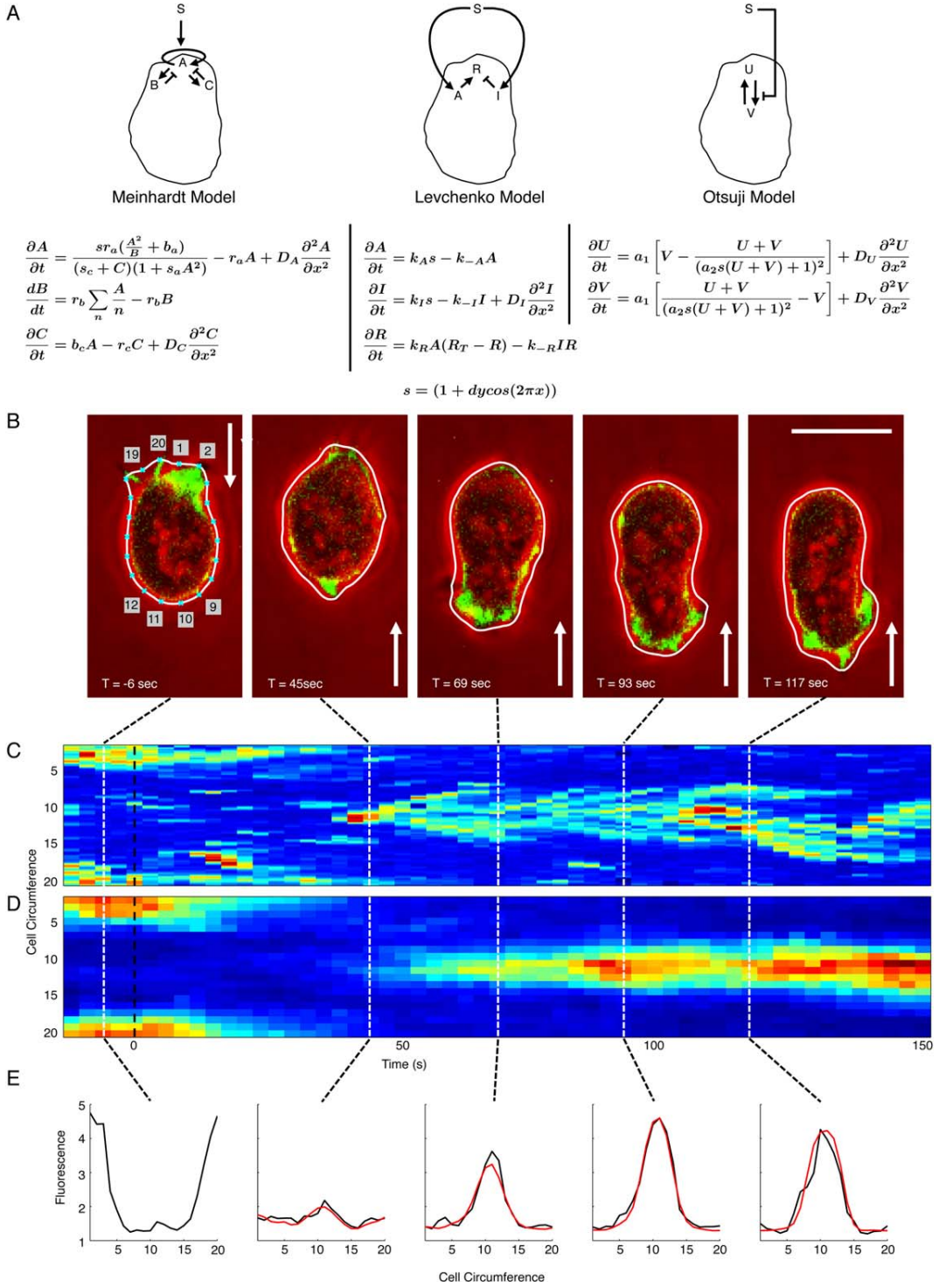

Figure 1. Molecular and computational analysis of actin relocalization in *Dictyostelium* cells: (**A**) schematic diagrams with equations for three alternative models proposed for cell polarity (5,12,13). Each model incorporates a stimulus term, *s*, that provides directionality to the external signal as defined in (5); (**B**) representative sequence of images showing actin relocalization in a single *Dictyostelium* cell after rapid flow reversal (18). Filamentous actin was visualized in JH10 cells expressing LimEΔ-GFP (green) with phase contrast in red. Arrow indicates direction of the high hydrodynamic shear stress ($P = 2.1$ Pa). The outer cell contour (white line) as determined using QuimP 11b (19, http://go.warwick.ac.uk/quimp) where the blue crosses are evenly spaced nodes labelled 1–20. Scale bar, 10 μm; (**C**) time-space plots of the cell from (B) as determined using QuimP 11b. Cell circumference as defined from the nodes shown in (B) with the dashed white lines indicating the time for each image. Black dashed line indicates the time the flow was reversed; (**D**) time-space plot, as determined in (C), for mean data of 18 responses from 14 cells (18); and (**E**) mean cortex fluorescence (black) for the indicated times points from (D). Red indicates example model fit using the Meinhardt model as defined in (A). [Color figure can be viewed in the online issue, which is available at wileyonlinelibrary.com.]

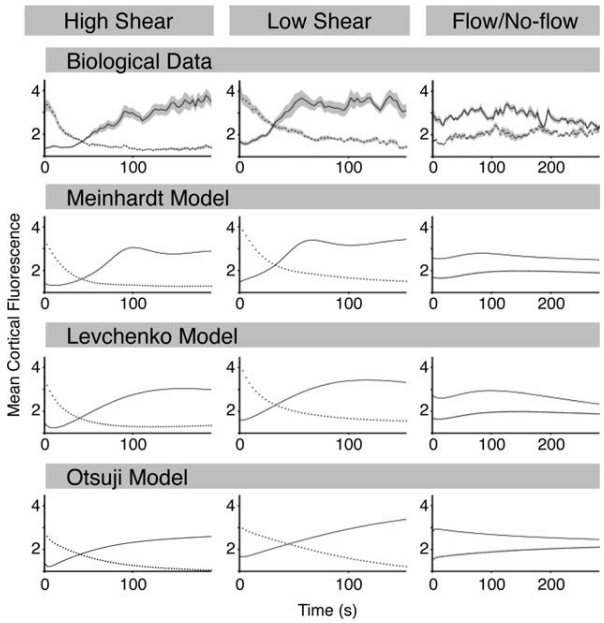

Figure 2. Actin relocalization data enables comparison of three proposed models of cell polarity: to provide a comparison of repolarization cells were split into two halves such that the front (solid line) was determined using the average cortical fluorescence obtained from the nodes 6–15 as illustrated in Figure 1B. The average cortical fluorescence for the back half of the cell (dotted line) was determined from nodes 1–5 and 16–20. Biological data was obtained as described in (18) for a high shear stress (P = 2.1 Pa), a low shear stress (P = 0.9 Pa) and cessation of flow. Mean data for the high shear stress was obtained from 18 responses from 14 cells, for the low shear stress 10 responses from 5 cells was analyzed, while 13 responses from 9 cells are shown in the cessation data set. For all data the shaded area represents standard error of the mean. Models as defined in Figure 1 were simultaneously fitted to all biological data sets using PottersWheel (see Methods). All parameters were conserved between data sets with the exception of *dy*, the asymmetry of the external stimulus. The goodness of fit, χ^2, is 178, 155, and 361 for the Meinhardt, Levchenko, and Otsuji models, respectively.

external signal strength dy be an unknown function of P, determining $dy(P)$ for P = 0.9 Pa and P = 2.1 Pa when data fitting. All models were fitted to the three different experiments simultaneously to increase the selective pressure on each model. Both the Meinhardt and Levchenko models were able to capture the loss of fluorescence at the old cell front but both provided better fits for the large shear stress ($T_{1/2}$ = 36 s for P = 2.1 Pa, $T_{1/2}$ = 45 s for P = 0.9 Pa), with the Otsuji model having problems to capture the fast decrease ($T_{1/2}$ = 83 s for P = 2.1 Pa, $T_{1/2}$ = 110 s for P = 0.9 Pa). The same was true for the gain of fluorescence at the newly activated front, where the Meinhardt and Levchenko models outperformed the Otsuji model. A similar trend was also observed when analysing the flow/no-flow experiments. The overall goodness of fit was summarized by χ^2 values of 178, 156, and 361 for the Meinhardt, Levchenko, and Otsuji models, respectively. Given the deficiencies of the Otsuji model to fit the reorientation data our further investigations concentrate only on the Meinhardt and Levchenko model.

Identifiability Analysis

The model fitting described previously provides parameters that maximize the goodness of fit, however, it is important to consider if these are the only combination of parameters that can explain the data. To address this, we have used profile likelihood estimations, where values for one particular parameter are changed over a defined region and the model is repeatedly refitted to compute how changing the parameter affects the goodness of fit. Identifiable parameters are characterized by a parabolic χ^2 profile which indicates a unique, optimal parameter value (Fig. 3A). Unidentifiable parameters do not affect the quality of the fit, and consequently have a flat profile; they might however be constrained by an upper or a lower limit. Unidentifiability can be linked either to the structure of a model, requiring changes to the model itself or a lack of quality experimental data causing practical unidentifiabilities. The profile likelihoods for the Meinhardt model show that all but one parameter were identifiable with r_b practically non identifiable. In the Levchenko model four out of ten parameters were practically unidentifiable.

A Simplified Two-Variable Version of the Meinhardt Model is Uniquely Identifiable

As shown previously, both, the models by Meinhardt and Levchenko were not fully identifiable. Different approaches exist to make models identifiable, changing either the model or the experimental design (24). In the Meinhardt model, we observed that the first inhibitor, B, remained close to 1, thus we first considered reducing the model to two variables, setting $\partial B/\partial t$ to zero. Ideally, it would still capture the same dynamics of A but become identifiable as the previously unidentifiable parameter r_b was dropped. However, we were unable to find a single value for B around 1, nor a simple linear expression in terms of the external shear stress P, which fitted all three experimental conditions simultaneously. We, therefore, determined optimum values of B for each condition and fitted a quadratic, $B(P)=1+\beta_0(P^2+\beta_1 P)$, in terms of P, which made it possible to simplify dy to $dy(0)$ = 0, and $dy(P)$=const=0.0128. Contrary to the original three-variable Meinhardt model, the reduced model has the advantage that it depends explicitly on the external shear stress. In principle, the exact nature of B(P) could be tested through fitting additional experiments with different shear stresses P, which however is beyond the scope of the current study.

We next performed profile likelihood estimations (Fig. 4A) for multi-experiment fits of the two-variable model to the same three experimental conditions as in Figure 2. The two-variable model generated a similar good fit (χ^2=184 compared to χ^2=178 for the three-variable model, half-lives for the loss of F-actin at the old front are almost identical). Moreover the parameter sets obtained when fitting were also similar between the two and three-variable model (Supporting Information Table S1 and Fig. 4B).

Using the Models to Make Predictions About the Persistence of Front Activation

Both, the Meinhardt and the Levchenko models fitted shear flow reversals reasonably well. We wanted to test whether we would be able to predict the outcome of a new experiment

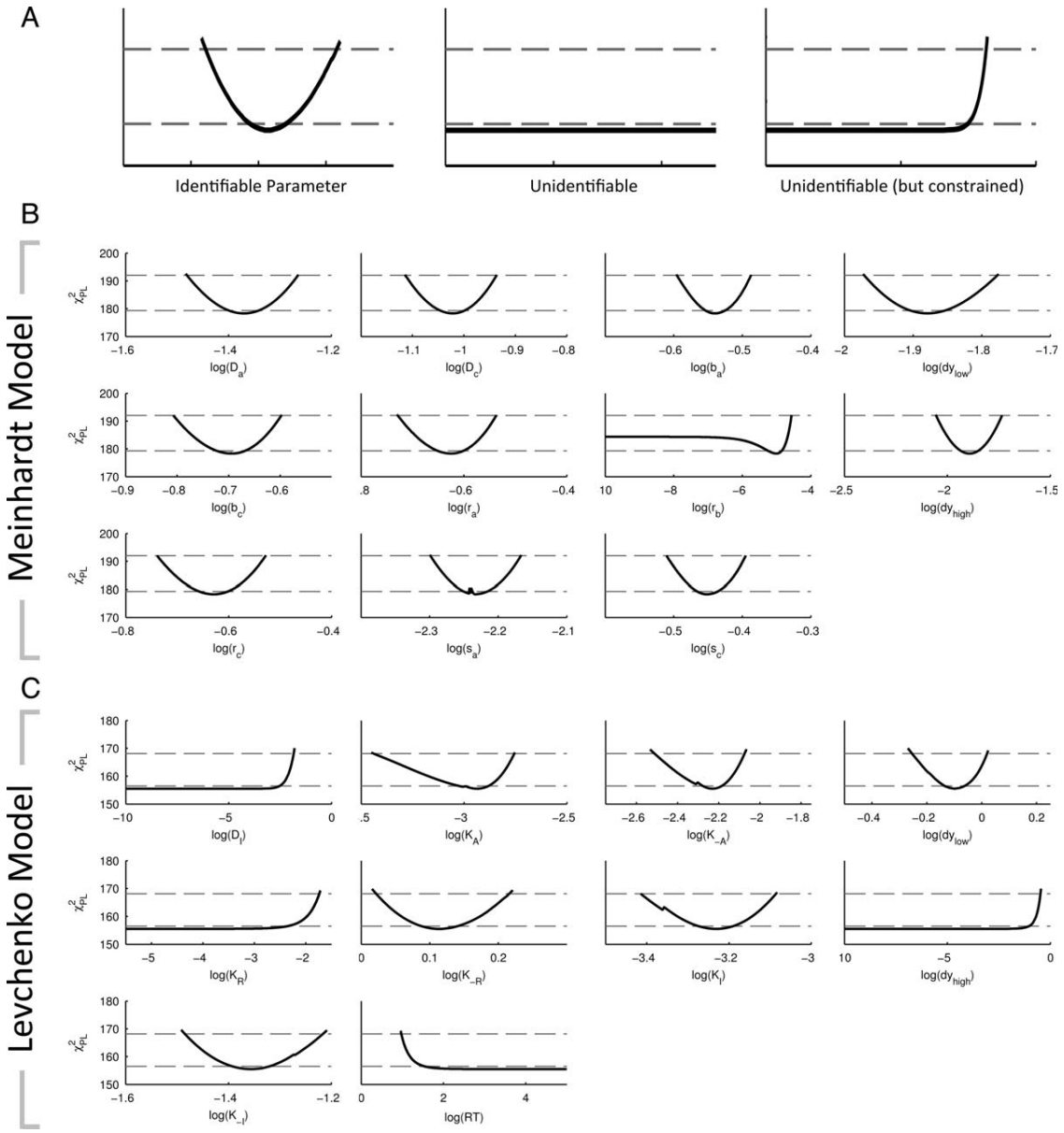

Figure 3. Profile likehood estimates for the Meinhardt and Levchenko models of cell polarity: (**A**) representative plots of profile likelihood estimation (PLE) analysis for example parameters demonstrating identifiable, unidentifiable and unidentifiable (but constrained) as defined by (24). PLE (χ^2 values) together with the point wise (dashed lower horizontal line) and simultaneous confidence levels (dashed upper horizontal line). The intersection where the PLE crosses the simultaneous confidence levels yields the lower and upper boundary for the simultaneous confidence intervals. A parameter is identifiable if both confidence intervals are finite as illustrated; (**B**) PLE analysis of Meinhardt model as defined in Figure 1. All parameters with the exception of r_b are identifiable; and (**C**) PLE analysis of Levchenko model demonstrating six identifiable parameters with four constrained but unidentifiable parameters.

using the sets of parameters obtained previously. We exposed a cell to two cycles of flow-induced (1 Pa) polarization and observed a persistent migration of the cell toward the flow source (Fig. 5A). Cessation of the flow for 2 min caused a loss of polarity. We performed simulations where we first wanted to qualitatively reproduce the persistent activation of the cell front as seen by the steady migration of the example cell for 10 min (Fig. 5B). These were initialized with uniform conditions and the system equilibrated, before replicating the signal behavior detailed above. Using the parameter set obtained in Figure 3, the Levchenko model failed to produce a stable front. To obtain a stable front a rather drastic change to the model was required, for example, increasing D_1 by four orders of magnitude and k_{-A} by a factor of 10. (Supporting Information Table S1 and Fig. 5C). Using the parameter set obtained in Figure 4 for the modified Meinhardt model, a single front was obtained but it rapidly split into three. A single persistent front could be obtained by reducing diffusion of the inhibitor C by 20% (Fig.

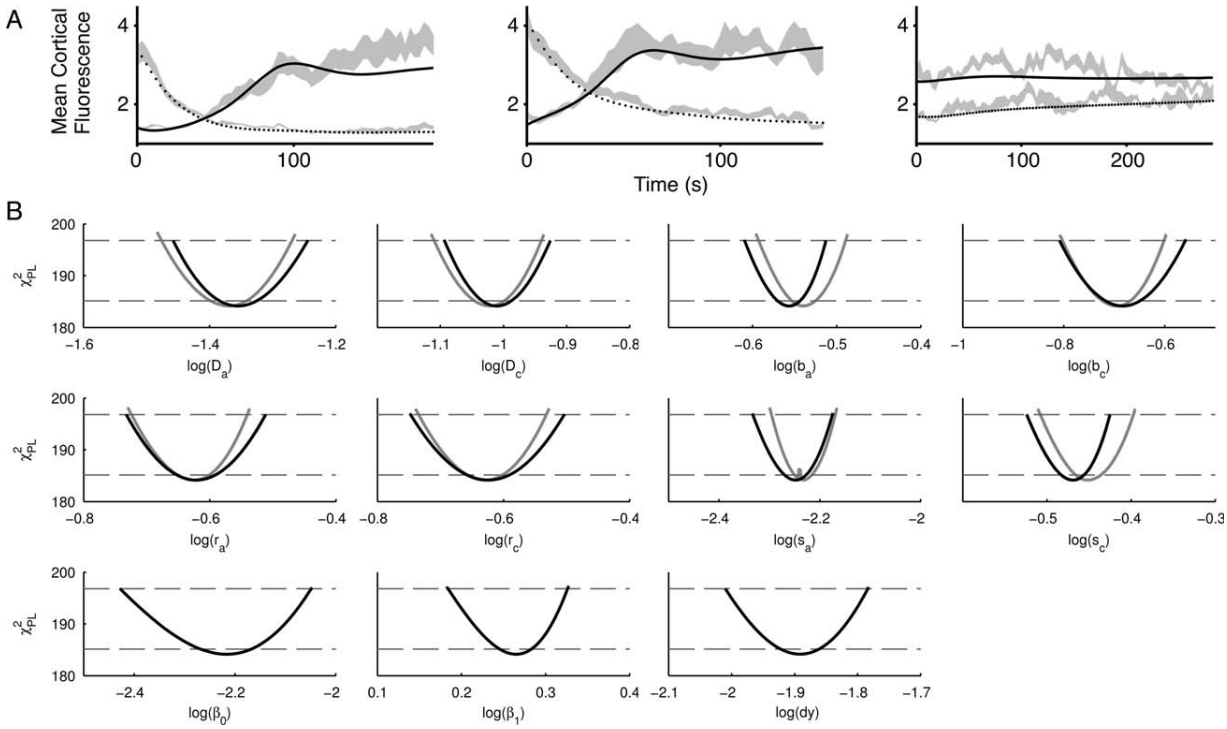

Figure 4. A fully identifiable reduced Meinhardt model replicates actin repolarization behavior: (**A**) fitting of a reduced Meinhardt model to the biological data described in Figure 2. Model has been reduced as described in the text and was simultaneously fitted to all biological data sets using PottersWheel ($\chi^2=184$) and (**B**) PLE analysis of the reduced Meinhardt model from (A). PLE analysis was performed as described in Figure 3 where solid lines represents the PLE and the thresholds are marked by dashed lines. Shown in gray are the conserved parameters between the reduced Meinhardt model and the one analyzed in Figure 3. Values from Figure 3 have been modified through the addition of $\Delta\chi^2=5.833$ to facilitate a direct comparison.

5D). This new constraint does not compromise the goodness of fit for the original repolarization data of Figure 4 (new $\chi^2=182$ compared to $\chi^2=184$ before).

Fitting Spontaneous Front Activation in Randomly Migrating Cells

Previously, we aggregated and synchronized data from multiple cells to obtain averaged data where noise is significantly reduced. Next, we attempted to simultaneously fit single cell data of randomly migrating *Dictyostelium* cells to determine how the models performed on more complex and noisy data (Figs. 6A and 6B). We fitted our biological data using both the Meinhardt and Levchenko models. Whereas the models are deterministic, the observed random patterns are clearly driven by noise. By treating the initial activator concentrations as free parameters, we only account for noise at the start of the time series.

We observed that for the Meinhardt model four parameters were an order of magnitude lower when compared to parameters obtained in Figure 5 (Supporting Information Table S1), three were of the same order and D_C could essentially be set to zero. Parameters in the Levchenko model also vary greatly between reorientation and random motility experiments (Supporting Information Table S1).

Both models captured some of the intrinsic dynamics surprisingly well (Figs. 6A, and 6B): (i) a front which abruptly disappears, (ii) a front which splits into two, and (iii) a broader low intensity F-actin crescent at the cell rear. Regions IV and VI of a second cell (Fig. 6B) again resemble front splitting, while region V denotes the merger of two fronts. Fitting reaction-diffusion models to image data has been successfully applied in image enhancement in many areas (25), Our example shows that the same concepts, usually applied to single images, can be extended in a straight-forward manner to filtering time series image data, thus aiding the model-based analysis of complex stochastic time-series data.

Discussion

A number of sophisticated mathematical models that couple models for cell orientation to cell deformation have recently been published (6–8). Interestingly, they all employ the original model for cell orientation by Meinhardt (5), which as we have shown demonstrates good agreement with experimental data of *Dictyostelium* cells responding to three different experimental conditions (18). Significantly, the model is able to make reasonable predictions of cortical F-actin dynamics during cell reorientation for up to 2 min, which is remarkable given that the turnover of the entire F-actin system in *Dictyostelium* is on the timescale of seconds (26,27).

Chemotactic receptors have been very well characterized but only recently has light been shed on putative mechanosensors, in particular PKD2 Ca^{2+} channels (28). Previously we

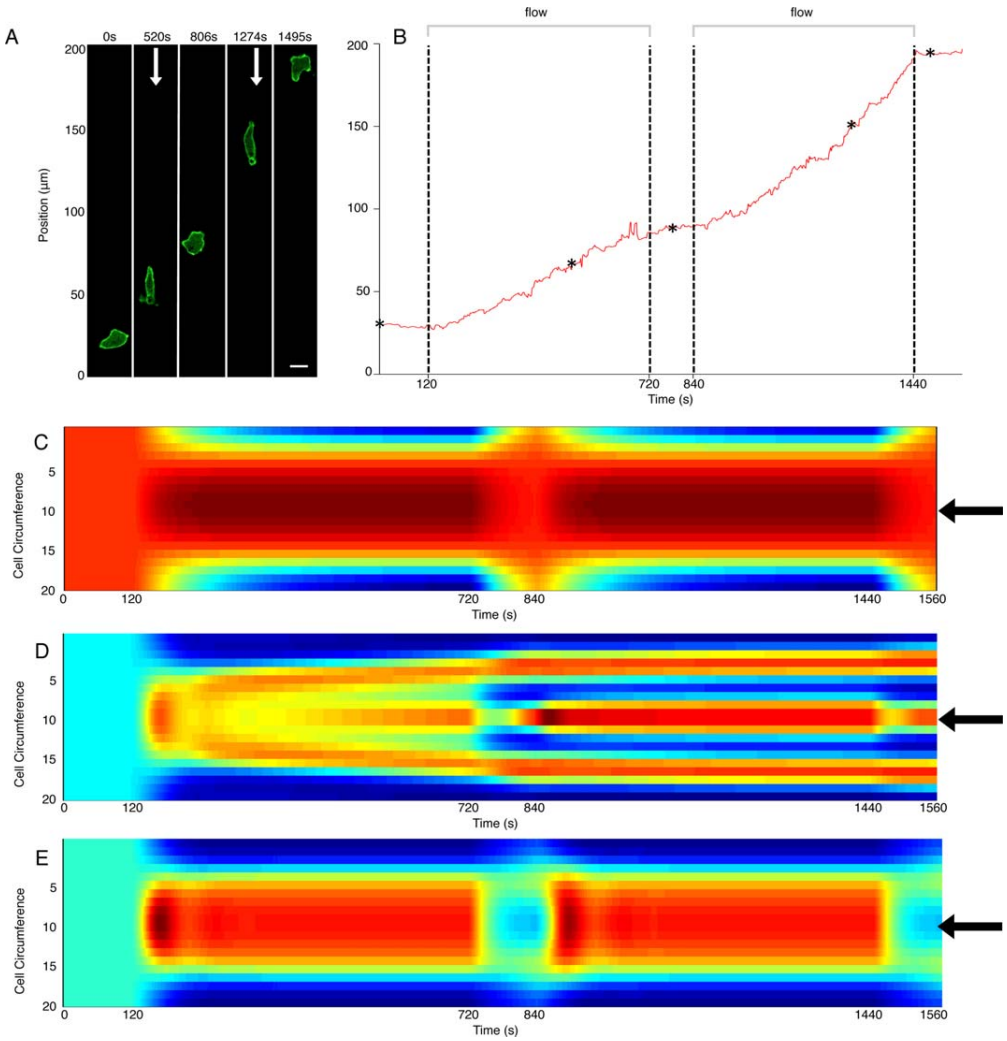

Figure 5. Simulated responses to long duration stimulation: (**A**) image sequence of wild-type (AX2) cells expressing ABP120-GFP (green). Cells were imaged for a total period of 1,560 s. Following an initial rest period (120 s) cells were exposed to a continuous flow for a duration of 600 s. The cycle was then repeated for a further 720 s. Arrows indicate presence and the direction of a shear stress $P = 1$ Pa; (**B**) Position of the cell front (relative to the bottom of the image) throughout the time course. Asterisks denote times of the five individual images shown. Scale bar, 10 μm; (**C**) simulations of the biological data in (A) using the Levechenko model. The arrow denotes the position where the external signal is the strongest. Adjustment of model parameters D_I and k_{-A} in the Levchenko model allows a persistent front to be obtained; (**D**) simulations of the biological data in (A) using the reduced Meinhardt model as described in Figure 4 results in breaking up of a single front; and (**E**) decreasing the diffusion constant for inhibitor C from 9.768×10^{-2} to 7.064×10^{-2} produces a persistent front. All models were started with uniform conditions and simulated in the absence of signal for 5,000 s before the signal input from experiment was replicated. [Color figure can be viewed in the online issue, which is available at wileyonlinelibrary.com.]

have shown that in *Dictyostelium* cells reversal of cell polarity in response to a shear flow reversal is very similar to the response seen when reversing a chemotactic gradient. This suggests that both sensor systems might be linked to one common pathway regulating actin polymerization and cell polarization (18). It is interesting to note that the models originally developed to investigate chemotaxis are equally applicable to mechanotaxis.

The estimation of model parameters from image data and identifiability analysis in the context of diffusion processes is an emerging area of research (29). We have reduced the Meinhardt model to a two-variable model, which is uniquely identifiable. Although there is no direct correspondence with known biochemical pathways, the activator variable in the model captures, remarkably well, the dynamics of F-actin assembly. The parameters we determined yield biochemically realistic timescales of cell front activation and repolarization, which will be appreciated by modelers trying to build more complex models that integrate actin dynamics and protrusive behavior.

The behavior of the reduced two-variable Meinhardt model is almost identical to the three-variable model. Although the second inhibitor in the Meinhardt model is often regarded as an improved extension of a model with only one inhibitor, adding permanent sensitivity, its local action can completely replace the first global inhibitor. In line with

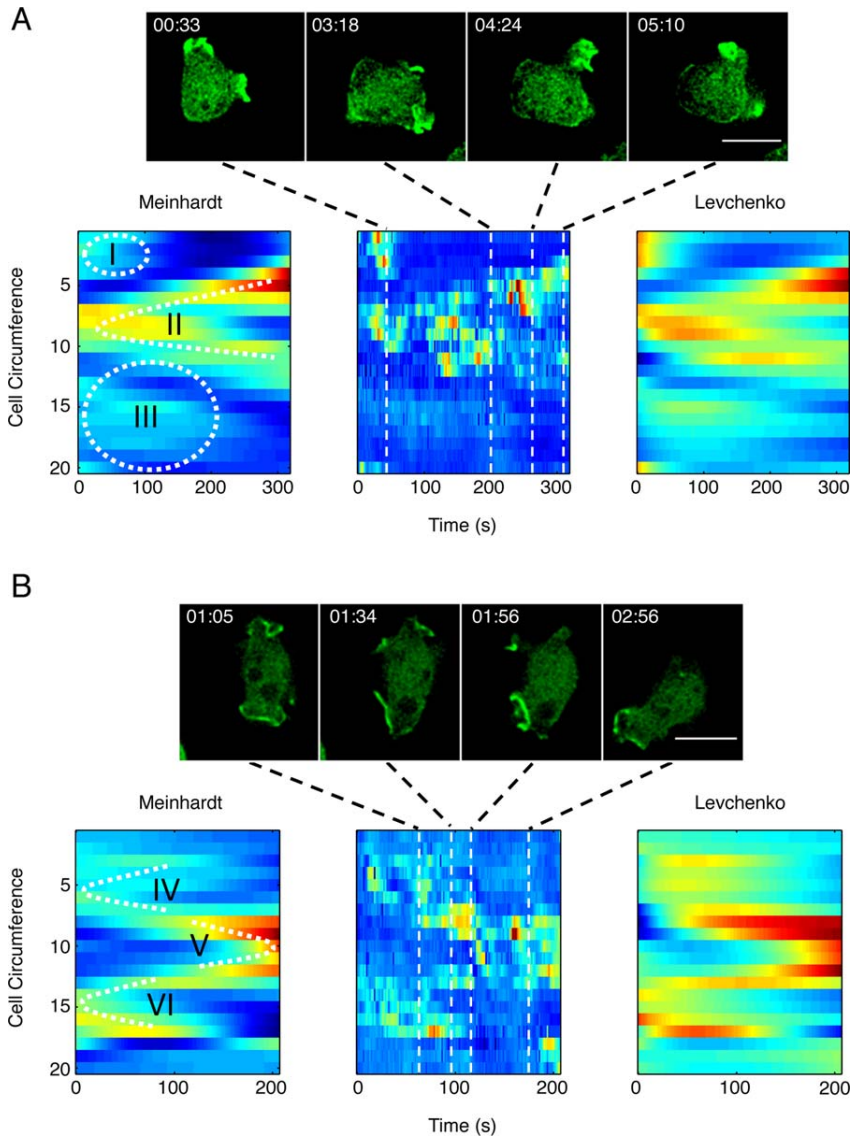

Figure 6. Comparison of the reduced Meinhardt and Levchenko models in simulating actin localization of unstimulated cells: two image sequences of representative cells (**A** and **B**) in the absence of an external signal. Filamentous actin was visualized in wild-type (AX2) cells expressing LimEΔ-RFP (green). QuimP 11b analysis performed as described in Figure 1 was used to generate cell cortex fluorescence data (central time–space plot) that was used for fitting both the reduced Meinhardt (χ^2=1485) and Levchenko (χ^2=1399) models. Regions of interest, highlighted by roman numerals, illustrate the ability of each model to capture biological phenomena. Scale bar, 10 μm. [Color figure can be viewed in the online issue, which is available at wileyonlinelibrary.com.]

that we found that the first inhibitor remained constant over time, justifying its removal as an independent variable. Similarly the Levchenko model achieves the same behavior using only one inhibitor, and also captures many aspects of F-actin dynamics during reorientation and random motility.

We have shown that care is needed when trying to make predictions as initially we were unable to achieve long-term persistence of front activation. Both the Meinhardt and Levchenko models required changes in their parameters. Significantly, this helped to constrain the models further; indeed the Meinhardt model was still able to fit our original set of data under the new constraint.

Randomly migrating cells display several competing fronts, which aids the probing of their environment by increasing the sampling frequency. The presence of a strongly orientating stimulus such as a chemotactic agent or shear flow requires cells to enter a different state where only a single front survives. Thus, it is expected that this new state is reflected by changes in parameters. In theory, going from several fronts to a single one is equivalent to increasing the wavelength of the pattern, which can be achieved by increasing activator diffusion. Here we confirm, for the Meinhardt model, that the diffusion of the activator in randomly migrating cells is by a factor of 20 lower, when compared to the shear flow experiments. The rate of inhibitor

diffusion becomes essentially negligible, suggesting a qualitative change in the model such that there is no lateral inhibition of activated peaks any more. This lack of lateral inhibition results in patterns of activation which are not evenly spaced, which is in fact a notable feature of random migration. Therefore, the changes in fitted diffusion rates are in agreement with the experimental observations. At the same time, fronts in randomly migrating cells are less stable, which explains why some of the kinetic parameters are also required to change. Interpretation of the exact changes is however difficult. Although the rates of production and decay of the local inhibitor *C* are, for example, reduced by a factor of 4, its local concentration can still increase rapidly, because it does not diffuse. This might contribute to the observed shorter lifetime of activated fronts in randomly migrating cells. Recently, membrane tension has been discussed as an inhibitory mechanism restricting the growth of protruding fronts, which because of its physical nature could explain very fast diffusive spreading (30,31). Therefore, one possibility supported by the change in model parameters could be that cells globally increase membrane tension when switching from random migration to a strongly polarized mode of movement.

Similarly to our example of modeling cell orientation, inverse modeling of spatio-temporal cellular dynamics has been employed in the context of photobleaching or photoactivation experiments to study the mobility, mass transport, or binding of cellular constituents (32–34). Perturbing the intrinsic dynamics by photobleaching or activation could nicely complement our approach, thereby trying to match diffusion in the model with the mobility of molecular players known to be involved in signaling to the actin cytoskeleton. More detailed biological models exist for receptor/G-protein networks, and signaling to the downstream modules controling polarity/myosin-II contractility and actin reorganization (35). Recently, Skoge et al. (36) have developed a model for Ras activation in chemotaxing *Dictyostelium* cells which includes memory effects to explain why cells do not reverse direction in the wake of a wave of chemoattractant. The model consists of seven equations with 24 parameters and has been successfully fitted to activated Ras levels measured at the front and the back of cells. We believe that our proposed framework will be a valuable tool to compare this and other recent models in the future. For example, to learn what degree of complexity is required to explain particular experimental findings which cannot be easily explained by the very simple models discussed in the current paper.

Acknowledgments

We thank Ingrid Tigges (Warwick Systems Biology) for providing the experimental data in Figure 5 and Jeremie Dalous for performing the shear flow experiments and valuable discussions.

Literature Cited

1. Kay RR, Langridge P, Traynor D, Hoeller O. Changing directions in the study of chemotaxis. Nat Rev Mol Cell Biol 2008;9:455–463.
2. Insall RH. Understanding eukaryotic chemotaxis: A pseudopod-centred view. Nat Rev Mol Cell Biol 2010;11:453–458.
3. Ridley AJ. Life at the leading edge. Cell 2011;145:1012–1022.
4. Turing AM. The chemical basis of morphogenesis. Philos Trans R Soc Lond B Biol Sci 1952;237:37–62.
5. Meinhardt H. Orientation of chemotactic cells and growth cones: Models and mechanisms. J Cell Sci 1999;112:2867–2874.
6. Neilson MO, Veltman DM, van Haastert PJ, Webb SD, Mackenzie JA, Insall RH. Chemotaxis: A feeback-based computational model robustly predicts multiple aspects of real cell behavior. PLoS Biol 2011;9:e1000618.
7. Elliott CM, Stinner B, Venkataraman C. Modelling cell motility and chemotaxis with evolving surface finite elements. J R Soc Interface 2012;9:3027–3044.
8. Tweedy L, Meier B, Stephan J, Heinrich D, Endres RG. Distinct shapes determine accurate chemotaxis. Sci Rep 2013;3:2606.
9. Shi C, Huang CH, Devreotes PN, Iglesias PA. Interaction of motility, directional sensing, and polarity modules recreates the behaviors of chemotaxing cells. PLoS Comput Biol 2013;9:e1003122.
10. Shibata T, Nishikawa M, Matsuoka S, Ueda M. Intracellular encoding of spatiotemporal guidance cues in a self-organizing signaling system for chemotaxis in *Dictyostelium* cells. Biophys J 2013;105:2199–2209.
11. Jilkine A, Edelstein-Keshet L. A comparison of mathematical models for polarization of single eukaryotic cells in response to guided cues. PLoS Comput Biol 2011;7: e1001121.
12. Otsuji M, Ishihara S, Co C, Kaiguchi K, Mochizuki A, Kuroda S. A mass conserved reaction–diffusion system captures properties of cell polarity. PLoS Comput Biol 2007; 3:e108.
13. Levchenko A, Iglesias PA. Models of eukaryotic gradient sensing: application to chemotaxis of amoebae and neutrophils. Biophys J 2002;82:50–63.
14. Chis OT, Banga JR, Balsa-Canto E. Structural identifiability of systems biology models: A critical comparison of methods. PLoS One 2011;6:e27755.
15. Dorman D, Libotte T, Weijer CJ, Bretschneider T. Simultaneous quantification of cell motility and protein–membrane-association using active contours. Cell Motil Cytoskeleton 2002;52:221–230.
16. Etzrodt M, Ishikawa HC, Dalous J, Müller-Taubenberger A, Bretschneider T, Derisch G. Time-resolved responses to chemoattractant, characteristic of the front and tail of *Dictyostelium* cells. FEBS Lett 2006;580:6707–6713.
17. Bosgraaf L, van Haastert PJ, Bretschneider T. Analysis of cell movement by simultaneous quantification of local membrane displacement and fluorescent intensities using Quimp2. Cell Motil Cytoskeleton 2009;66:156–165.
18. Dalous J, Burghardt E, Müller-Taubenberger A, Bruckert F, Gerisch G, Bretschneider T. Reversal of cell polarity and actin–myosin cytoskeleton reorganization under mechanical and chemical stimulation. Biophys J 2008;94:1063–1074.
19. Tyson RA, Epstein DBA, Anderson KI, Bretschneider T. High resolution tracking of cell membrane dynamics in moving cells: An electrifying approach. Math Model Nat Phenom 2010;5:34–55.
20. Rasband WS. Image J, U. S. National Institutes of Health, Bethesda, Maryland, USA, http://imagej.nih.gov/ij/, 1997–2014.
21. Maiwald T, Eberhardt O, Blumberg J. Mathemtical modeling of biochemical systems with PottersWheel. Methods Mol Biol 2012;880:119–138.
22. Coleman TF, Li Y. An interior trust region approach for nonlinear minimization subject to bounds. SIAM J Optim 1996;6:418–445.
23. Coleman TF, Verma A. A preconditioned conjugate gradient approach to linear equality constrained minimization. Comput Optim Appl 2001;20:61–72.
24. Raue A, Kreutz C, Maiwald T, Bachmann J, Schilling M, Klingmüller U, Timmer J. Structural and practical identifiability analysis of partially observed dynamical models by exploiting the profile likelihood. Bioinformatics 2009;25:1923–1929.
25. Weickert J. Anisotropic diffusion in image processing. Germany: Teubner Stuttgart; 1998.
26. Diez S, Gerisch G, Anderson K, Müller-Taubenberger A, Bretschneider T. Subsecond reorganization of the actin network in cell motility and chemotaxis. Proc Natl Acad Sci USA 2005;102:7601–7606.
27. Bretschneider T, Diez S, Anderson K, Heuser J, Clarke M, Müller-Taubenberger A, Köhler J, Gerisch G. Dynamic actin patterns and Arp2/3 assembly at the substrate-attached surface of motile cells. Curr Biol 2004;14:1–10.
28. Lima WC, Vinet A, Pieters J, Cosson P. Role of PKD2 in rheotaxis in *Dictyostelium*. PLoS One. 2014;9(2):e88682.
29. Hock S, Hasenauer J, Theis FJ. Modeling of 2D diffusion processes based on microscopy data: Parameter estimation and practical identifiability analysis. BMC Bioinformat. 2013;14 Suppl 10:S7.
30. Graziano BR, Weiner OD. Self-organization of protrusions and polarity during eukaryotic chemotaxis. Curr Opin Cell Biol 2014;30:60–67.
31. Tyson RA, Zatulovskiy E, Kay RR, Bretschneider T. How blebs and pseudopods cooperate during chemotaxis. Proc Natl Acad Sci USA. 2014;111(32):11703–11708.
32. Sadegh-Zadeh K, Montas HJ, Shirmohammadi A. Identification of biomolecule mass transport and binding rate parameters in living cells by inverse modeling. Theor Biol Med Model 2006;3:36.
33. Ulrich M, Kappel C, Beaudouin J, Hezel S, Ulrich J, Eils R. Tropical – Parameter estimation and simulation of reaction–diffusion models based on spatio-temporal microscopy images. Bioinformatics 2006;22:2709–2710.
34. Tardy Y, McGrath JL, Hartwig JH, Dewey CF. Interpreting photoactivated fluorescence microscopy measurements of steady-state actin dynamics. Biophys J 1995;69:1674–1682.
35. Artemenko Y, Lampert TJ, Devreotes PN. Moving towards a paradigm: Common mechanisms of chemotactic signaling in *DIctyostelium* and mammalian leukocytes. Cell Mol Life Sci 2014;71:3711–3747.
36. Skoge M, Yue H, Erickstad M, Bae A, Levine H, Groisman A, Loomis WF, Rappel WJ. Cellular memory in eukaryotic chemotaxis. Proc Natl Acad Sci USA. 2014;111: 14448–14453.

BIBLIOGRAPHY

Agard, D. A. (1984), 'Optical sectioning microscopy: Cellular architecture in three dimensions', *Annual Review of Biophysics and Engineering* **13**, 191–219.

Bagorda, A. & Parent, C. A. (2008), 'Eukaryotic chemotaxis at a glance', *Journal of Cell Science* **121**, 2621–2624.

Bellu, G., Saccomani, M. P., Audoly, S. & D'Angio, L. (2007), 'Daisy: a new software tool to test global identifiability of biological and physiological systems', *Computer Methods and Programs in Biomedicine* **88**, 52–61.

Bolourani, P., Spiegelman, G. B. & Weeks, G. (2006), 'Delineation of the roles played by RasG and RasC in cAMP-dependent signal transduction during the early development of *Dictyostelium Discoideum*', *Molecular Biology of the Cell* **17**, 4543–4550.

Bosgraaf, L., Russcher, H., Smith, J. L., Wessels, D., Soll, D. R. & Haastert, P. J. M. V. (2002), 'A novel cGMP signalling pathway mediating myosin phosphorylation and chemotaxis in *Dictyostelium*', *The EMBO Journal* **21**, 4560–4570.

Bosgraaf, L., van Haastert, P. & Bretschneider, T. (2009), 'Analysis of cell movement by simultaneous quantification of local membrane displacement and fluorescent intensities using Quimp2', *Cell Motility and the Cytoskeleton* **66**, 156–165.

Chen, L., Iijiama, M., Tang, M., Landree, M. A., Huang, Y. E., Xiong, Y., Iglesias, P. A. & Devreotes, P. (2007), 'PLA2 and PI3K/PTEN pathways act in parallel to mediate chemotaxis', *Developmental Cell* **12**, 603–614.

Chen, M. Y., Insall, R. H. & Devreotes, P. N. (1996), 'Signaling through chemoattractant receptors in dictyostelium.', *Trends in Genetics* **12**, 52–57.

Coleman, T. F. & Li, Y. (1996), 'An interior trust region approach for nonlinear minimization subject to bounds', *SIAM Journal on Optimization* **6**, 418–445.

Coleman, T. F. & Verma, A. (2001), 'A preconditioned conjugate gradient approach to linear equality constrained minimization', *Computational Optimization and Applications* **20**, 61–72.

Croft, W., Elliott, C. M., Ladds, G., Stinner, B., Venkataraman, C. & Weston, C. (2015), 'Parameter identification problems in the modelling of cell motility', *Journal of Mathematical Biology* **7**, 399–436.

Cross, M. & Greenside, H. (2009), *Pattern Formation and Dynamics in Nonequilibrium Systems*, Cambridge University Press.

Dalous, J., Burghardt, E., Müller-Taubenberger, A., Bruckert, F., Gerisch, G. & Bretschneider, T. (2008), 'Reversal of cell polarity and actin-myosin cytoskeleton reorganization under mechanical and chemical stimulation', *Biophysical Journal* **94**(3), 1063 – 1074.

Décavé, E., Rieu, D., Dalous, J., Fache, S., an Bertrand Fourcade, Y. B., Satre, M. & Bruckert, F. (2003), 'Shear flow-induced motility of *Dictyostelium Discoideum* cells on solid substrate', *Journal of Cell Science* **116**, 4331–4343.

DiCiccio, T. J. & Efron, B. (1996), 'Bootstrap confidence intervals', *Statistical Science* **11**, 189–228.

Dixit, N., Yamayoshi, I., Nazarian, A. & Simon, S. I. (2011), 'Migrational guidance of neutrophils is mechanotransduced via high-affinity LFA-1 and calcium flux', *The Journal of Immunology* **187**, 472–481.

Efron, B. (1977), 'Bootstrap methods: Another look at the jackknife', *The Annals of Statistics* **7**, 1–26.

Efron, B. (1987), 'Better bootstrap confidence intervals', *Journal of the American Statistical Association* **82**, 171–185.

Elliott, C. M., Stinner, B. & Venkataraman, C. (2012), 'Modelling cell motility and chemotaxis with evolving surface finite elements', *Journal of the Royal Society Interface* **9**, 3027–44.

Etzrodt, M., Ishikawa, H. C. F., Dalous, J., Müller-Taubenberger, A., Bretschneider, T. & Gerisch, G. (2006), 'Time-resolved responses to chemoattractant, characteristic of the front and tail of *Dictyostelium* cells', *FEBS Letters* **580**, 6707–6713.

Fache, S., Dalous, J., Engelund, M., Hansen, C., Chamaraux, F., Fourcade, B., Satre, M., Devreotes, P. & Bruckert, F. (2005), 'Calcium mobilization stimulates dictyostelium discoideum shear-flow-induced cell motility', *Journal of Cell Science* **118**, 3445–3457.

Fey, P., s Kowal, A., Gaudet, P., Pilcher, K. E. & Chisholm, R. L. (2007), 'Protocols for gorwth and development of *Dictyostelium discoideum*', *Nature Protocols* **2**, 1307–1316.

Gierer, A. & Meinhardt, H. (1972), 'A theory of biological pattern formation', *Kybernetik* **12**, 30–39.

Hairer, E. & Wanner, G. (1996), *Solving Ordinary Differential Equations. Stiff and and Differential-Algebraic Problems.*, Springer Series in Computational Mathematics.

Hindmarsh, A. C., Brown, P. N., Grant, K. E., Lee, S. L., Serban, R., Shumaker, D. E. & Woodward, C. S. (2005), 'SUNDIALS: Suite of nonlinear and differential/algebraic equation solvers', *ACM Transactions on Mathematical Software* **31**, 363–396.

Hoeller, O., Bolourani, P., CLark, J., an Phillip T Hawkins, L. R. S., Weiner, O. D., Weeks, G. & Kay, R. R. (2013), 'Two distinct functions for PI3-kinases in macropinocytosis', *Journal of Cell Science* **126**, 4296–4307.

Hoeller, O. & Kay, R. R. (2007), 'Chemotaxis in the absence of PIP3 gradients', *Current Biology* **17**, 813–817.

Holmes, W. R. & Edelstein-Keshet, L. (2012), 'A comparison of computational models for eukaryotic cell shape and motility', *PLoS Computational Biology* **8**, e1002793.

Ibarra, N., Pollitt, A. & Insall, R. H. (2005), 'Regulation of actin assembly by SCAR/WAVE proteins', *Biochemical Society Transactions* **33**, 1243–1246.

Insall, R. H. (2010), 'Understanding eukaryotic chemotaxis: a pseudopod-centred view', *Nature Reviews Molecular Cell Biology* **11**, 453–458.

Janetopoulos, C., Ma, L., Devreotes, P. N. & Iglesias, P. A. (2004), 'Chemoattractant-induced phosphatidylinositol 3,4,5-trisphosphate accumulation is spatially amplified and adapts, independent of the actin cytoskeleton', *PNAS* **101**, 8951–8956.

Jilkine, A. & Edelstein-Keshet, L. (2011), 'A comparison of mathematical models for polarization of single eukaryotic cells in response to guided cues', *PLoS Computational Biology* **7**, e1001121.

Kamimura, Y., Xiong, Y., Iglesias, P. A., Hoeller, O., Bolourani, P. & Devreotes, P. (2008), 'PIP3 independent activation of TORC2 and PKB at the cell's leading edge meditaes chemotaxis', *Current Biology* **18**, 1034–1043.

Karlsson, J., Anguelova, M. & Jirstrand, M. (2012), 'An efficient method for structural identifiability analysis of large dynamic systems', *Proceedings of the 16th IFAC Symposium of System Identification* .

Keijzer, S. d., Galloway, J., Harms, G. S., Devreotes, P. N. & Iglesias, P. A. (2011), 'Disrupting microtubule network immobilizes amoeboid chemotactic receptor in the plasma membrane', *Biochimica et Biophysica Acta - Biomembranes* **1808**, 1701–1708.

Killich, T., Plath, P. J., Hass, E. C., Xiang, W., Bultmann, H., Rensing, L. & Vicker, M. G. (1994), 'Cell-movement and shape are nonrandom and determined by intracellular, oscillatory rotating waves in *Dictyostelium* amoebas', *Biosystems* **33**, 75–87.

Killich, T., Plath, P. J., Xiang, W., Bultmann, H., Rensing, L. & Vicker, M. G. (1993), 'The locamotion shape and pseudopodial dynamics of unstimulated *Dictyostelium* cells are not random', *Journal of Cell Science* **106**, 1005–1013.

Konjin, T., Barkley, D., Chang, Y. & Bonner, J. (1968), 'Cyclic AMP: a naturally occuring acrasin in the cellular slime molds', *American Naturalist* **102**, 225–233.

Kotsis, F., Nitschke, R., Doerken, M., Walz, G. & Kuehn, E. W. (2008), 'Flow modulates centriole movements in tubular epithelial cells', *Cell and Molecular Physiology* **456**, 1025–1035.

Lee, S., Comer, F. I., Sasaki, A., McLeod, I. X., Duong, Y., Okumura, K., Yates, J. R., Parent, C. A. & Firtel, R. A. (2005), 'TOR complex 2 integrates cell movement during chemotaxis and signal relay in dictyostelium', *Molecular Biology of the Cell* **16**, 4572–4583.

Lehmann, E. & Leo, E. (1983), *Theory of Point Estimation*, Springer.

Levchenko, A. & Iglesias, P. A. (2002), 'Models of eukaryotic gradient sensing: Application to chemotaxis of amoebae and neutrophils', *Biophysical Journal* **82**, 50–63.

Li, L., Nørrelykke, S. F. & Cox, E. C. (2008), 'Persistent cell motion in the absence of external signals: A search strategy for eukaryotic cells', *PLoS ONE* **3**, e2093.

Ma, L., Janetopoulos, C., Yang, L., Devreotes, P. N. & Iglesias, P. A. (2004), 'Two complementary, local excitation, global inibition machanisms acting in parallel can explain the chemoattractant-induced regulation of PI(3,4,5)P_3 response in *Dictyostelium* cells', *Biophysical Journal* **87**, 3764–3774.

Maiwald, T. & Timmer, J. (2008), 'Dynamical modeling and multi-experiment fitting with PottersWheel', *Bioinformatics* **24**(18), 2037–2043.

Makino, A., Prossnitz, E. R., Bünemann, M., Wang, J. M., Yao, W. & Schmid-Schönbein, G. W. (2006), 'G protein-coupled receptors serve as mechanosensors for fluid shear stress in neutrophils', *American Journal of Physiology - Cell Physiology* **290**, 1633–9.

Maree, A. F. M., Jilkine, A., Dawes, A., Grieneisen, V. A. & Edelstein-Keshet, L. (2006), 'Polarization and movement of keratocytes: A multiscale modelling approach', *Bulletin of Mathematical Biology* **68**, 1169–1211.

McCann, C. P., Reicha, E. C., Wang, C., Losert, W. & Parent, C. A. (2014), 'Dictyostelium cells migrate similarly of surfaces of varying chemical composition', *PLoS ONE* **9**.

McRobbie, S. J. & Newell, P. C. (1983), 'Chemoattractant-mediated changes in cytoskeletal actin of cellular slime moulds', *Journal of Cell Science* **68**, 139–151.

Meinhardt, H. (1999), 'Orientation of chemotactic cells and growth cones: models and mechanisms', *Journal of Cell Science* **112**, 2867–2874.

Meinhardt, H. & Gierer, A. (1974), 'Application of a theory of biological pattern formation based on lateral inhibition', *Journal of Cell Science* **15**, 321–346.

Morris, H. L., Reed, C. I., Haycock, J. W. & Reilly, G. C. (2010), 'Mechanisms of fluid-flow-induced matrix production in bone tissue engineering', *Journal of Engineering in Medicine* **224**, 1509–1521.

Narang, A., Subramanian, K. K. & Lauffenburger, D. A. (2001), 'A mathematical model for chemoattractant gradient sensing based on receptor-regulated membrane phospholipid signaling dynamics', *Annals of Biomedical Engineering* **29**, 677–691.

Nardin, E. D., Radel, S. J. & Genco, R. J. (1991), 'Isolation and partial characterization of the formyl peptide receptor components on human neutrophils', *Biochemical and Biophysical Research Communications* **174**, 84–9.

Neilson, M., Mackenzie, J. A. & amd R H Insall, S. D. W. (2011), 'Modelling cell movement and chemotaxis using pseudopod-based feedback', *SIAM Journal on Scientific Computing* **33**, 1035–1057.

Otsuji, M., Ishihara, S., Co, C., Kaibuchi, K., Mochizuki, A. & Kuroda, S. (2007), 'A mass conserved reaction-diffusion system captures properties of cell polarity', *PLoS Computational Biology* **3**, e108.

Parent, C. A., Blacklock, B. J., Froehlich, W. M., Murphy, D. B. & Devreotes, P. N. (1998), 'G protein signalling events are activated at the leading edge of chemotactic cells', *Cell* **95**, 81–91.

Parent, C. A. & Devreotes, P. (1999), 'A cell's sense of direction', *Science* **284**, 765–771.

Raue, A., Becker, V., Klingmuller, U. & Timmer, J. (2010), 'Identifiability and observability analysis for experimental design in nonlinear dynamical models', *Chaos* **20**, 045105.

Raue, A., Kreutz, C., Maiwald, T., Bachmann, J., Schilling, M., Klingmuller, U. & Timmer, J. (2009), 'Structural and practical identifiability analysis of partially observed dynamical models by exploiting the profile likelihood', *Bioinformatics* **25**, 1923–1929.

Raue, A., Kreutz, C., Maiwald, T., Klingmuller, U. & Timmer, J. (2011), 'Addressing parameter identifiability by model-based experimentation', *IET Systems Biology* **5**, 120–130.

Saran, S., Meima, M. E., Avvarez-Curto, E., Weening, K. E., Rozen, D. E. & Schaap, P. (2002), 'cAMP signaling in *Dictyostelium*', *Journal of Muscle Research and Cell Motility* **23**, 793–802.

Segel, L. A. & Jackson, J. L. (1972), 'Dissipative structure: An explanation and an ecological example', *Journal of Theoretical Biology* **37**, 545–559.

Shi, C., Huang, C.-H., Devreotes, P. & Iglesias, P. A. (2013), 'Interaction of motility, directional sensing, and polarity modules recreates the behaviors in chemotaxing cells', *PLoS Computational Biology* **9**, e1003122.

Subramanian, K. K. & Narang, A. (2004), 'A mechanistic model for eukaryotic gradient sensing: Spontaneous and induced phosphoinositide polarization', *Journal of Theoretical Biology* **231**, 49–67.

Turing, A. (1952), 'The chemical basis of morphogenesis', *Philosophical Transactions of the Royal Society (B)* **237**, 37–72.

Tweedy, L., Meier, B., Stephan, J., Heinrich, D. & Endres, R. G. (2013), 'Distinct cell shapes determine accurate chemotaxis', *Scientific Reports* **3**, 2606.

Tyson, R. A., Zatulovskiy, E., Kay, R. R. & Bretschneider, T. (2014), 'How blebs and pseudopods cooperate during chemotaxis', *Proceedings of the National Academy of Sciences* **111**, 11703–11708.

Tyson, R., Epstein, D., Anderson, K. & Bretschneider, T. (2010), 'High resolution tracking of cell membrane dynamics in moving cells: An electrifying approach.', *Mathematical Modelling of Natural Phenomena* **5**, 34–55.

Valignat, M.-P., Theodoly, O., Gucciardi, A., Hogg, N. & Lellouch, A. C. (2013), 'T Lymphocytes orient against the direction of fluid flow during LFA-1-mediated migration', *Biophysical Journal* **104**, 322–331.

Veltman, D. M., Keizer-Gunnink, I. & Haastert, P. J. V. (2008), 'Four key signaling pathways mediating chemotaxis in *Dictyostelium Discoideum*', *Journal of Cell Biology* **180**, 747–753.

Wadhams, G. H. & Armitage, J. P. (2004), 'Making sense of it all: Bacterial chemotaxis', *Nature Reviews* **5**, 1024–1037.

Wojciak-Stothard, B. & Ridley, A. J. (2003), 'Shear stress-induced endothelial cell polarization is mediated by Rho and Rac but not Cdc42 or PI 3-kinases', *The Journal of Cell Biology* **161**(2), 429–439.

Xiong, Y., Huang, C.-H., Iglesias, P. A. & Devreotes, P. N. (2010), 'Cells navigate with a local-excitation, global-inhibition-biased excitable network', *Proceedings of the National Academy of Sciences* **107**(40), 17079–17086.

Zhu, X., Bouffanais, R. & Yue, D. K. P. (2014), 'Persistent cellular motion control and trapping using mechanotactic signaling', *PLoS ONE* **9**.